AD-A153 631 TURBULENCE STRUCTURE IN THE BOUNDARY LAYERS OF AN OSCILLATING AIRFOIL(U) VRIJE UNIV BRUSSELS (BELGIUM) DEPT OF FLUID MECHANICS J D RUYCK ET AL. DEC 83 1/1

UNCLASSIFIED VUB-STR-14 DAJA45-83-C-0021 F/G 20/4 NL

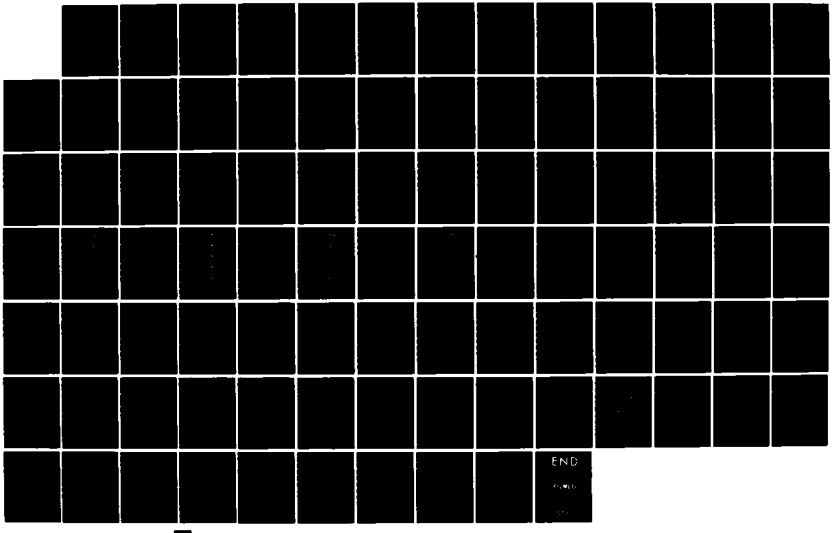

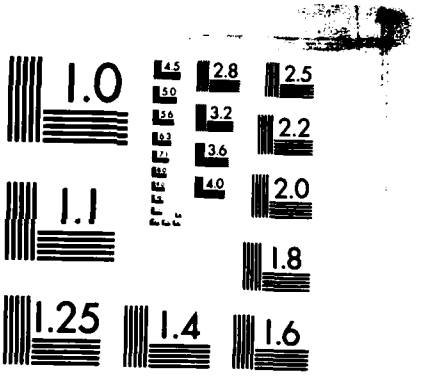

AD

TURBULENCE STRUCTURE IN THE BOUNDARY LAYERS ON AN OSCILLATING AIRFOIL

Final Technical report
by

J. DE RUYCK and Ch. HIRSCH

January 1983 – December 1983

VUB report STR–14

United States Army

RESEARCH & STANDARDIZATION GROUP (EUROPE)

London, England

Contract number DAJA 45–83–C–0021

Contractor : Vrije Universiteit Brussel
Dept. of Fluid Mechanics

AD

TURBULENCE STRUCTURE IN THE BOUNDARY LAYERS ON AN OSCILLATING AIRFOIL

Final Technical report
by

J. DE RUYCK and Ch. HIRSCH

January 1983 – December 1983

VUB report STR–14

United States Army

RESEARCH & STANDARDIZATION GROUP (EUROPE)

London, England

Contract number DAJA 45–83–C–0021

Contractor : Vrije Universiteit Brussel
Dept. of Fluid Mechanics

UNCLASSIFIED

SECURITY CLASSIFICATION OF THIS PAGE (When Data Entered)

R&D 2835

REPORT DOCUMENTATION PAGE

READ INSTRUCTIONS BEFORE COMPLETING FORM

1. REPORT NUMBER	2. GOVT ACCESSION NO. AD-A153 631 / 3. RECIPIENT'S CATALOG NUMBER
4. TITLE (and Subtitle) Turbulence Structure in The Boundary Layers of an Oscillating Airfoil	5. TYPE OF REPORT & PERIOD COVERED Final ~~Annual~~ Report 6. PERFORMING ORG. REPORT NUMBER
7. AUTHOR(s) J. De Ruyck & Ch. Hirsch	8. CONTRACT OR GRANT NUMBER(s) DAJA45-83-C-0021
9. PERFORMING ORGANIZATION NAME AND ADDRESS Vrije Universiteit Brussel Pleinlaan 2, 1050 Brussels Belgium	10. PROGRAM ELEMENT, PROJECT, TASK AREA & WORK UNIT NUMBERS 6.11.02A IT161102BH57-06
11. CONTROLLING OFFICE NAME AND ADDRESS USARDSG-UK Box 65, FPO NY 09510	12. REPORT DATE Jan 83-Dec 83 13. NUMBER OF PAGES 83
14. MONITORING AGENCY NAME & ADDRESS (if different from Controlling Office)	15. SECURITY CLASS. (of this report) Unclassified 15a. DECLASSIFICATION/DOWNGRADING SCHEDULE

16. DISTRIBUTION STATEMENT (of this Report)

Approved for Public Release; distribution unlimited

17. DISTRIBUTION STATEMENT (of the abstract entered in Block 20, if different from Report)

18. SUPPLEMENTARY NOTES

19. KEY WORDS (Continue on reverse side if necessary and identify by block number)

OSCILLATING AIRFOIL, DYNAMIC STALL, EXPERIMENTAL VELOCITY FIELDS, AND REYNOLDS STRESSES.

20. ABSTRACT (Continue on reverse side if necessary and identify by block number)

The main objective of the present work is to provide experimental information about velocity fields and turbulence structures in unsteady flows.

A NACA 0012 airfoil oscillates around an axis at 25% chord distance from the leading edge. With a sinusoidal motion. Instantaneous distributions of velocity as well as all non-zero Reynolds stresses are determined in the profile boundary layers. Measurements are performed at various incidences,

DD FORM 1 JAN 73 1473 EDITION OF 1 NOV 65 IS OBSOLETE

UNCLASSIFIED

SECURITY CLASSIFICATION OF THIS PAGE (When Data Entered)

from non stalled to deep stalled flow conditions. The reduced frequency is 0.3 at a chord Reynolds number of 300,000.

A slanted rotating hot wire is used and the angular calibration characteristics of the wire are applied in order to detect and measure reversed flows.

Instantaneous detailed flow and turbulence patterns of the periodic separation vortex are presented and discussed. These patterns are obtained from traverses at 8 chordwise positions along the auction side of the blade.

ABSTRACT

The main objective of the present work is to provide experimental information about velocity fields and turbulence structures in unsteady flows.

A NACA 0012 airfoil oscillates around an axis at 25 % chord distance from the leading edge, with a sinusoidal motion. Instantaneous distributions of velocity as well as all non-zero Reynolds stresses are determined in the profile boundary layers. Measurements are performed at various incidences, from non-stalled to deep stalled flow conditions. The reduced frequency is 0.3 at a chord Reynolds number of 300,000.

A slanted rotating hot wire is used and the angular calibration characteristics of the wire are applied in order to detect and measure reversed flows.

Instantaneous detailed flow and turbulence patterns of the periodic separation vortex are presented and discussed. These patterns are obtained from traverses at 8 chordwise positions along the suction side of the blade.

Nomenclature

c	blade chord
E	anemometer voltage
f	phase angle
i	incidence
i_o	mean incidence
k	frequency coefficient $\omega c/2Q_\infty$
P	probability density
Q	velocity modulus
q	normalised velocity modulus
u	chordwise velocity
v	velocity normal to the wall
w	spanwise velocity
x	chordwise coordinate
y	coordinate normal to the wall
z	spanwise coordinate
δ	yaw angle
σ	velocity variance $\sqrt{q'^2}$
Φ	degenerate hypergeometric function
$\bar{}$	ensemble averaged value
$'$	fluctuation from ensemble averaged value
$\langle\ \rangle$	expected value
∞	condition far upstream or downstream

1. Introduction

The actual development of computational methods for steady and unsteady flows has reached a stage where two dimensional, time averaged Navier Stokes equations can be solved within reasonable cost and storage requirements, for both steady and unsteady situations. Impressive computational results have been presented during the last years, in particular full 2D Navier-Stokes calculations in stalled unsteady flows [1,2,3]. However, the verification of Navier Stokes solutions is still limited mainly by a lack of detailed experimental data.

To our knowledge only visualisations are available in the case of stalled flows around airfoils. The experimental determination of velocity and turbulence fields in an unsteady, dynamic stalled flow is still a challenge in experimental fluid dynamics. In the present report some progress in this field is presented. A technique has been developed which allows experiments in low speed high turbulent flows with arbitrary flow direction (2D) and it has been applied to measure stalled boundary layers on a pitching NACA 0012 airfoil. Measurements have been performed at eight chordwise positions along the blade chord. Results of five test configurations are available : an unstalled case, two cases with stall onset and two full stalled cases. Detailed data about instantaneous velocity and turbulence fields are available in full dynamic stalled boundary layers, whereas extensive wake measurements were made available in the past [4,5].

2. Previous work

Several reviews on unsteady flow experiments and computations are available : the Freeman lecture by Mc Croskey [6], a review of experimental work done in this field by L.W. Carr [7] and a recent book of Telionis [8] devoted to unsteady flows in general. In this book, different types of unsteady flows are discussed and some application codes are presented.

In the following, previous work closely related to the present experiments is summarized, namely work done on unsteady boundary layers and/or wakes on flat plates and airfoils.

Most of the flat plate experiments are done on a fixed plate with an external oscillating flow. Detailed experiments are available, with and without adverse pressure gradient, in unseparated and to some extend in

separated flows. Frequency coefficients based on the boundary layer thickness range from 0 to .24 [14] and oscillation amplitudes reach 55% of the outer flow [12]. Data of velocities, two or three Reynolds stresses, static pressure and skin friction are available. Table 1 gives an overview of work done in this field with some details about each experiment. This table is not believed to be complete but it gives an idea of the type of experiments and results available in the open literature.

The flat plate experiments can be considered as a more fundamental research whereas more direct data are needed about current flow types such as flows around airfoils. Experiments on unsteady flows around airfoils are in general performed using an oscillating airfoil (pitching or plunging) in a steady free stream, whereas the flat plates are generally fixed. Table 2 gives a summary of airfoil experimental work.

Satyarayana [26] and Saxena et al [27] made experiments on a fixed airfoil in an oscillating external flow. Saxena et al made experiments at angles of attack close to the stall limit. In these experiments pressure distributions and velocity profiles are presented, no Reynolds stresses are given. Covert et al [28] generated an unsteady flow by a rotating cylinder not far from the trailing edge of a NACA 0012 airfoil. They considered rather high frequency coefficients (up to 6) and the unsteady flow components diffuse rapidly downstream ($x/c = 1.2$).

In the case of an oscillating airfoil extensive experiments were made for the determination of unsteady airloads by Mc Croskey and his collaborators. A summary and discussion of these experiments are given in [29]. Several profile shapes were used for these investigations. Unsteady pressures and airloads are determined for various combinations of Mach number (up to .3), frequency (k=.2), oscillation amplitude, mean incidence, Reynolds number (up to 4,000,000) and airfoil shape (NACA 0012, Vertol vr-7, NLR 7301). No velocities or detailed turbulence data were measured. Four different flow regimes were considered : no stall, stall onset, light and deep dynamic stall.

A second type of experiments on oscillating airfoils is performed by Mc Alister and L.W. Carr [30]. The experiments consist in visualisations at low Reynolds number (21,000) of the dynamic stalled flow around a pitching NACA 0012 airfoil. The airfoil oscillated from 0° to 20° incidence at k=.25. Similar visualisations were presented by Robinson and Luttges [31], at a

Reynolds number of 100,000 and by Werle [33] at Re = 5,000 and k=0.5.

A last type of experiment which can be mentioned is performed by Ho and Chen [32]. The purpose of this experiment is to analyse the flow in the vicinity of the trailing edge of a plunging airfoil in a steady free stream. Measurements were made with 5 X-wires in the wake of the airfoil.

Experiments in the steady wakes and boundary layers along airfoils are closely related to the present work. J.C. Yu [21] presented velocity and three Reynolds stress profiles at 16 chordwise positions in the vicinity of the trailing edge of a NACA 63-012 airfoil (x/c from .9 to 1.1). Hah and Laksminarayana [22] presented wake measurement of a NACA 0012 airfoil at 3°, 6° and 9° incidence. Measurements are available at 6 positions in the inner wake, comparisons are made with calculations. More recently, Novak and Ramaprian [23] and Ramaprian et al [24] presented extensive wake measurements in the wakes of a swept NACA 0012 airfoil [23], in the symmetric and asymmetric wakes of flat plates [24] and in the wake of a Korn-Garabedian airfoil. Comparisons are made between theory and experiment for the asymptotic, the intermediate (k-epsilon model) and the inner (Albert's model) wake conditions. Jansen and Mueller [25] presented measurements made in the boundary layers of an NACA 66(3)-018 airfoil at two values of the angle of attack. Measurements were made in the laminar separation bubble near leading edge.

In the present research context, experiments have been made in the wake of a pitching airfoil [4,5]. Several frequencies, oscillation amplitudes and incidences were considered, including steady flow conditions. Velocity and turbulence properties are available at five downstream positions. Several frequencies and oscillation amplitudes were considered. Stall onset was reached in these experiments, but full dynamic stall could not be considered since the required measurement techniques were not yet available.

Methods for the theoretical prediction of the aforementioned flow types are in development. S.B.R. Kottapalli and G.A. Pierce [34] presented an analytical study of the drag on an oscillating airfoil. The turbulence input was based on the Cebeci-Smith eddy viscosity model. T. Cebeci presented a method [35] for the calculation of boundary layer characteristics on an oscillating airfoil, including flow reversal. Shamroth [36] applied a time dependent compressible turbulent Navier-Stokes analysis to the oscillating flow field problem. The test Reynolds number was 2,600,000. Turbulence

models are based on a turbulence energy equation. Baker and Yu [44] calculated detailed turbulence and velocity profiles and compared with Yu's data [21]. This is however limited to the steady state case. More fundamental work has been presented by Smith F.T. [37] about trailing edge separation and reattachement. An interacting flow theory is presented for a trailing edge flow with a one-side separation on a thin airfoil, where flow reattachement is imposed near trailing edge. This theory indicates the possibility of a vortex close to the trailing edge which turns in a sense opposite to the separation vortex. This behaviour is not confirmed by the experiment data of Smith [37]. Cebeci and Schimke [38] presented a viscous-inviscid interaction procedure for the computation of incompressible laminar separation bubbles in two- dimensional flows. Impressive data were presented by Mehta [1]. Dynamic stalled airfoil boundary layers were computed and results were verified with visualisations of Werle [33] in a qualitative way. Similar computations were presented by Sugavana and Wu [2]. No data comparisons were made in the latter cases.

The present review situates well the present work between previous and actual work done in the field of unsteady aerodynamics. To our knowledge only visualisations are available in the case of stalled flows around airfoils and it is believed that the present data meet an urgent need for experimental data.

TABLE 1 : FLAT PLATE EXPERIMENTS

Author	Type of experiment	Type of results
Cousteix et al [9,10,11,12] 1976-1981	with and without adverse pressure gradient separated flows rotating vanes high oscillation amplitude	instantaneous velocity and 3 Reynolds stress profiles; boundary layer thicknesses
Kenison [13] 1977	adverse pressure gradient separated flows	static pressure, skin friction
Parikh et al [14] 1981	time and space dependent pressure gradient bleeding off through test section wall	instantaneous velocity and 3 Reynolds stress profiles, boundary layer thicknesses
Patel [15] 1977	zero pressure gradient	overall averaged velocity and Reynolds stresses
Pericleus [16] 1977	adverse pressure gradient	overall averaged velocity and Reynolds stresses
Rakowsky [17] 1966	adverse pressure gradient	overall averaged velocity and Reynolds stresses
Simpson [18] Simpson et al [19] [20] 1979-1983	adverse pressure gradient near separation and separated	instantaneous static pressures, skin friction and two Reynolds stresses

TABLE 2 : AIRFOIL EXPERIMENTS

Author	Type of experiment
Yu [21]	.steady flow measurements in the vicinity of the trailing edge of a NACA 63-012 airfoil .velocity profiles and Reynolds stresses
Hah, Laksminarayana [22]	.steady flow measurements in the inner wake of a NACA 0012 airfoil at 3, 6 and 9 degrees incidence .velocity profiles and Reynolds stresses
Novak, Ramaprian [23]	.steady flow measurements in the wake of a NACA 0012 airfoil, measurements in the inner, near and far wake, velocity profiles and Reynolds stresses
Ramaprian et al [24]	.steady flow measurements in the wake of a Korn-Garabedian airfoil
Jansen, Mueller [25]	.steady flow measurements in the boundary layers of a NACA 66(3)-018 airfoil, two angles of attack, measurements in the laminar separation bubble
Satyarayana [26], Saxena [27]	.unsteady flow measurements, fixed airfoil in unsteady external flow, close to stall limit,
Covert et al [28]	.unsteady flow measurements in boundary layers of a fixed airfoil, rotating cylinders near trailing edge
Mc Croskey et al [6] [29]	.unsteady airloads on a pitching airfoil several airfoil types, Mach number, pitching amplitudes, stalled and non-stalled flows
Mc Alister, Carr [30]	.visualisation of unsteady flow around a pitching NACA 0012 airfoil
Robinson,Luttges [31] and Werle [33]	.visualisation of unsteady flow around a pitching NACA 0012 airfoil
Ho and Chen [32]	.unsteady flow measurement in the wake of a plunging airfoil
De Ruyck, Hirsch [4,5]	.unsteady flow measurements in the wake of a pitching NACA 0012 airfoil

3. Experimental set-up

3.1 Introduction

The complete set up is shown on figures 1 and 2. A single 45° slanted hot wire is used on a support fixed on a 60 cm chord pitching airfoil. This single rotating wire allows the determination of velocity magnitude and direction, and of all the Reynolds stresses in the boundary layers.

The probe support rotates in a plane normal to the local wall around its fixing point near the lower side of the airfoil (fig 1). At this fixation, a step motor is mounted which rotates the probe around its axis. A linear actuator, fixed on the opposite side of the airfoil, controls the distance of the sensor from the airfoil wall.

The airfoil position is measured through a resolver pick-up which is fixed on the oscillation axis of the airfoil.

Two pressure taps near leading edge and a pressure transducer mounted close to these taps yield a signal which is used to trigger the periodic sampling of the measured hot wire signals.

3.2 Oscillating airfoil

A 60 cm NACA 0012 airfoil is used for the present experiments. This airfoil is mounted in a 2 by 1 meter test section in one of the VUB blowdown windtunnels, where speeds of 17 m/s are reached at a free turbulence level less than 0.2 %.

Kraemer's rule [39] was used to design a tripping wire which is fixed at 10% chord distance from the leading edge. The tripping wire has a diameter of 0.3 % chord.

A sinusoidal motion is obtained with a crank-connecting rod mechanism, where a long connecting rod allows a motion which is sinusoidal within a few percent distorsion. The connecting rod is close to the tunnel wall. An overdimensioned asynchronuous motorreductor yields a stable frequency.

3.3 Probe support

A support has been designed for experiments on the oscillating wall of the airfoil (fig 1). Following criteria were observed for the construction of the support.

1. maximum stiffness, minimum weigth.
2. minimum disturbance near mid span.
3. rotation axis positioning corresponding to maximum resolution.
4. possibility for detection of any flow angle.
5. possibility for remote positioning.

Condition 4 is essential with respect to the position of the rotation axis. This axis must be perpendicular to the 2D flow surfaces in order to detect any flow direction in a similar way. Fortunately, this condition suits well to all the other conditions : this positioning gives a resolution which is close to the optimal one [4] and it allows to put the rotation mechanism close to the lower tunnel wall, far away from mid-span. A maximum stifness can be given up to about 10% chord distance from the sensor, whereas the sensor part is small with regard to possible flow disturbances.

The distance between the sensor and the wall is varied through a rotation of the support around its lower fixation point. The sensor therefore describes a circular arc with a large radius (R ~ 80 % chord length) and remains close to mid-span at any distance from the wall. As a consequence, the rotation axis is not completely perpendicular to the 2D flow surfaces, which is a minor problem when processing the data however. The maximum distance from the wall is about 20 % chord.

A stepmotor is mounted on the lower fixation point, which allows the rotation of the probe-axis over 48 positions (each 7.5°). The distance from the wall is controlled by an accurate linear actuator (.0025 cm/step).

3.4 Hot wire apparatus

The used hot wire is a 45° slanted DISA gold plated hot wire type 55P02. The sensor diameter is .005 mm and the length is 1.25 mm. The wire is connected to a TSI CTA anemometer bridge. No linearisation of the hot wire signal is used in order to avoid phase distorsion. The calibration of the wire occurs in situ.

3.5 Data acquisition and real time control

Two Z80 micro-processors control the experiment and the data acquisition. One controls the rotation step motor and the linear probe actuator, whereas the other controls the data acquisition. The recorded signals are

- Hot wire signal (A to D converted)
- Pressure signal (A to D converted)
- Airfoil position (Digital)
- Probe rotation and actuator status (Digital)

These signals are recorded on a 2400 feet digital magtape.

Real time control is performed by a Tektronix 4051 computer which allows the full automatisation of the experiments with an autonomy of 4 to 5 hours. Experiments in stalled conditions take up to 30 hours for one boundary layer traverse.

4. Hot wire measurement technique

4.1 Introduction

The measurement of low speed flows with high turbulence and arbitrary flow direction is still a difficult task in experimental fluid dynamics. Recently, some progress has been presented by Thompson and Whitelaw [40]. In this technique called 'flying hot wire technique' the hot wire is in motion in such a way that a relative velocity is superimposed on the flow velocity which is to be measured. In this way problems of zero velocity detection and arbitrary flow direction are solved. Such a technique is difficult to apply in the present context however.

A technique has been developed where reversed flows are obtained from the angular calibration characteristics of a rotating slanted hot wire. This technique which is relatively simple allows accurate measurements within the small sensing area of a single wire (1 mm) whith no extra technical requirements, and is discussed in sections 4.3 and 4.4.

4.2 Velocity and turbulence determination

The method to determine main flow parameters as well as all non-zero Reynolds stresses with a single hot wire has its base in the works of Kool and De Grande at the Vrije Universiteit Brussel [41,42]. Improvements with regard to the optimisation of the probe position were developed by De Ruyck [4]. The basic theory of the rotating wire technique is briefly summarised in the following.

The anemometer voltage E and the effective cooling velocity Q_{eff} are related by the the King law through

$$E^2 = A + B\, Q_{eff}^C \qquad (1)$$

The velocity Q can be reconstructed from equation (1) through

$$Q_{eff} = Q\, (\cos^2\delta + k \sin^2\delta)^{1/2} \qquad (2)$$

The yaw angle δ is the angle between the velocity vector and the plane surface perpendicular to the wire and k is a correction factor. Differentiation of equation (2) yields

$$dQ_{eff} = A_Q dQ + A_\delta d\delta \qquad (3)$$

dQ and dδ can be written as functions of du, dv and dw, which represent the increases in velocity components u, v and w. In this way, equation (3) can be rewritten as follows

$$dQ_{eff} = A_u u' + A_v v' + A_w w' \qquad (4)$$

where du, dv and dw are replaced by u', v' and w', the (small) turbulent velocity fluctuations. Taking the RMS of the rhs and lhs of equation (4) yields

$$\overline{(dQ_{eff})^2} = \overline{(A_u u')^2} + \overline{(A_u v')^2} + \overline{(A_u w')^2} + 2\overline{A_u A_v u'v'} + 2\overline{A_u A_w u'w'} + 2\overline{A_v A_w v'w'} \qquad (5)$$

If the turbulence intensity is not too large ($\tau<10\%$) the fluctuations on A_u, A_v and A_w are small and equation (5) can be rewritten, for a two dimensional flow

$$\overline{(dQ_{eff})^2} = A_u^2\overline{u'^2} + A_v^2\overline{v'^2} + A_w^2\overline{w'^2} + 2A_u A_v \overline{u'v'} \qquad (6)$$

The Reynolds stresses appear in the rhs of equation (6), whereas A_u, A_v and A_w depend on the probe position only. The stresses $\overline{v'w'}$ and $\overline{u'w'}$ are zero in the present context. If the lhs of equation (6) is determined experimentally for at least 4 different probe positions, the 4 non-zero Reynolds stresses can be determined from equation (6).

In practice 19 positions are taken and a least square fit is used to determine the Reynolds stresses.

4.3 Reversed flow detection

The flow properties are determined from ensemble averaged hot wire data. About 200 periods are recorded with 240 sample data per period (every 1.5° phase angle). This is done for each of the 48 rotational position of the probe.

The hot wire is rotated over 360° where 48 rotational positions are considered. The rotation over 360° is necessary since reversed flows are

expected. Figure 3 shows a typical ensemble averaged directional response of the slanted hot wire. The minima in this response correspond to minimum angles between flow direction and hot wire. The two minima correspond to a correct forward attack of the wire and a adverse one where the wire is masked by one of the prongs (fig 3). In practice, the flow properties are determined from 19 of the 48 directional data points, which are chosen around the correct minimum in figure 3, where prong effects are small.

The flow direction can easily be determined from the directional wire response, but the determination of the flow sense is less straightforward.

Following procedure is followed to determine the correct flow sense.

- Minima in the hot wire directional response are determined from a harmonic analysis (the response on fig 3 is periodic). Two directions shifted over 180° are found.

- 19 data points are selected around these minima and used to determine the velocity magnitude and the non-zero Reynolds stresses. Both solutions are saved (240 times 2 data for one normal coordinate).

- Final results are determined by selection of one of the solutions for all the data points. This selection is done manually and has not been integrated in the automatic data reduction programs.

The selection of the correct solutions is based mainly on the continuity of the flow angle over one period. This is made possible by the high density of experimental data (240 data points, every 1.5° phase).

Figs 4 and 5 illustrate the selection procedure. On these figures a detailed record is given of the results around the separation time at mid chord (test case BL20, time steps 35 to 46, increasing incidence around 19 degrees). On figure 4 chordwise and normal relative velocity profiles are shown. The squares are the forward and the plus the reversed solutions. At the first time (35), the profile is known to be a non reversed one and the squares therefore denote the correct solution, the normal velocity is negative. From time 37 on, both chordwise velocity curves touch at zero velocity (upper figure), while the corresponding normal velocity profiles switch (lower figure). The continuity in the correct solution can clearly be seen and it is not difficult to determine where the squares are to be replaced by plus

in order to obtain the correct solution.

On figure 5, the corresponding velocity vectors are drawn. On the upper figure, all the forward solutions (squares) are drawn and it again clearly appears where there is to be switched from one solution to the other, which is done on the lower figure.

4.4 Zero mean velocity determination

When a mean flow velocity $\bar{q}$ becomes very small whereas the fluctuations q' are high ($\bar{q} < q'$) some difficulties arise when applying equations (1) and (2). These difficulties can best be described with the aid of figure 6.

On figure 6 the probability density of the velocity is shown for a one dimensional case. When $\bar{q}$ is large compared with q', all the values of the measured velocities are positive and no problems arise when averaging the velocity in order to obtain its mean value $\bar{q}$. When the fluctuations are of the same order as $\bar{q}$, negative velocities can be expected and the dashed probability curve extends towards negative values in figure 6. Since a hot wire detects only the velocity modulus, the solid line probability curve is measured. The mean value $\langle q \rangle$ of the measured solid probability curve is different from the mean velocity $\bar{q}$ and a correction is to be made on $\langle q \rangle$ in order to obtain the exact mean velocity $\bar{q}$.

This problem has been investigated (e.g. Castro [43]) but no practical correction rules have been found in the literature and the following procedure has therefore been developed in the present work. The dashed probality curve in figure 6 is assumed to be Gaussian and it can be expressed in function of the mean velocity $\bar{q}$ as follows, with q normalised

$$P(q) = \frac{1}{\sqrt{2\pi}} e^{-\frac{1}{2}(q-\bar{q})^2} \tag{7}$$

The solid probability curve $P'(q)$ can be derived from equation (7) and the mean value $\langle q \rangle$ of the solid curve is obtained from

$$\langle q \rangle = \int_{-\infty}^{\infty} q\, P'(q)\, dq \tag{8}$$

This mean value is easily found to be (see appendix 1)

$$\langle q \rangle = \sqrt{2/\pi}\, e^{-\frac{1}{2}\bar{q}^2} + \bar{q}\, \mathrm{erf}\left(\frac{\bar{q}}{\sqrt{2}}\right)] \qquad (9)$$

In a two dimensional flow with velocity components u and v, equations (7) and (8) can be rewritten as (with u and v normalised)

$$P(u,v) = \frac{1}{2\pi} e^{-\frac{1}{2}[(u-\bar{u})^2 + v^2]} \qquad (10)$$

$$\langle q \rangle = \iint_{-\infty}^{\infty} \sqrt{u^2+v^2}\, P(u,v)\, du\, dv \qquad (11)$$

Equation 10 is not subject to sign problems as discussed for the one dimensional approach. After some manipulation, the mean value $\langle q \rangle$ is found to be (appendix 1)

$$\langle q \rangle = \sqrt{\pi/2}\, \Phi(-1/2, 1; -\bar{q}^2/2) \qquad (12)$$

Φ is a degenerate hypergeometric function. From equations (9) or (12) it is in principle possible to determine the real mean velocity $\bar{q}$ from the measured mean values $\langle q \rangle$. When the turbulence is small, equations (9) and (12) both reduce to

$$\langle q \rangle = \bar{q} = \bar{u} \qquad (13)$$

An analytical expression for a full three dimensional flow has not been found. It however appeared that both equations (9) and (12) yield quite similar and satisfactory results. To avoid unacceptable computing times, an approximation for equations (9) and (12) has been searched, as follows

$$\langle q \rangle = \bar{q} + K\, e^{-\frac{1}{2} q^2} \qquad K \approx 1.2 \qquad (14)$$

K is a constant parameter which has been calibrated in such a way that a good zero-definition for the mean velocity is found for all the experiments. A good zero definition means that velocity profiles which are partially reversed should have a net and continuous shape when the velocity changes of sign. Eqs 9, 12 and 14 are illustrated on figure 7, where the difference between the measured $\langle q \rangle$ and the real $\bar{q}$ is drawn against $\bar{q}$. At large values of $\bar{q}$, the difference is zero, whereas at zero mean velocity the correction

becomes maximum.

More details about these theoretical considerations can be found in appendix 1.

5. Data reduction and computer requirements

A main problem in the present study is the acquisition and the processing of an enormeous amount of data. One traverse requires six (2400 ft 1600 bpi) magtapes storage and processing (240 MByte). About 10 GByte have in total been recorded and processed in the present experiments.

The amount of data to be recorded was chosen as a compromise between minimum requirements for obtaining an acceptable accuracy and acceptable measuring and processing efforts. The periodic averaging is done over about 200 periods at 240 data per period. The number of rotational positions was 48, which was the maximum possible with the used step-motors, and a minimum for detecting an arbitrary flow angle with precision. Only 20 of these positions were used to determine the velocity magnitude and the Reynolds stresses, hence about 20 times 200 = 4000 samples were used for the determination of velocity and Reynolds stresses in one data point, at each time step.

The measurements for one traverse in stall required about 30 hours. The global processing for each traverse required about 7000 System Seconds on a 170/750 CDC computer.

Final results are available on magtape (appendix 2).

6. Selection of test cases

The parameters which are to be chosen are : the oscillation amplitude, mean airfoil incidence and reduced frequency. These parameters have been chosen from the experience of past experiments in the wake of the same airfoil [5]. Following conditions were then tested.

mean incidence :	0°, 5°, 10°
	(no stall, stall onset)
amplitude :	+/- 1.7° and +/- 5°
	(low and high)
frequency coefficient :	0.36 to 1.01
	(low and high)

No full stall was reached in these experiments, since at that time there was no ability for measuring reversed flows in a accurate way. Small reversed flows were however detected close to the trailing edge in the test case WHA5 where the airfoil ascillated from 5° to 15° at a frequency coefficient of 1.01.

The test case WLA5 (5° to 15°, low frequency coefficient) has been reproduced in the present work, in order to match the results obtained in [5] with the present ones. Other test configurations from the wake measurements were not reproduced, since they are expected to be less relevant, whereas the interest for full stalled cases is more important.

The oscillation amplitude was chosen high, being the most relevant one (+/- 5°). The oscillation frequency was kept low (0.3) since at higher values the development of the vortex is too subject to the history of the vortex developed during the previous oscillation period.

Incidence ranges were chosen in such a way that a clear distinction can be made between a non-stalled, stall onset and deep stalled case. Following test cases are available, all at an oscillation frequency of +/- 5°.

Ident	incidence	freq. coeff.	Re	
BLA5	5 to 15	0.48	178,000	stall onset
BL15	5 to 15	0.3	300,000	non stalled
BL16	6 to 16	0.3	300,000	stall onset
BL18	8 to 18	0.3	300,000	stalled
BL20	10 to 20	0.3	300,000	stalled

Test case BL15 is a non stalled case where the incidence ranges from 5° to 15°. When the frequency is increased from 0.3 to 0.48 (BLA5), a flow separation near the leading edge occurs and a vortex is present during a small part of the oscillation period. When the frequency is kept constant but the mean incidence is increased with 1° (BL16), the flow separates at both the leading and the trailing edge. A very small vortex is present during a short time near leading edge. When the incidence is further increased, the leading edge vortex developes into a large separation vortex and a full dynamic stalled flow results (BL18 and BL20).

Measurements were performed at 7° to 17° incidence, k=0.3. These conditions correspond with the transition between stall onset and stalled conditions : stall sometimes initiated, sometimes not and no coherent results could be found.

Results are available at the chordwise positions x/c = 15.4, 24.0, 32.9, 41.5, 49.9, 60.4, 70.6 and 80.0 % chord

7. Results

Results of all the available test cases are summarized on figures 8 to 19. For all these test cases data are available at 240 time steps (each 1.5° phase shift). This high density was required for the reversed flow detection, in particular near the vortex front which developes within a short time.

On figures 8 to 14, the most relevant time steps have been selected from the available data. The time goes from the top to the bottom in each figure. The time step number (1 to 240), the instantaneous incidence (i) and the phase angle (f) are mentioned on each figure. The phase angle is defined through

$$i = i_o + 5 \sin f, \quad f = \omega t$$

Hence times 1 and 121 correspond to $i=i_o$, the mean incidence. Times 61 and 181 correspond to respectively the maximum and the minimum incidence times. The leftmost figures represent the instantaneous velocity vectors, the central ones the streamwise turbulent velocity fluctuations $\sqrt{u'^2}/Q_\infty$ and the rightmost ones minus the Reynolds stress $\overline{u'v'}/Q_\infty^2$. The scales are added below each figure. It is to be observed that no smoothing has been applied on the results, except on the Reynolds stress $\overline{u'v'}$ in the stalled cases. This smoothing has moreover been done in the time domain only, not in the space, which means that all the points at one time step, as they are shown in the results, are completely independent of each other.

Test cases BLA5 and BL15 are summarised on figures 8 and 9. In both cases the incidence ranges from 5° to 15° but the frequency coefficients are different : 0.3 for BL15 and 0.48 for BLA5. On figures 10 to 14 results of test cases BL16, BL18 and BL20 are shown. These tests are performed at the same frequency coefficient of 0.3 and only the mean incidence has been increased from 10° to 13°. On figures 15 to 18 some particular Reynolds stress profiles are discussed. On figure 19 finally some of the unstalled turbulence profiles are compared with standard flat plate turbulence data.

5 to 15 degrees k=0.3 NO STALL

Test case BL15 is shown on figures 8.a and 8.b where results are shown every 36° degrees phase shift.

On figure 8.a the incidence grows from the mean value 10° towards the

maximum incidence (time steps 1, 25, 49) and it next decreases (time steps 73,97). Following observations can be made

At the highest incidences (time steps 49 and 73), the boundary layer tends to separate in the last station, and it is believed that the boundary layer is lightly separated at the trailing edge. Turbulence levels at maximum incidence do not exceed 14 % and minimum levels are comparable to the turbulence levels as found by Klebanoff on constant pressure flat plate experiments [39]. The Reynolds stress at maximum incidence reaches overall values of 0.8 % Q.

On figure 8.b the incidence decreases towards its minimum value and no particularities are observed. All the turbulence levels are quite close to the flat plate Klebanoff levels.

5 to 15 degrees k = 0.48 STALL ONSET

The higher frequency case is shown on figure 9.a and 9.b. The following differences with respect to the lower frequency case are observed :

The flow has less tendency to separate at the trailing edge, and it is believed to not separate at all at this place. Whereas the situation has improved at the trailing edge by increasing the frequency coefficient, the situation has deteriorated at leading edge where a small vortex initiates at the maximum incidence times (not shown). This vortex affects the flow in the first two stations at the time steps 73 and 97 (14.8° and 12.9° decreasing incidence) and it disappears at about 11° incidence (not shown).

The turbulence increases to about 20 % of Q for $\sqrt{u'^2}$ and 1 % of Q^2 for $\overline{u'v'}$ in all the stations when the critical stall onset incidence is reached (time step 73 to 145, incidence decreasing from 15° to 7°). Peaks of resp. 35 % Q and 5 % Q^2 are observed in the first station.

Important scatter is observed around 0° phase angle in this particular testcase, even after smoothing the data. This scatter is observed at the same time in all the stations, although these results are completely independent of each other. No explanation has been found for this behaviour which is not observed in the other test cases.

6 to 16 degrees incidence k=0.3 STALL ONSET

The stall onset case BL16 is shown on figures 10.a and 10.b. The results are shown every 36° phase shift. The frequency is the same as for the unstalled case BL15 but the mean incidence has been increased with 1°.

On figure 10.a the incidence grows from the mean value 11° towards the maximum incidence (time steps 1, 25, 47) and it next decreases (time steps 73, 97). Following observations can be made :

A trailing edge separation initiates in the last station at time step 49. The incidence has reached the value of 15.8° and has exceeded the static stall limit of 14°. This separation must be present at the trailing edge at an incidence which must be close to the static stall limit.

During the next time steps this separation affects the flow further upstream, and at time step 73 (15.8° incidence), the whole boundary layer flow tends to separate. At the same time, a small but strong vortex is created close to the leading edge. This vortex however doesn't come to development and it disappears, together with the trailing edge separation as the incidence decreases towards its mean value 11° (time step 121, figure 10.b).

The flow is not really reversed during the trailing edge separation, whereas a strong reversal is observed at leading edge.

Following observations can be made about the corresponding turbulence properties shown on figures 10.a and 10.b.

Turbulence intensities range from about 8 %, which is close to the current levels as found by Klebanoff, to 18 % in the trailing edge separated flow (time steps 193 and 73). Peak values of 37 % are observed near the leading edge vortex. Maxima in the turbulence profiles in general correspond to the maxima in velocity gradients at any time, which is in accordance with the current turbulence models.

The Reynolds stress levels range from 0.24 % of Q^2 in unstalled conditions to 1.5 % of Q_∞^2 in both the trailing edge separated flow and the leading edge vortex. The value of 0.24 exceeds the flat plate levels of about 0.15 % of Q^2. The local value of Q however differs from Q_∞ and it is found that

$$Q \sim 1.1 \text{ to } 1.2\ Q_\infty$$

$$Q^2 \sim 1.2 \text{ to } 1.4\ Q_\infty^2$$

$$\frac{\overline{u'v'}}{Q^2} \sim 0.7 \text{ to } 0.8\ \frac{\overline{u'v'}}{Q_\infty^2}$$

hence the experimental levels reduce to 0.15 to 0.2 %, which is close to the flat plate values. Much scatter is present on the $\overline{u'v'}$ profiles in the leading edge vortex and these results should be considered as only indicative.

8 to 18 degrees k=0.3 STALLED

Test case BL18 is reported on figures 11 and 12. Figure 11 shows the complete oscillation period every 35° phase shift. On figure 12, a more detailed record is given of the vortex development which is shown every 6° phase shift.

On figure 10.a the incidence first grows from the mean value 13° to the maximum value 18° and it next decreases. At the first time step (time step 1, mean incidence), a normal boundary layer is observed, with a tendency for separation in the last station however. Trailing edge separation is present at the next time step (time step 25, 15.9°), where the incidence has exceeded the static stall limit. The leading edge vortex initiates at an incidence of 16.5° (not shown) which is close to the stall onset incidence of 16°. It is fully developed at the next time step (time step 49, 17.8°). A strong acceleration is observed close to the wall between the leading edge vortex and the trailing edge separation point. At the time step 73 (17.8° incidence), the leading edge vortex has left the sensed area which extends up to about 25 % chord distance from the wall. When the incidence decreases (time step 77), a second vortex developes and its evolution can be observed on figure 11.b.

On figure 11.b, the incidence further decreases towards its minimum value of 8°. The second vortex has developed to a large separated low speed flow field where a clear separation line starts from tne leading edge and is almost parallel to the main flow direction. This low speed flow is finally blown away as the incidence reaches its minimum value (time steps 145, 169,

193).

Minimum overall turbulence levels of about 8 % are again found when the boundary layer is not separated (time step 193, figure 11.b). This level increases towards 20 % before the separation occurs (time step 25, 15.9°). When the flow is separated, peak values up to 40 % are observed, in particular near leading edge. Maximum values in the turbulence profiles in general correspond to maximum velocity gradiends, even when the flow is separated, which is again in accordance with current turbulence modeling. These maxima indicate the separation line which lies just beyond.

Although much scatter is present on the $\overline{u'v'}$ profiles in figures 11.a and 11.b, a good structure can be observed in the Reynolds stress. High values (4.5 % Q^2) are found just above the separation line (time step 121, figure 11.b), whereas the minimum unstalled stresses range within the flat plate Klebanoff levels.

An interesting observation is that the stress which in general has a sign opposite to that of the velocity gradient dU/dy, indicating turbulent energy production, gets an unusual sign inside the vortex. The sign of the stress changes two times in several profiles (in particular at time 97, 15.9°, figure 11.a), whereas the mainstream velocity gradient remains positive. This behaviour disappears as the incidence decreases towards its minimum value (figure 11.b). The turbulent energy production is given by

$$\text{production} = - \overline{u'v'} \left(\frac{\partial U}{\partial y} + \frac{\partial V}{\partial x} \right)$$

This production can easily be calculated from the experimental data and two production profiles are shown on figure 15. Stress profiles corresponding to stations 3 and 4 for time step 94 (17°) are drawn as well as the correponding turbulent energy profiles. On figures 16 and 17, superpositions are made of velocity and turbulence for time steps 94 (see figure 15) and 104. From figures 15 and 16 it can be seen that turbulent energy is returned from the vortex center to the main flow, through negative values of the energy production.

The same behaviour is also well observed just before the leading edge separation occurs. On figure 18 negative stresses are observed which clearly correspond to velocities which are still not reversed and they may indicate the coming vortex development.

More details about the vortex development are shown on figure 12. Near maximum incidence (times 60, 64), the vortex center is near mid chord and it leaves the sensed area which extends up to about 25 % chord distance from the wall. When the incidence starts to decrease, a second vortex develops which can be observed in station 3 to 5 at the time steps 76 to 92. This second vortex is smaller, it is not created at leading edge but more downstream. The second vortex moves downstream more slowly than the first one : this velocity is about 10 % of Q against 60 %. The second vortex remains closer to the wall and it 'diffuses' into a large scale low speed reversed flow.

10 to 20 degrees k = 0.3 STALLED

Figures 13 and 14 represent results obtained at a higher main incidence. The qualitative behaviour and the overall turbulence levels in this test case is very similar to those of the previous test case BL18, except that the trailing edge separation is present throughout the whole period. The first leading edge vortex initiates at the same incidence of 16.5 degrees (figure 14, time step 14). It rapidly leaves the sensed area. A second vortex can again be observed (figure 14, time steps 62 to 94), although it is less clear than in the previous case. The scatter on the Reynolds stress is important, but a good structure is again observed, in particular on figure 13.b. The reenergizing through positive signs of $\overline{u'v'}$ can again be observed on figure 13.a, time steps 73 and 97.

Comparison with flat plate boundary layer data

Some of the unstalled turbulence profiles of case BL15 are compared with data obtained by Klebanoff [39] on a flat plate at constant pressure gradient. On figure 19.a to 19.d the four non-zero turbulence stress profiles are compared at four times during the oscillation period at x/c = 60.4 % chord. At 270° phase angle (minimum incidence 5°) the pressure gradient is the most favourable for the boundary layer and the results (squares) are quite close to the Klebanoff data (solid lines). In all other cases, increased levels are observed, with maximum values in the most critical situation (figure 19.b, 15° incidence). In this situation the Reynolds stress exceeds the Klebanoff profile by about 5 times. Maximum values in these profiles are shifted towards the middle of the boundary layer, which corresponds with a shift in the maximum velocity gradient $\partial U/\partial y$.

The present comparison indicates a good coherence with standard data such as those obtained by Klebanoff.

Comparison with computed data

Some computed results obtained by Mehta [1] are reproduced on figure 20. The test conditions for these results are different from the present ones. The Reynolds number is 10,000, the frequency coefficient 0.25 and the airfoil oscillates from 0° to 20°. Some similarity with the present results is found however : the presence of two vortices is observed in the same way as in the present experiments and a similar acceleration between leading edge vortex and trailing edge separation is observed on figure 13.a (time 25).

This similarity between the measured and computed flow configurations lends support to the negligible influence of the tripping wire on the measured flow structure. So more, that the length scale of the leading edge vortex is much larger than the scale of the tripping wire. It is to observed that no turbulence modeling was used by Mehta when computing the flow.

Accuracy

The error levels are strongly dependent on the turbulence levels, in particular when the flow is stalled.

Random errors are in general small, since the scatter on most of the results is small although they are obtained without smoothing. An exception is to be made for the Reynolds stress $\overline{u'v'}$ in the stalled flows however. For these results random errors are excessive and the results are sometimes to be considered as indicative. The random error on the velocity varies between 1 and 5 %. The scatter un the $\sqrt{u'^2}$ profiles varies between 2 and 10 %. The $\overline{u'v'}$ stress in test cases BL15, BLA5 and BL16 is unsmoothed and the scatter reaches about 10 % outside of the leading vortex. This scatter has been reduced by a time smoothing procedure which is given in appendix 3.

Systematic errors are dependent on the accuracy of the wire calibrations and on the resolution of the data acquisition system (0.4 %). The hot wire calibrations are automaticaly included before and after each experiment, whereas intermediate reference recordings are programmed during the long experiments (up to 30 hours). In this way calibration errors are reduced to a minimum which is of the same order as the acquisition resolution.

Systematic errors on the velocity can therefore be considered as about 1 % of Q. The systematic error on the turbulence properties in unstalled flows is more important due to the linearisation of equation 5. In stall this linearisation is believed to induce errors of 5 to 10 %. Errors of 1 to 2 % are induced in non-stalled conditions.

Conclusions

A technique for velocity and turbulence measurements in dynamic stalled flows has been summarised and applied in the boundary layers of an oscillating airfoil. Measurements are made in unstalled, stall onset and full dynamic stalled conditions at 8 chordwise positions along the suction side of the airfoil.

Detailed pictures of leading edge vortices and trailing edge separations are found. Two leading edge vortices are detected and the Reynolds stress indicates a reenergizing of the mean flow from the turbulence in the separation vorticies. Strong vorticities are observed at leading edge, whereas the trailing edge separated flow is of low velocity. A close similarity is observed with computed results on different but similar conditions.

Turbulence levels in the non-stalled flows are found to correspond to current smooth wall turbulence levels, whereas the turbulence levels in separated flows reach 40 % of Q and the Reynolds stress 4 % Q_∞^2.

Trailing edge separation is observed when the incidence exceeds the static stall limit of 14° at k=0.3. This tendency is decreased as the frequency coefficient is increased. Leading edge vortices initiate at 16.5° fot k=0.3 and below 15° at k=0.48. At stall onset, the leading edge vortex doesn't develop, contrarily to the full stalled cases.

Detailed velocity and turbulence data are made available for direct data comparison with computational results of Navier Stokes calculations on oscillating airfoils at high Reynolds numbers.

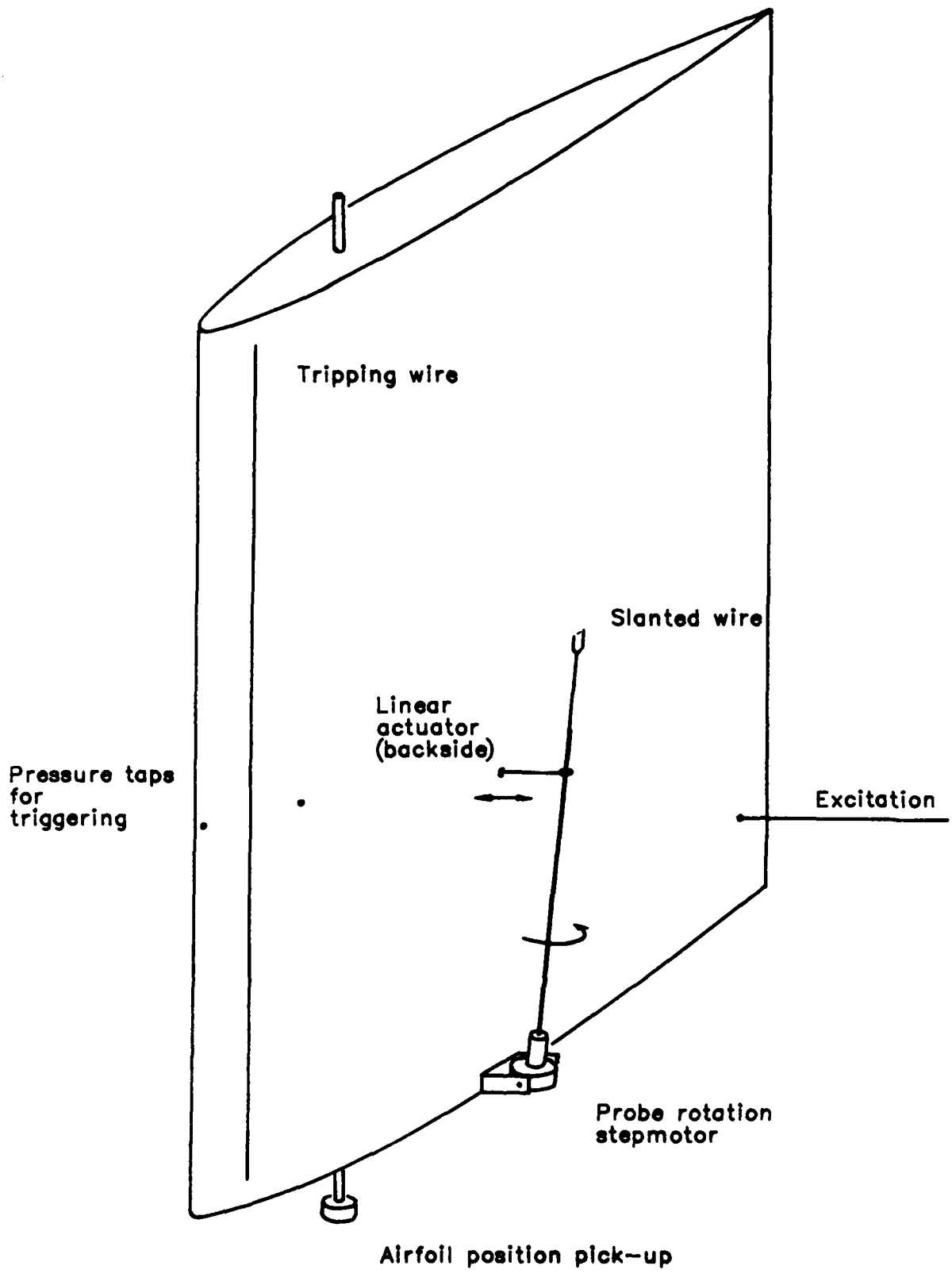

Figure 1 : Experimental set up

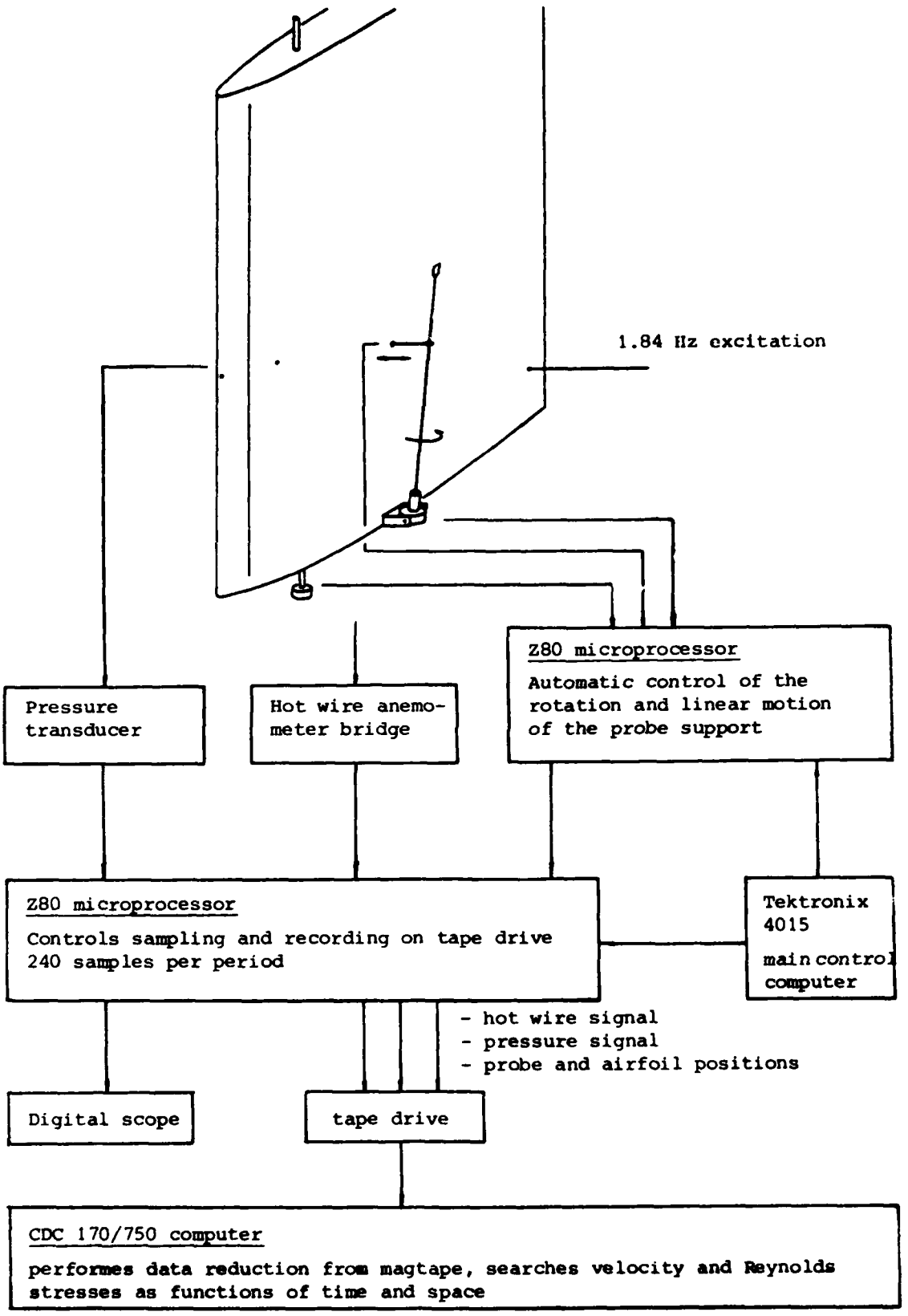

Figure 2 : Data acquisition

REVERSED FLOW DETECTION

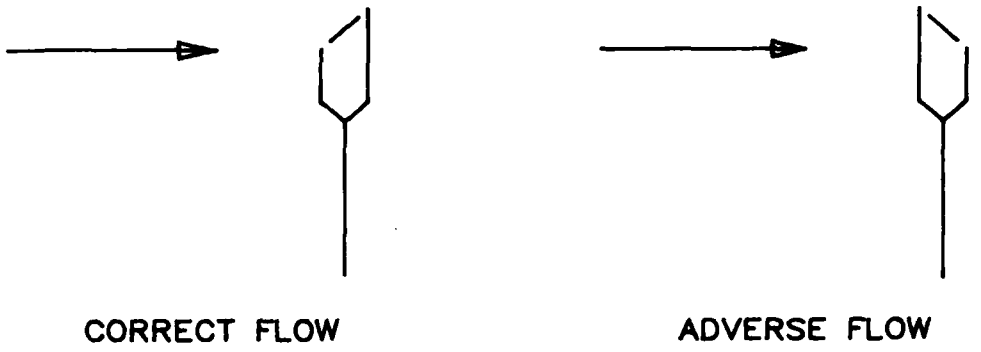

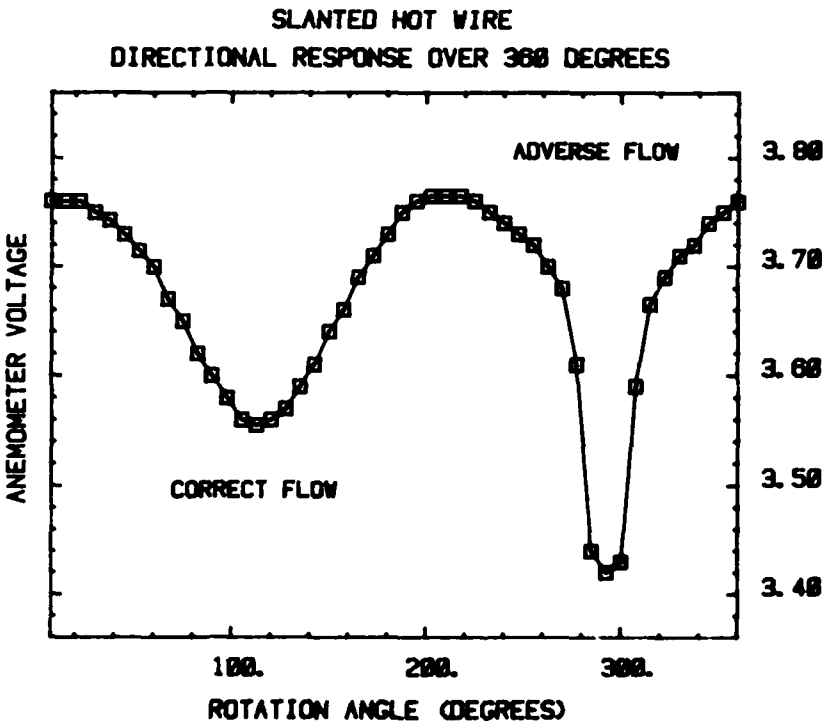

Figure 3 : Reversed flow detection

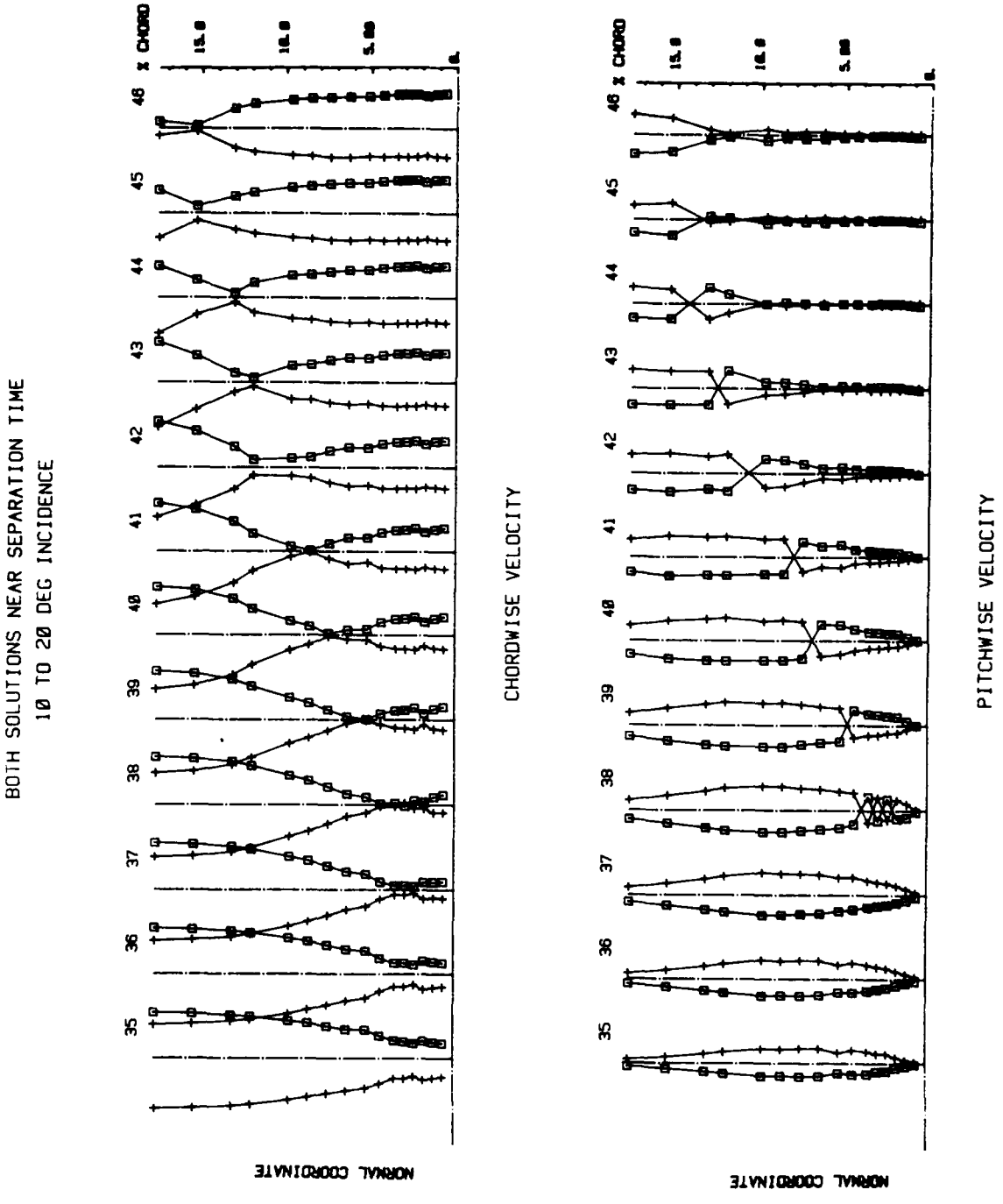

Figure 4 : Forward and reversed solutions near separation time

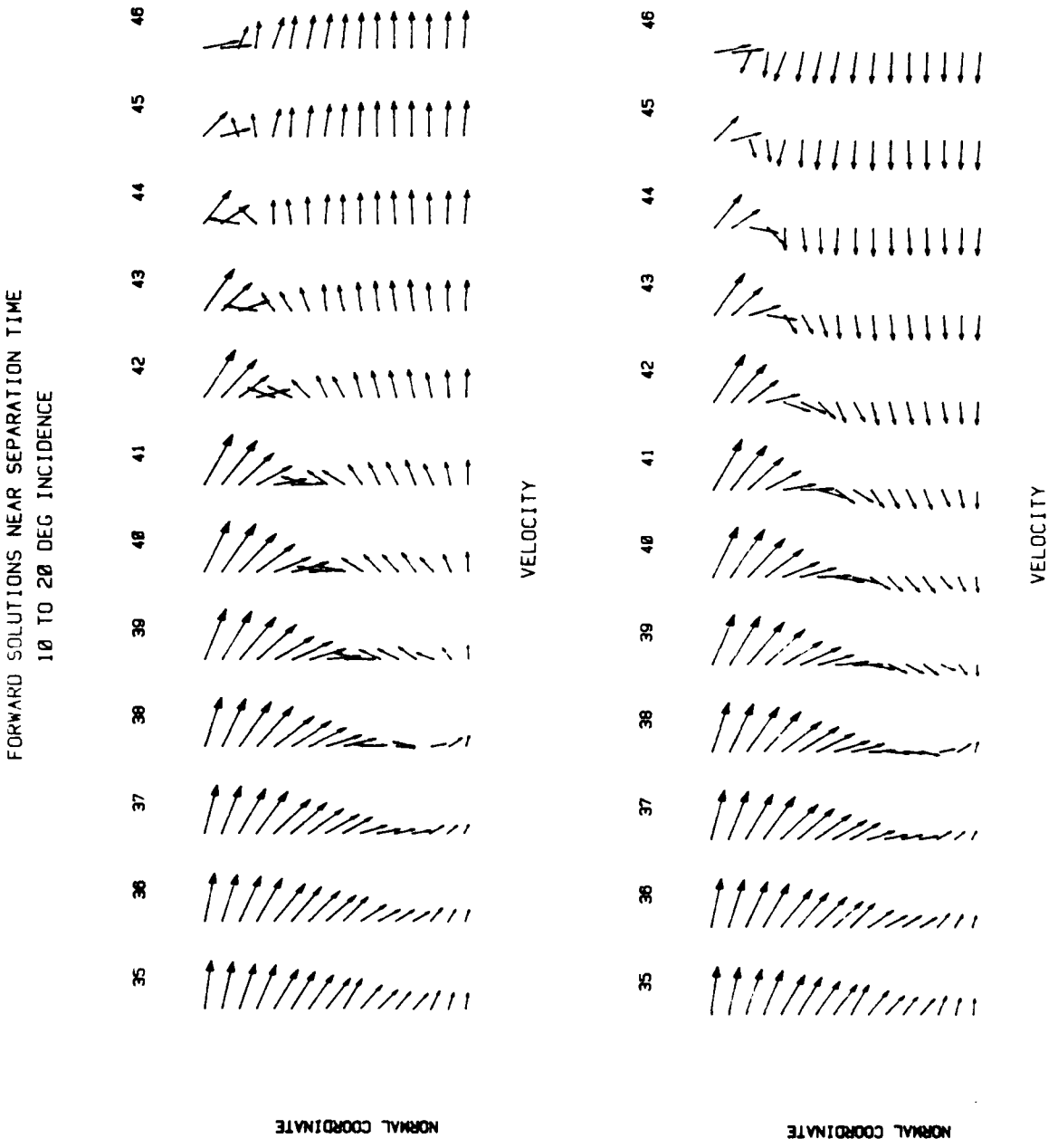

Figure 5 : Forward (left side) and correct (right side) solutions near separation time

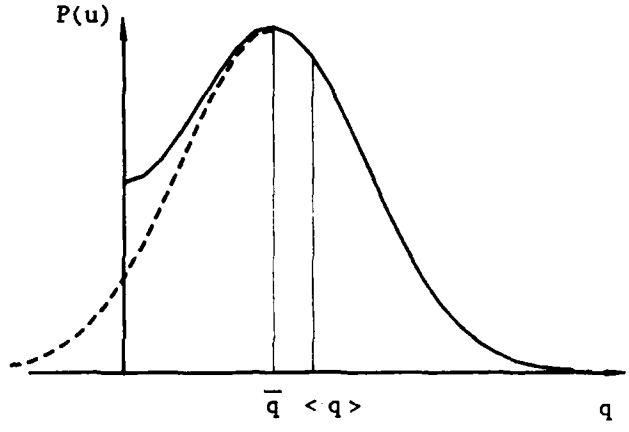

Figure 6 : One dimensional velocity probability curve

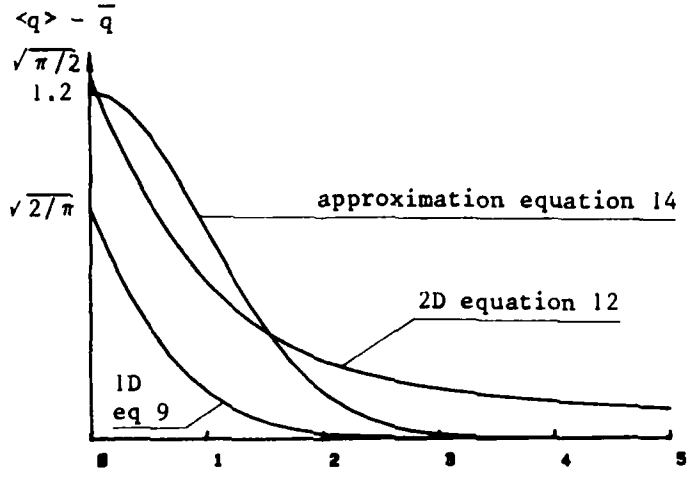

Figure 7 : Corrections for zero
mean velocity determination

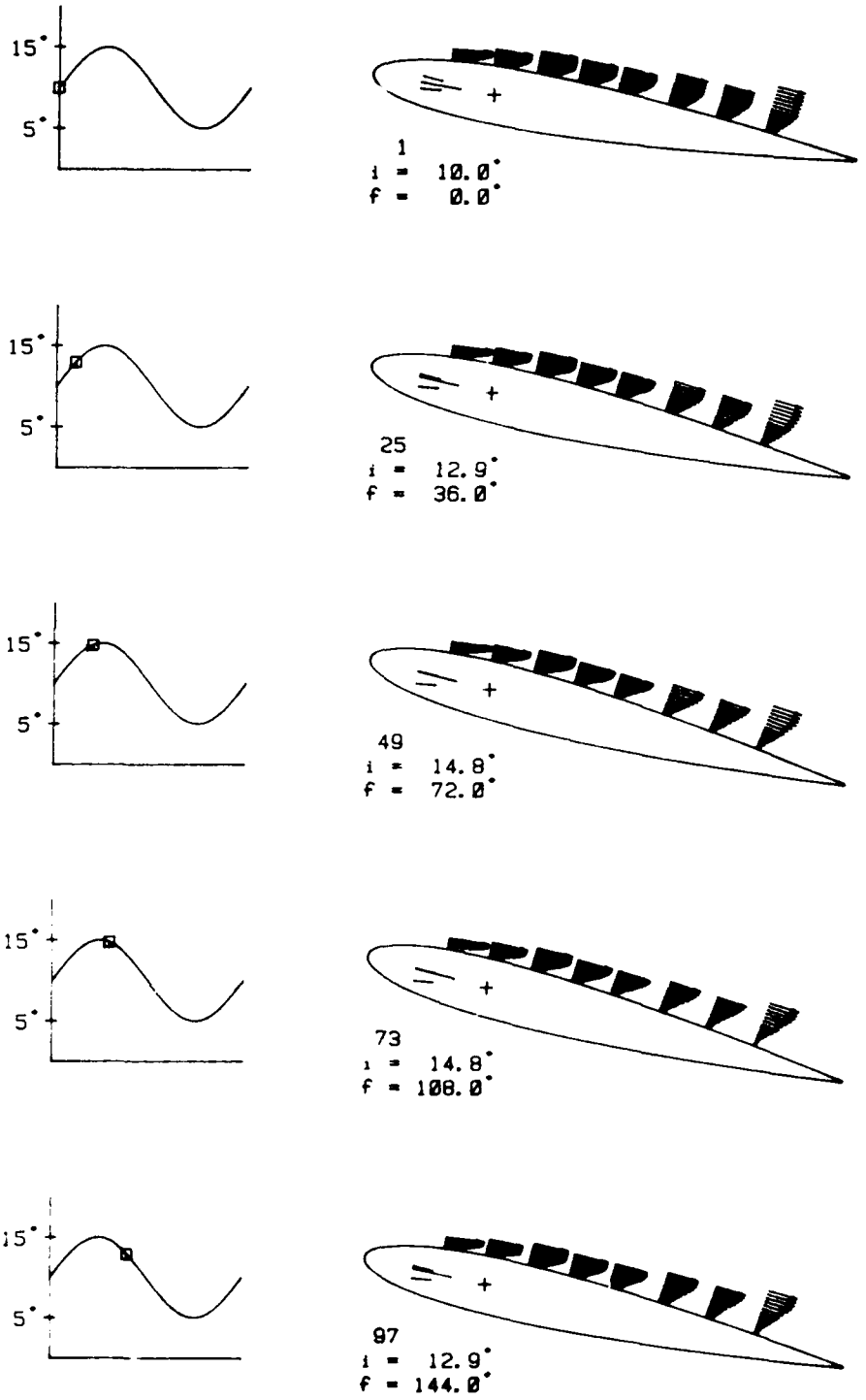

Figure 8.a :

Test case BL15 : 5° to 15° incidence, $\kappa = 0.3$, no stall

Velocity vectors scale : — Q

i : incidence f : phase angle

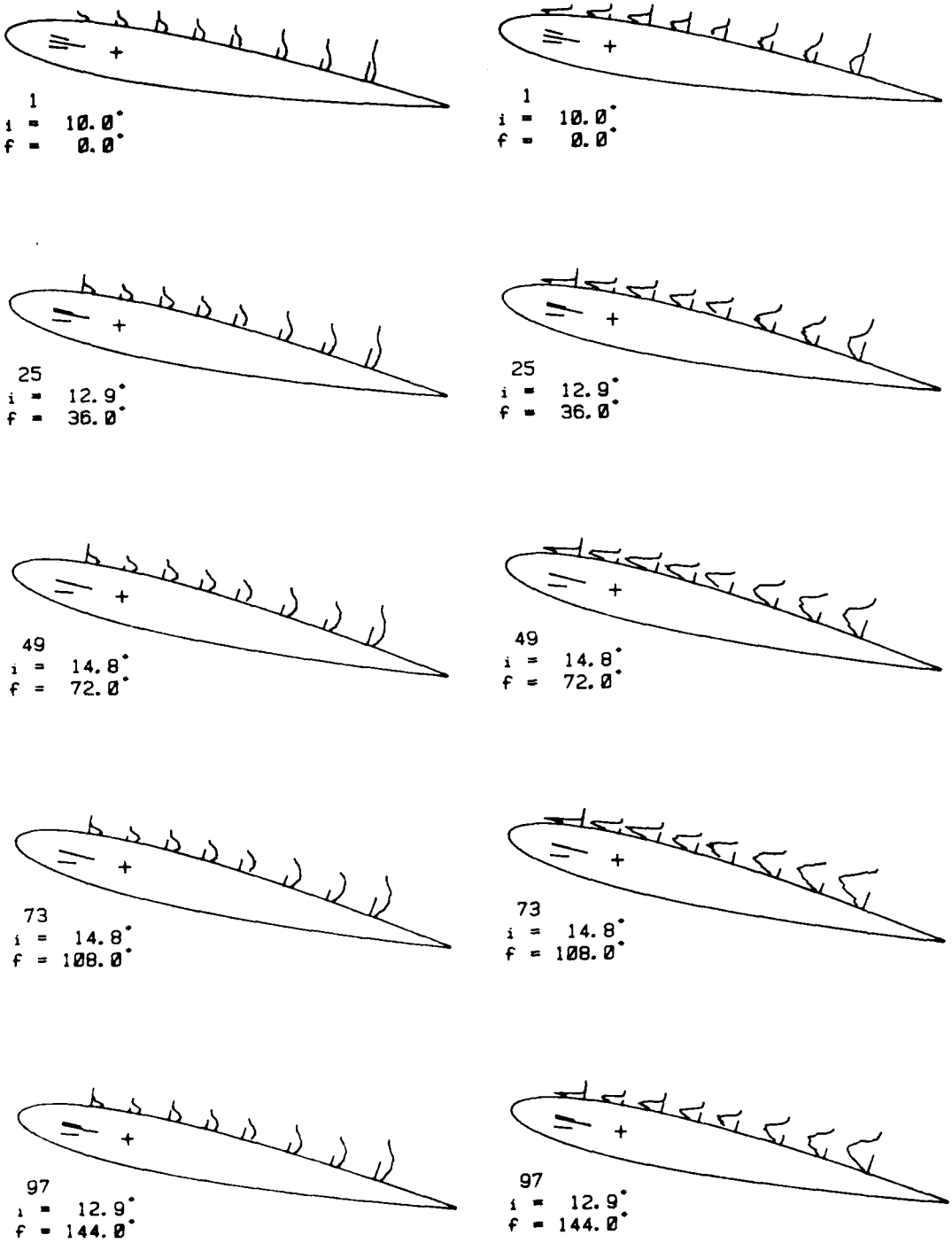

Figure 8.a (continued) :

Test case BL15 : 5° to 15° incidence, k = 0.3, no stall

Left : Chordwise fluctuations $\sqrt{u'^2}/Q$ scale : — 30% Q

Right : Reynolds stress $-\overline{u'v'}/Q^2$ scale : — 0,75% Q^2

i : incidence f : phase angle

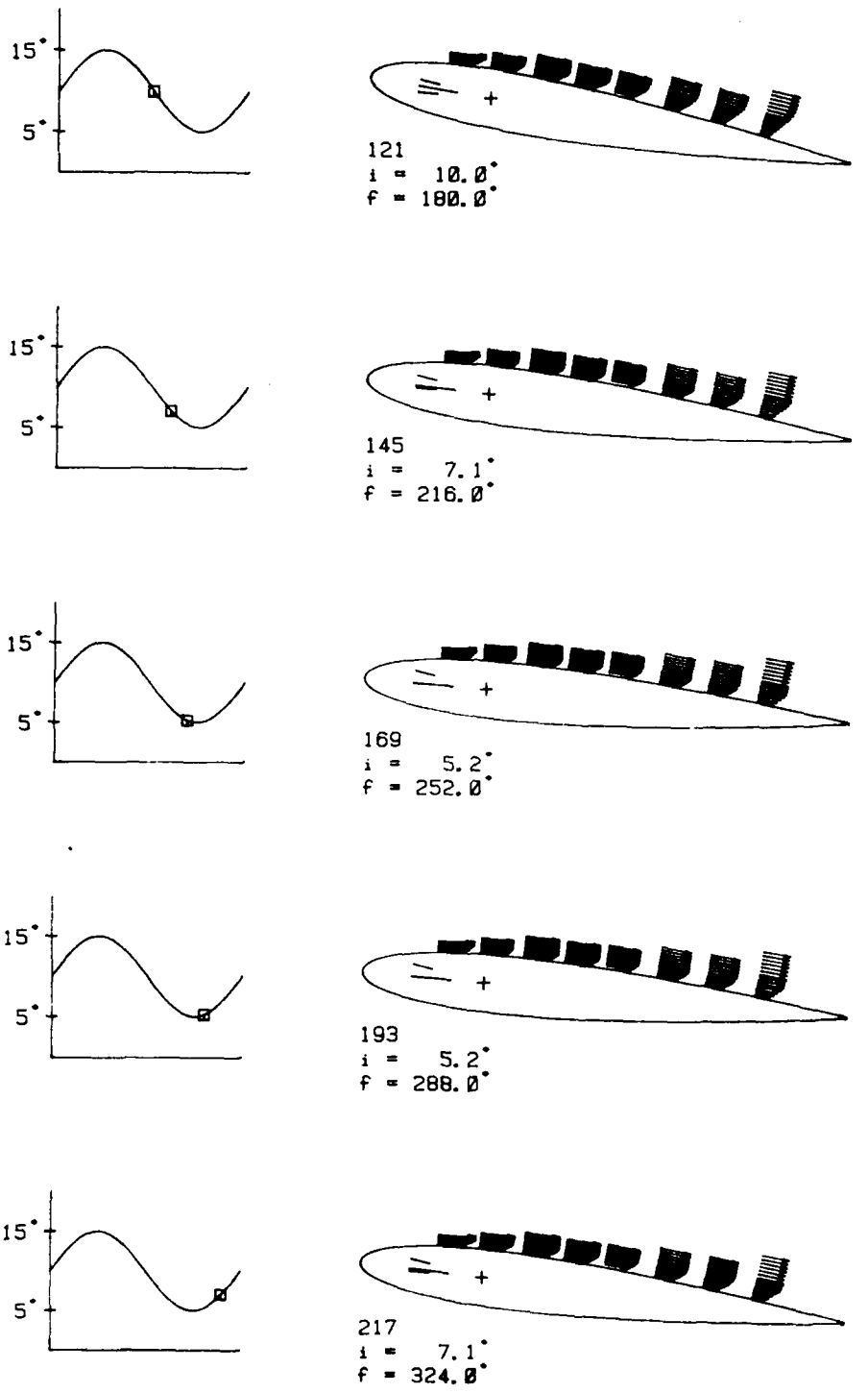

Figure 8.b :

Test case BL15 : 5° to 15° incidence, k = 0.3, no stall

Velocity vectors scale : — Q

i : incidence f : phase angle

121
i = 10.0°
f = 180.0°

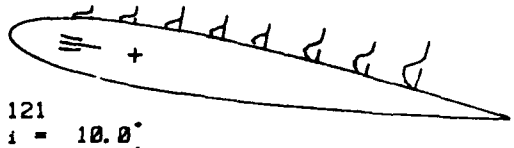

121
i = 10.0°
f = 180.0°

145
i = 7.1°
f = 216.0°

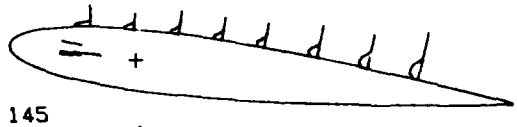

145
i = 7.1°
f = 216.0°

169
i = 5.2°
f = 252.0°

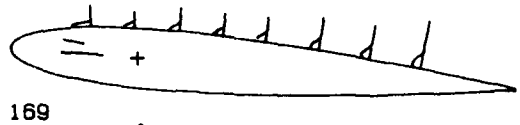

169
i = 5.2°
f = 252.0°

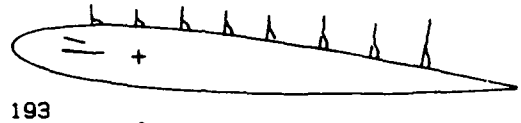

193
i = 5.2°
f = 288.0°

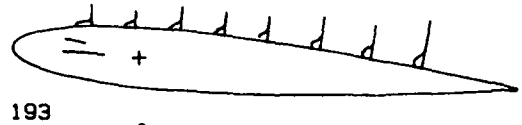

193
i = 5.2°
f = 288.0°

217
i = 7.1°
f = 324.0°

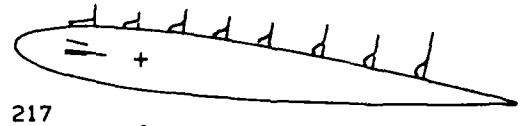

217
i = 7.1°
f = 324.0°

Figure 8.b (continued) :

Test case BL15 : 5° to 15° incidence, k = 0.3, no stall

Left : Chordwise fluctuations $\sqrt{u'^2}/Q$ scale : — 30% Q

Right : Reynolds stress $-\overline{u'v'}/Q^2$ scale : — 0,75% Q^2

i : incidence f : phase angle

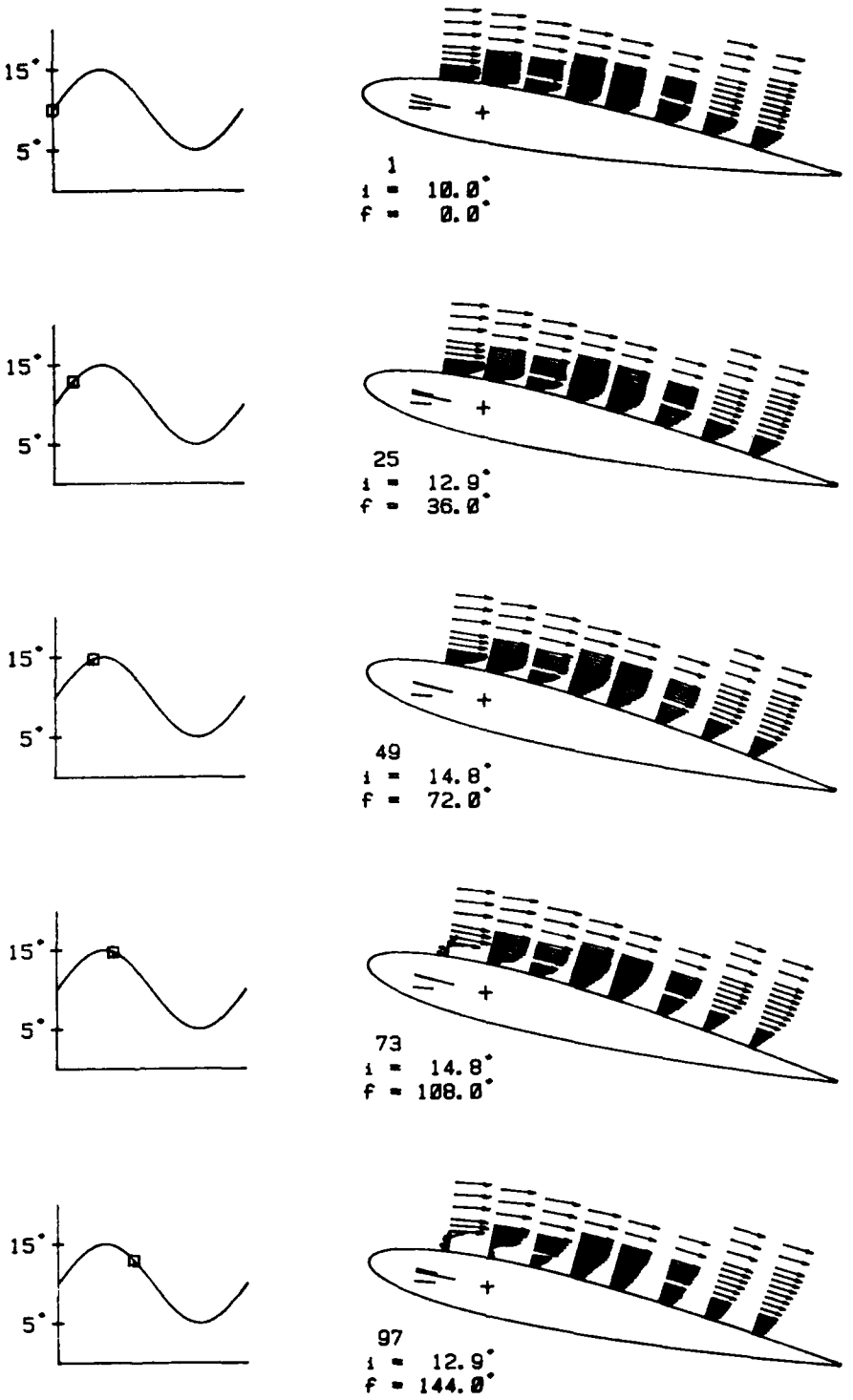

Figure 9.a :

Test case BLA5 : 5° to 15° incidence, k = 0.48, stall onset

Velocity vectors scale : — Q

i : incidence f : phase angle

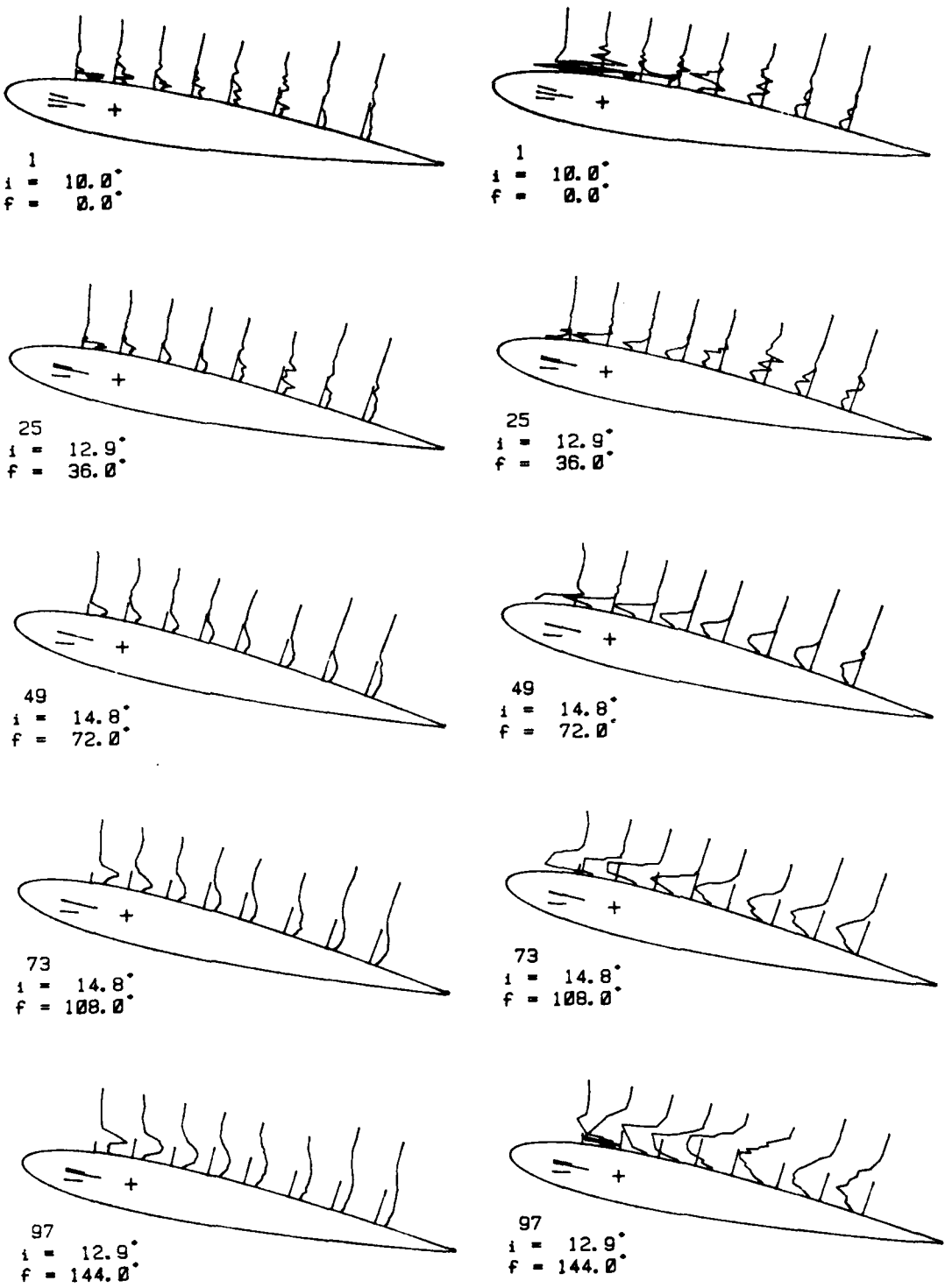

Figure 9.a (continued) :

Test case BLA5 : 5° to 15° incidence, k = 0.48, stall onset

Left : Chordwise fluctuations $\sqrt{u'^2}/Q$ scale : — 30% Q

Right : Reynolds stress $-\overline{u'v'}/Q^2$ scale : — 0,75% Q^2

i : incidence f : phase angle

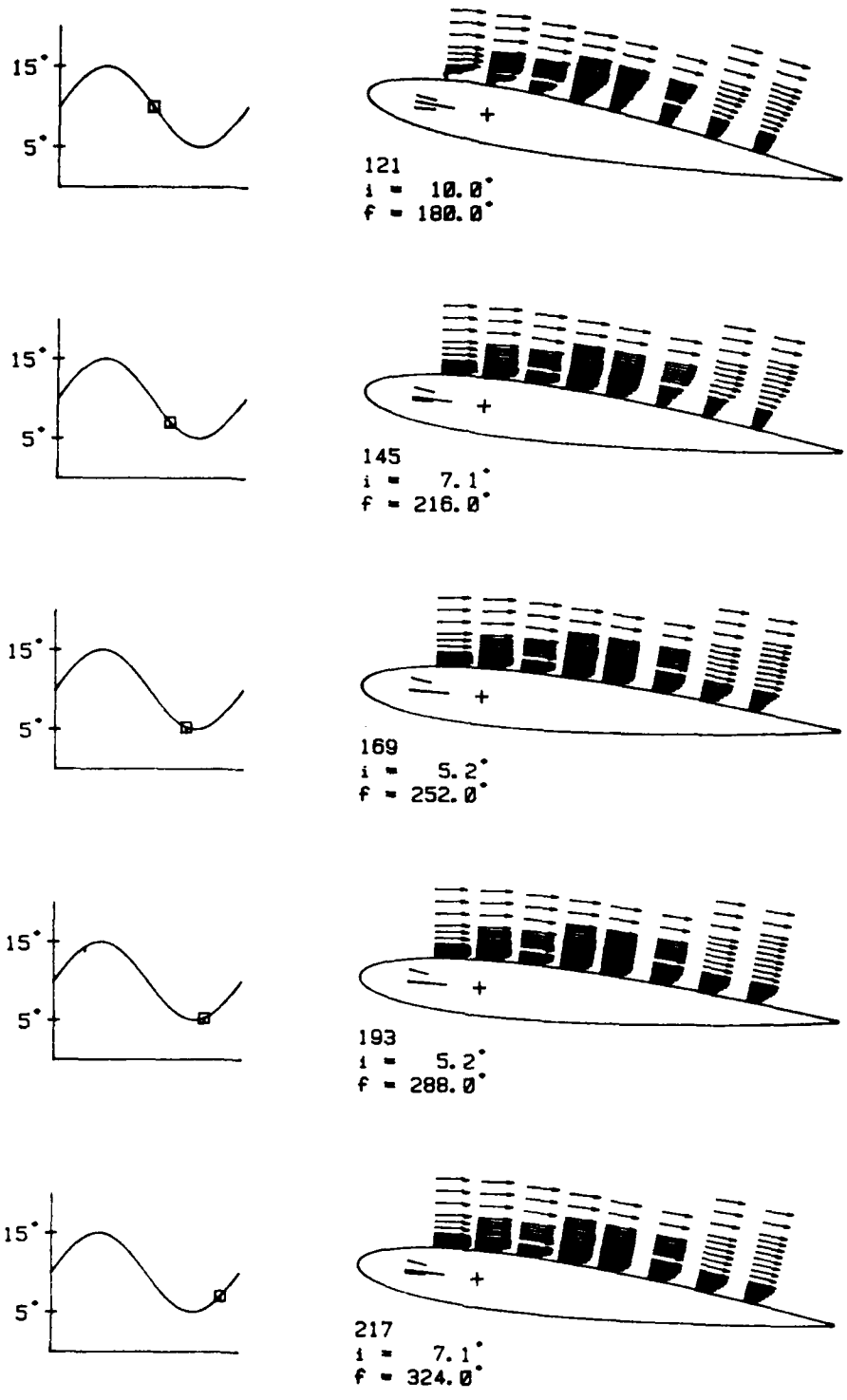

Figure 9.b :

Test case BLA5 : 5° to 15° incidence, k = 0.48, stall onset

Velocity vectors scale : — Q

i : incidence f : phase angle

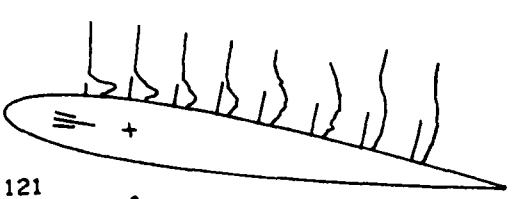

121
i = 10.0°
f = 180.0°

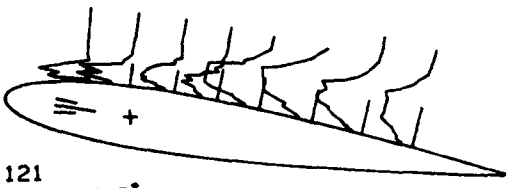

121
i = 10.0°
f = 180.0°

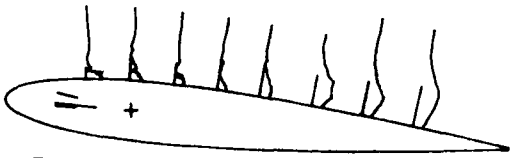

145
i = 7.1°
f = 216.0°

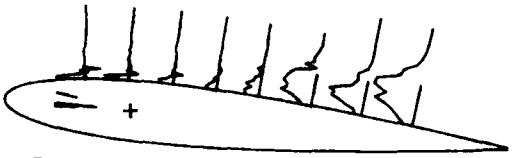

145
i = 7.1°
f = 216.0°

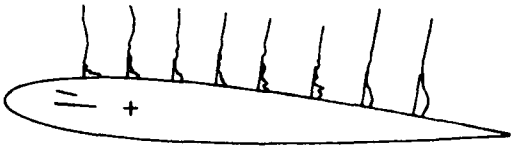

169
i = 5.2°
f = 252.0°

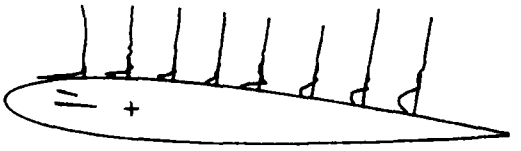

169
i = 5.2°
f = 252.0°

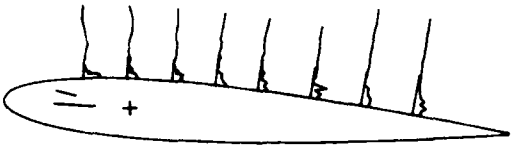

193
i = 5.2°
f = 288.0°

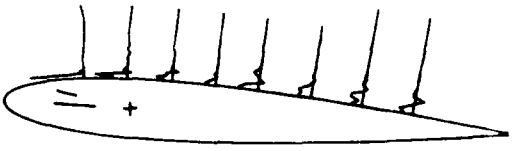

193
i = 5.2°
f = 288.0°

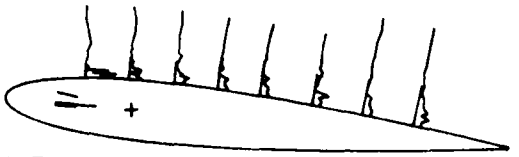

217
i = 7.1°
f = 324.0°

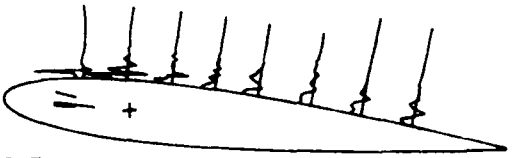

217
i = 7.1°
f = 324.0°

Figure 9.b (continued) :

Test case BLA5 : 5° to 15° incidence, k = 0.48, stall onset

Left : Chordwise fluctuations $\sqrt{u'^2}/Q$ scale : — 30% Q

Right : Reynolds stress $-\overline{u'v'}/Q^2$ scale : — 0,75% Q^2

i : incidence f : phase angle

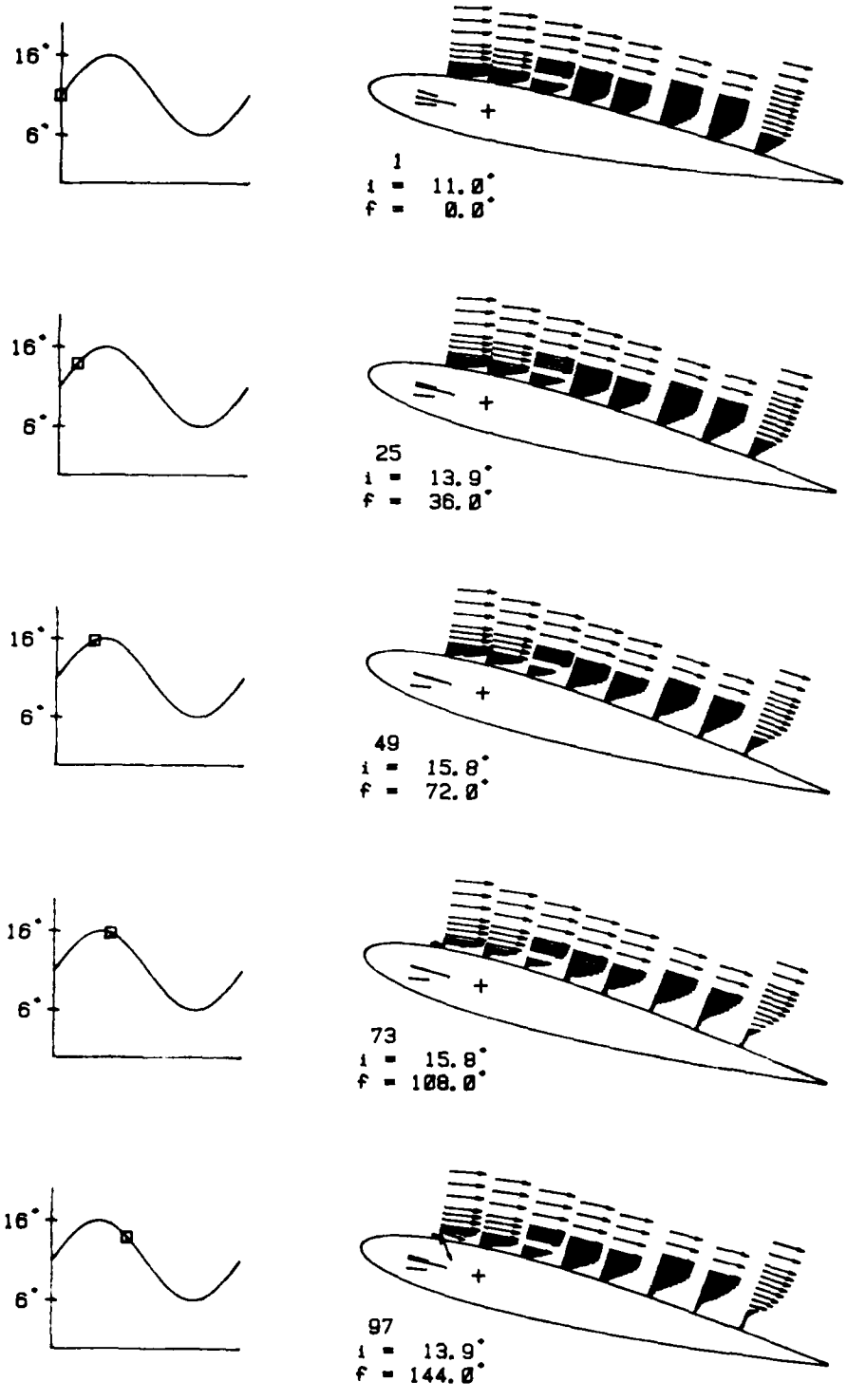

Figure 10.a :

Test case BL16 : 6° to 16° incidence, k = 0.3, stall onset

Velocity vectors scale : — Q

i : incidence f : phase angle

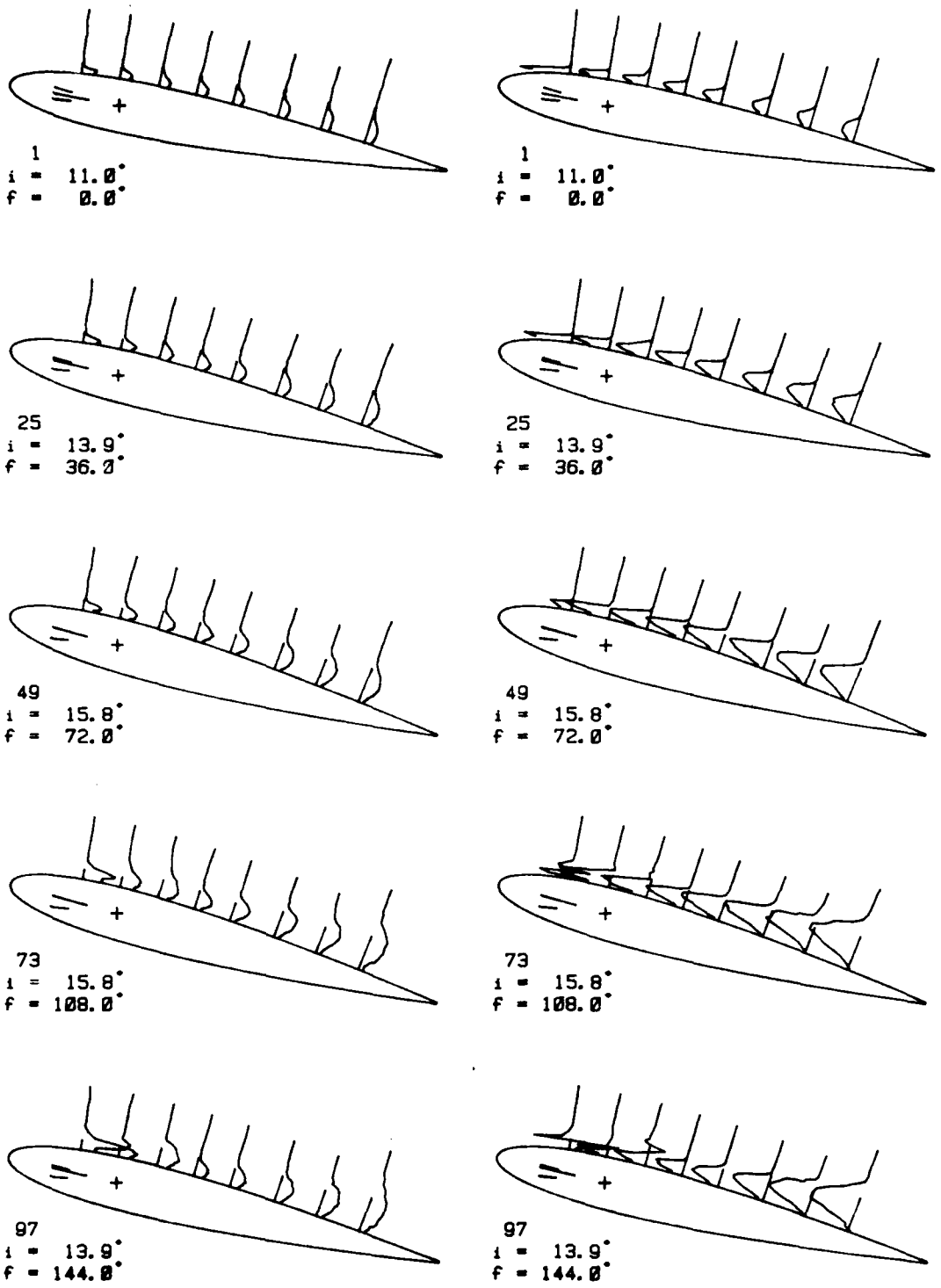

Figure 10.a (continued) :

Test case BL16 : 6° to 16° incidence, k = 0.3, stall onset

Left : Chordwise fluctuations $\sqrt{u'^2}/Q$ scale : — 30% Q

Right : Reynolds stress $-\overline{u'v'}/Q^2$ scale : — 0,75% Q^2

i : incidence f : phase angle

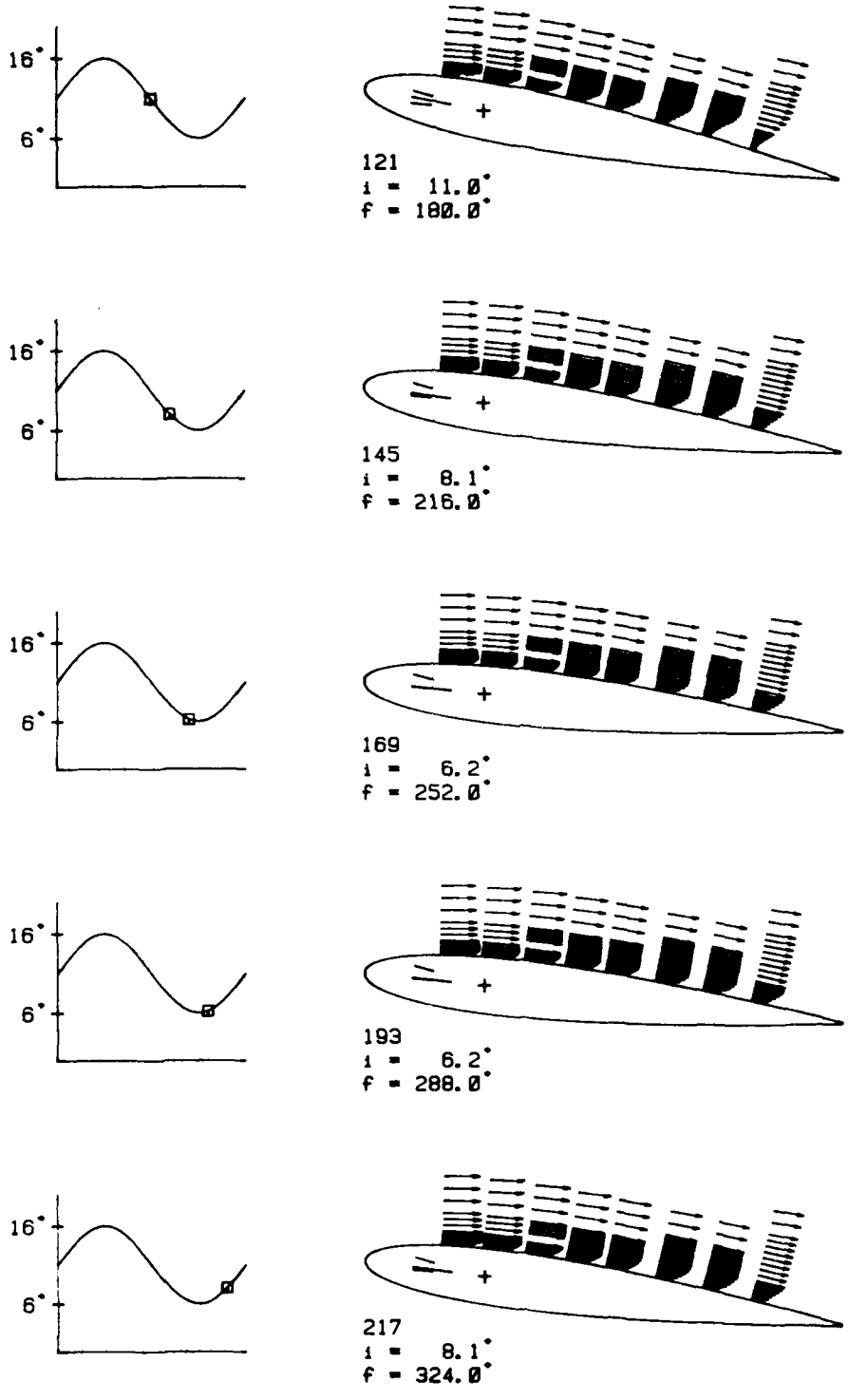

Figure 10.b :

Test case BL16 : 6° to 16° incidence, k = 0.3, stall

Velocity vectors scale : — Q

i : incidence f : phase angle

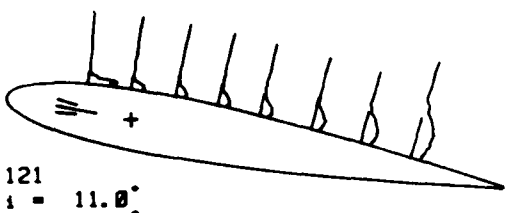

121
i = 11.0°
f = 180.0°

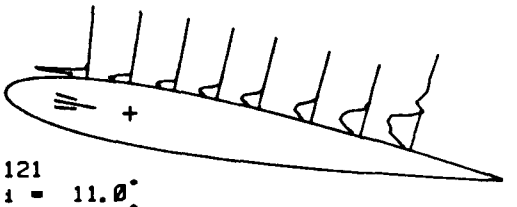

121
i = 11.0°
f = 180.0°

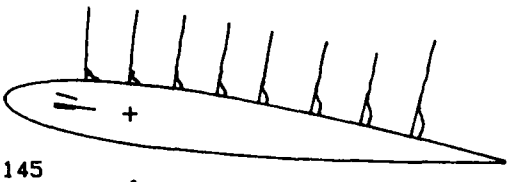

145
i = 8.1°
f = 216.0°

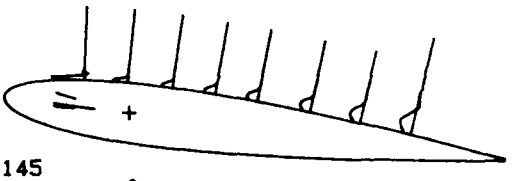

145
i = 8.1°
f = 216.0°

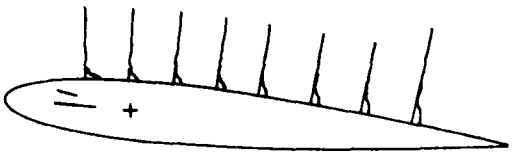

169
i = 6.2°
f = 252.0°

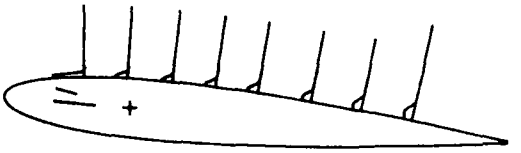

169
i = 6.2°
f = 252.0°

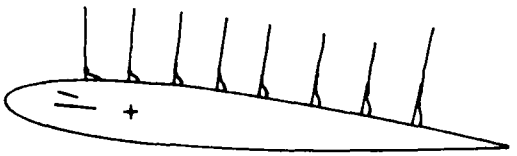

193
i = 6.2°
f = 288.0°

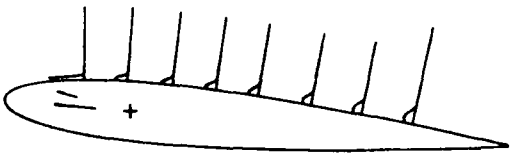

193
i = 6.2°
f = 288.0°

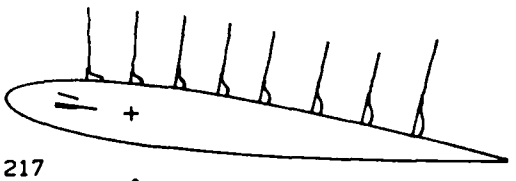

217
i = 8.1°
f = 324.0°

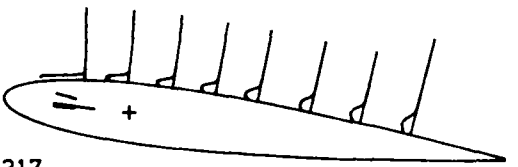

217
i = 8.1°
f = 324.0°

Figure 10.b (continued) :

Test case BL16 : 6° to 16° incidence, k = 0.3, stall

Left : Chordwise fluctuations $\sqrt{u'^2}/Q$ scale : — 30% Q

Right : Reynolds stress $-\overline{u'v'}/Q^2$ scale : — 0,75% Q^2

i : incidence f : phase angle

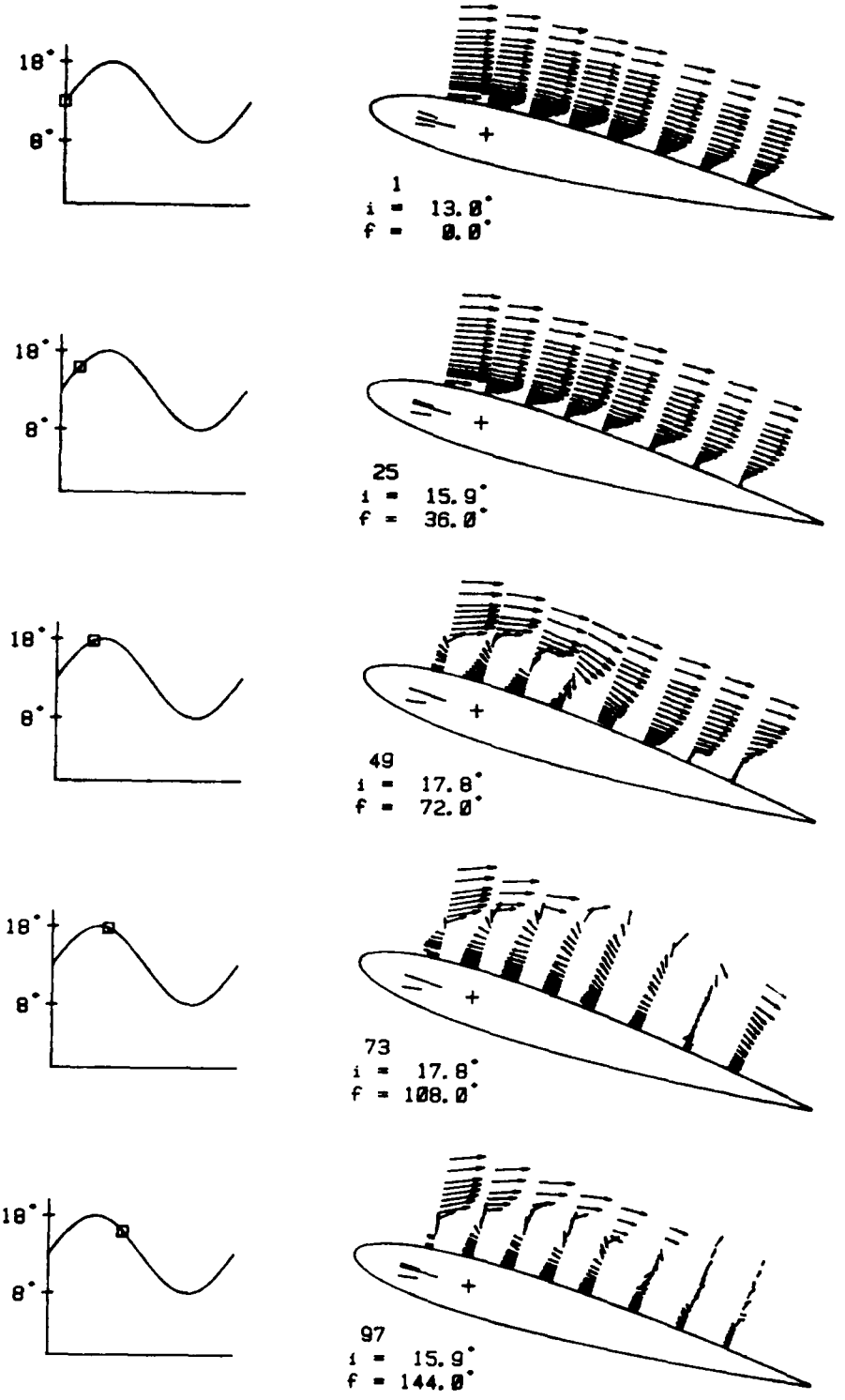

Figure 11.a :

Test case BL18 : 8° to 18° incidence, k = 0. , stall

Velocity vectors scale : — Q

i : incidence f : phase angle

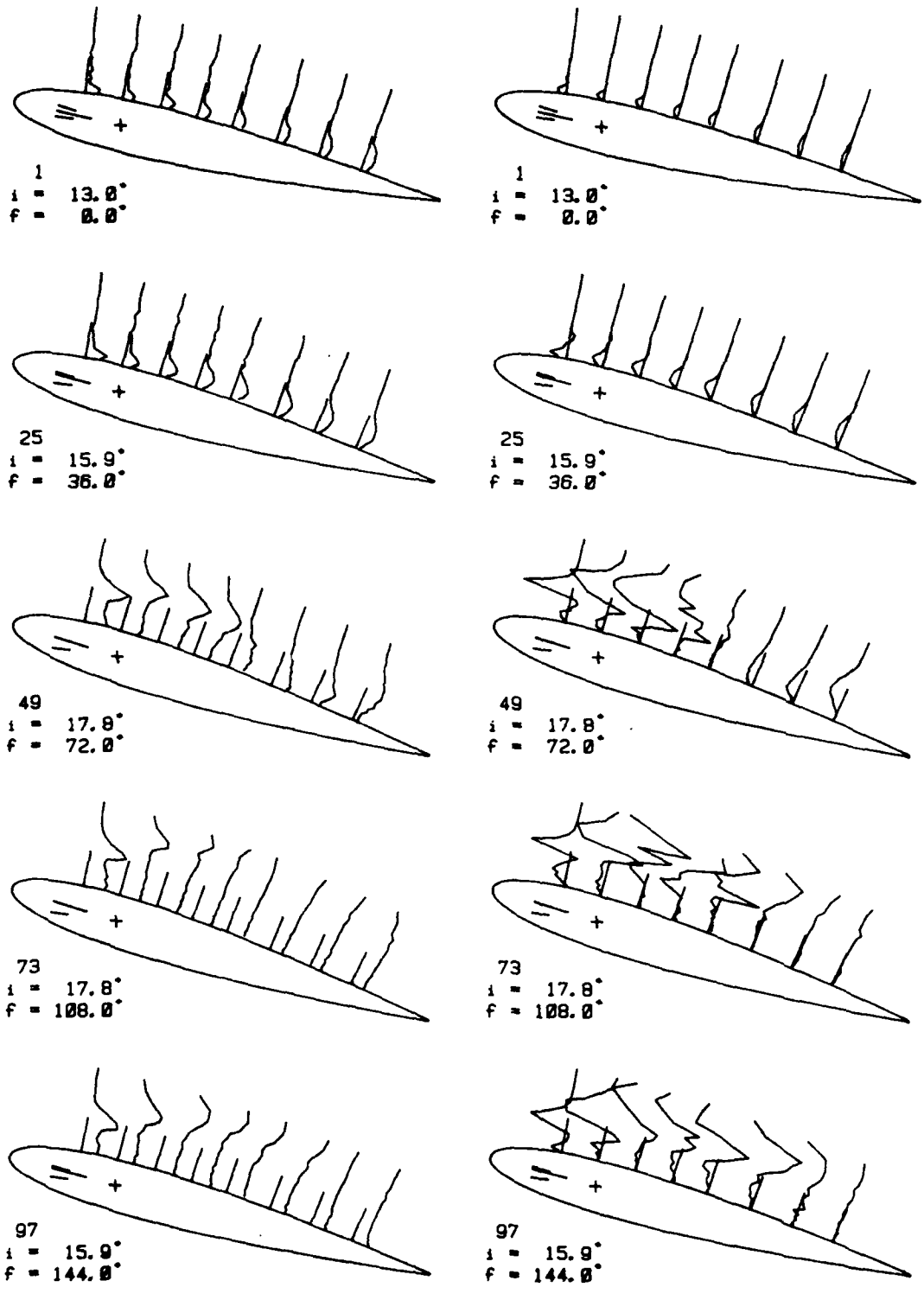

Figure 11.a (continued) :

Test case BL18 : 8° to 18° incidence, k = 0.3, stall

Left : Chordwise fluctuations $\sqrt{u'^2}/Q$ scale : — 30% Q

Right : Reynolds stress $-\overline{u'v'}/Q^2$ scale : — 3% Q^2

i : incidence f : phase angle

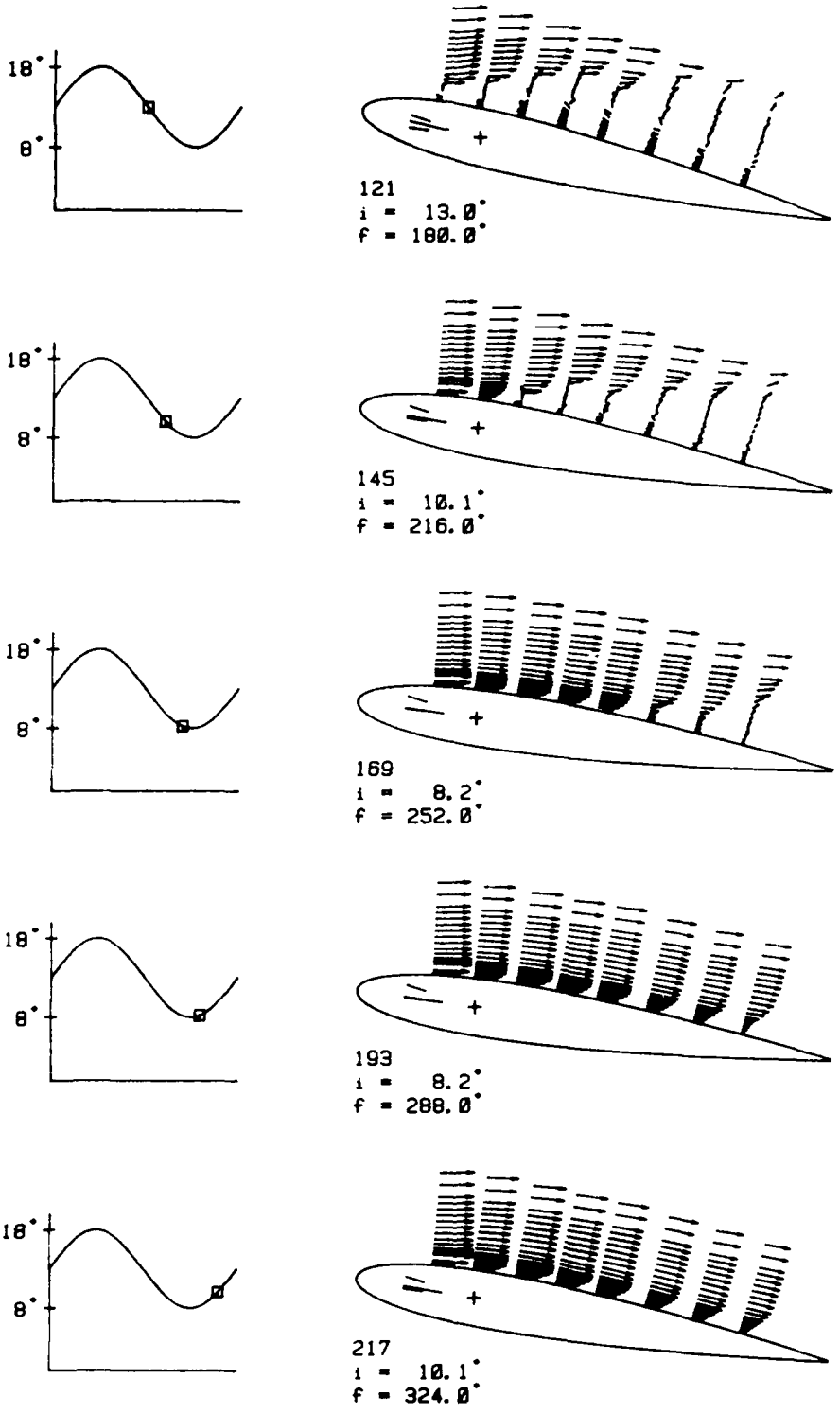

Figure 11.b :

Test case BL18 : 8° to 18° incidence, k = 0.3, stall

Velocity vectors scale : — Q

i : incidence f : phase angle

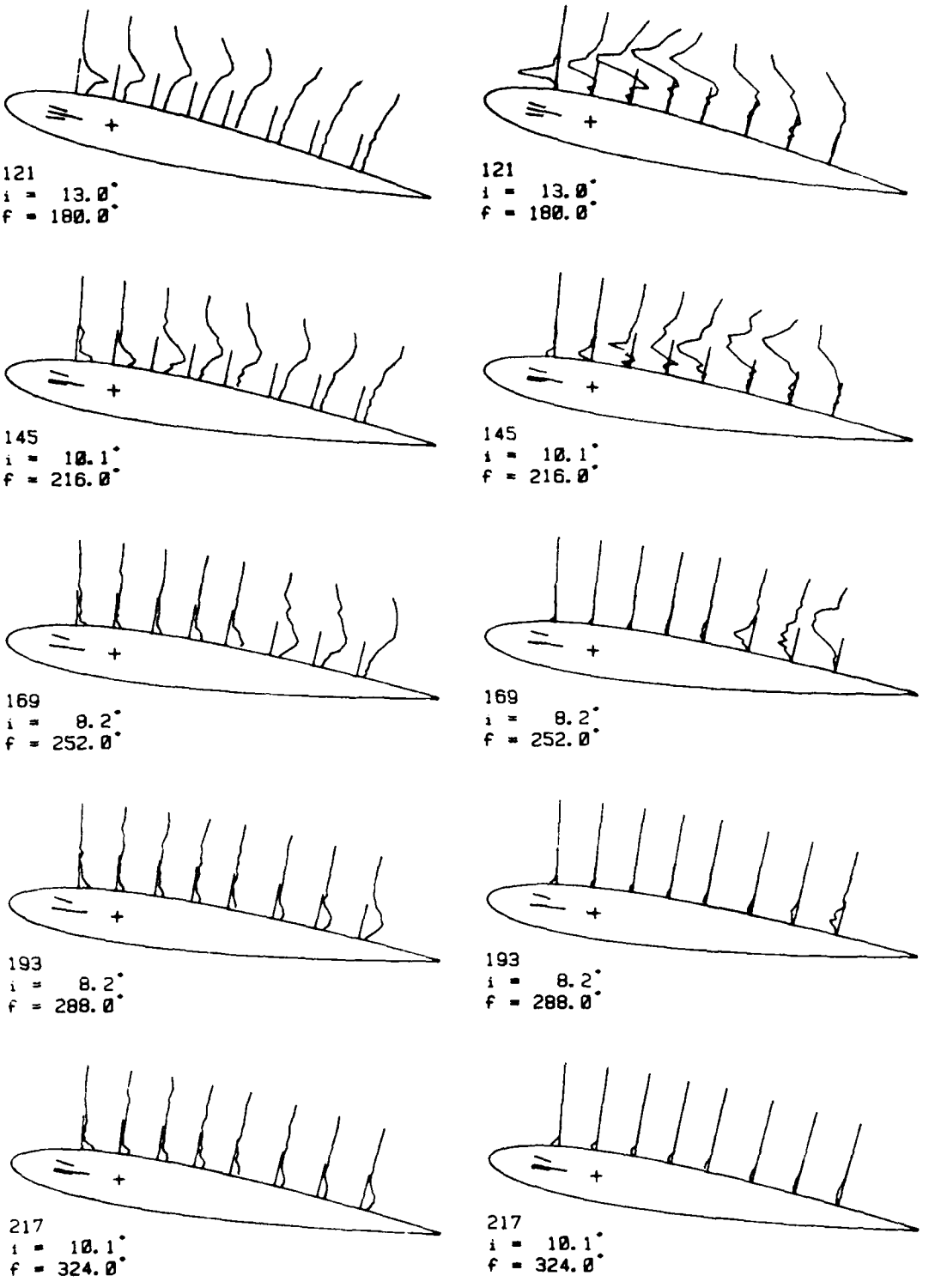

Figure 11.b (continued) :

Test case BL18 : 8° to 18° incidence, k = 0.3, stall

Left : Chordwise fluctuations $\sqrt{u'^2}/Q$ scale : — 30% Q

Right : Reynolds stress $-\overline{u'v'}/Q^2$ scale : — 3% Q^2

i : incidence f : phase angle

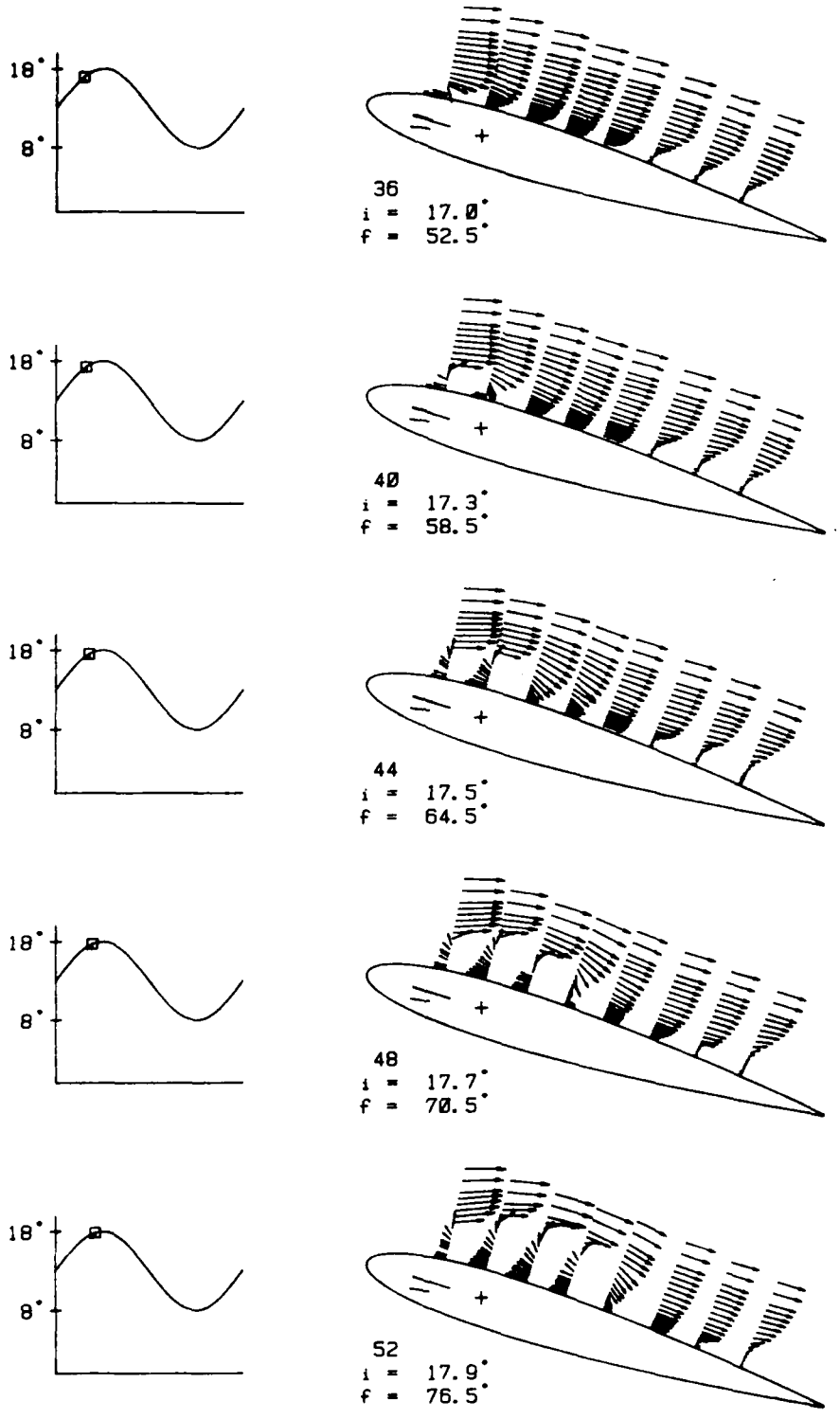

Figure 12 :

Test case BL18 : 8° to 18° incidence, k = 0.3, stall

Velocity vectors scale : — Q

i : incidence f : phase angle

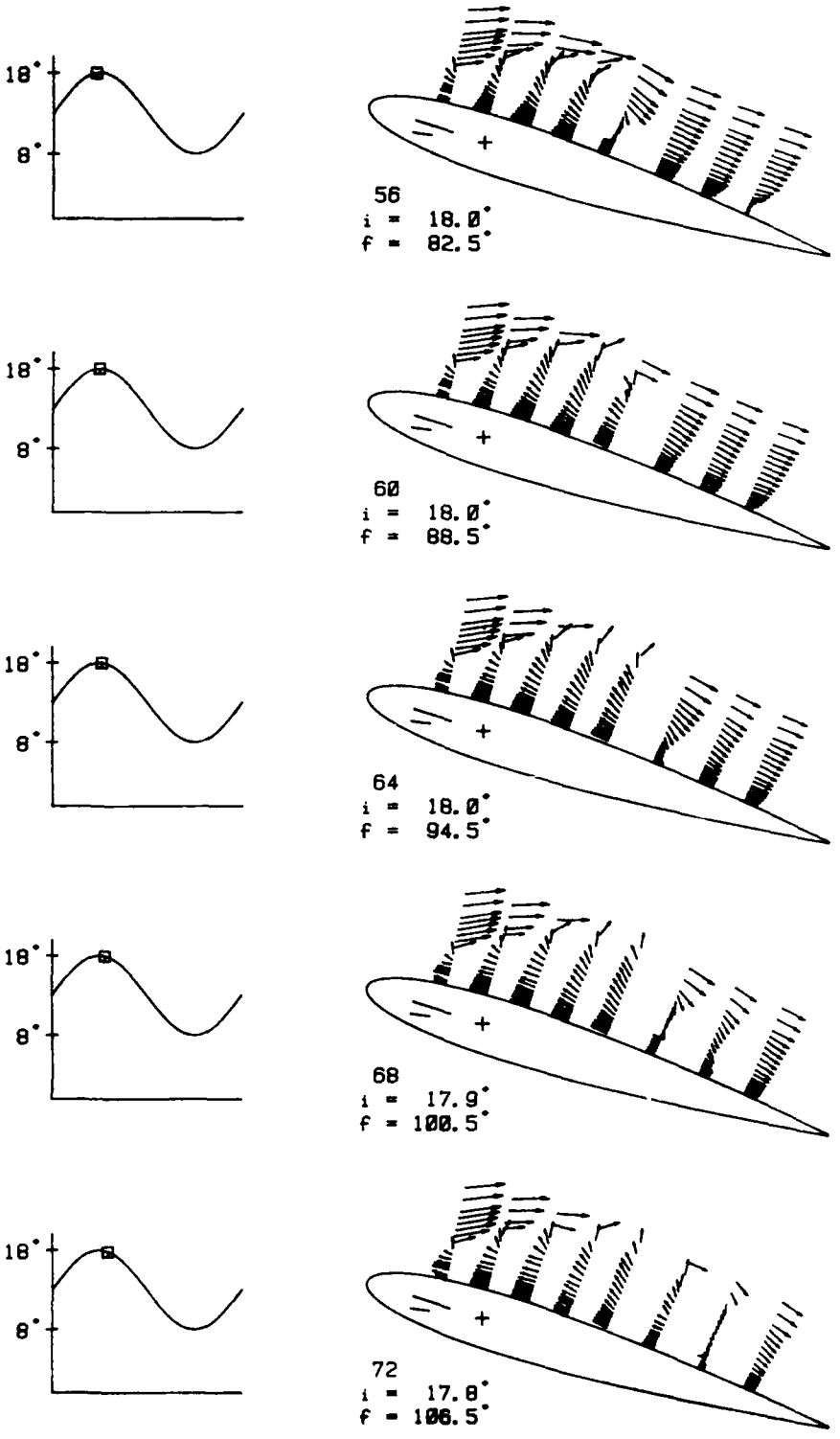

Figure 12 (continued on next page) :

Test case BL18 : 8° to 18° incidence, k = 0.3, stall

Velocity vectors scale : — Q

i : incidence f : phase angle

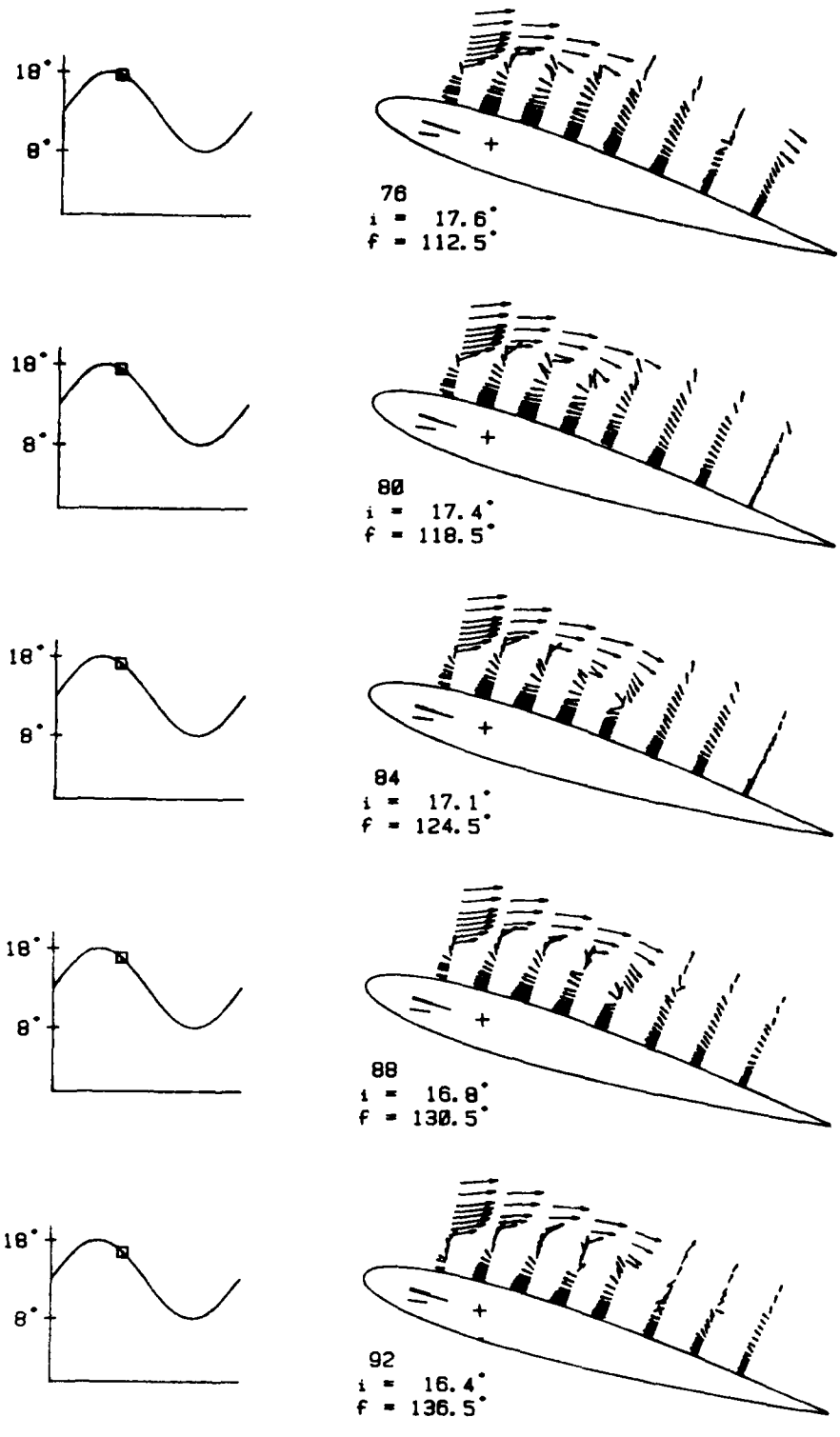

Figure 12 (continued) :

Test case BL18 : 8° to 18° incidence, k = 0.3, stall

Velocity vectors scale : — Q

i : incidence f : phase angle

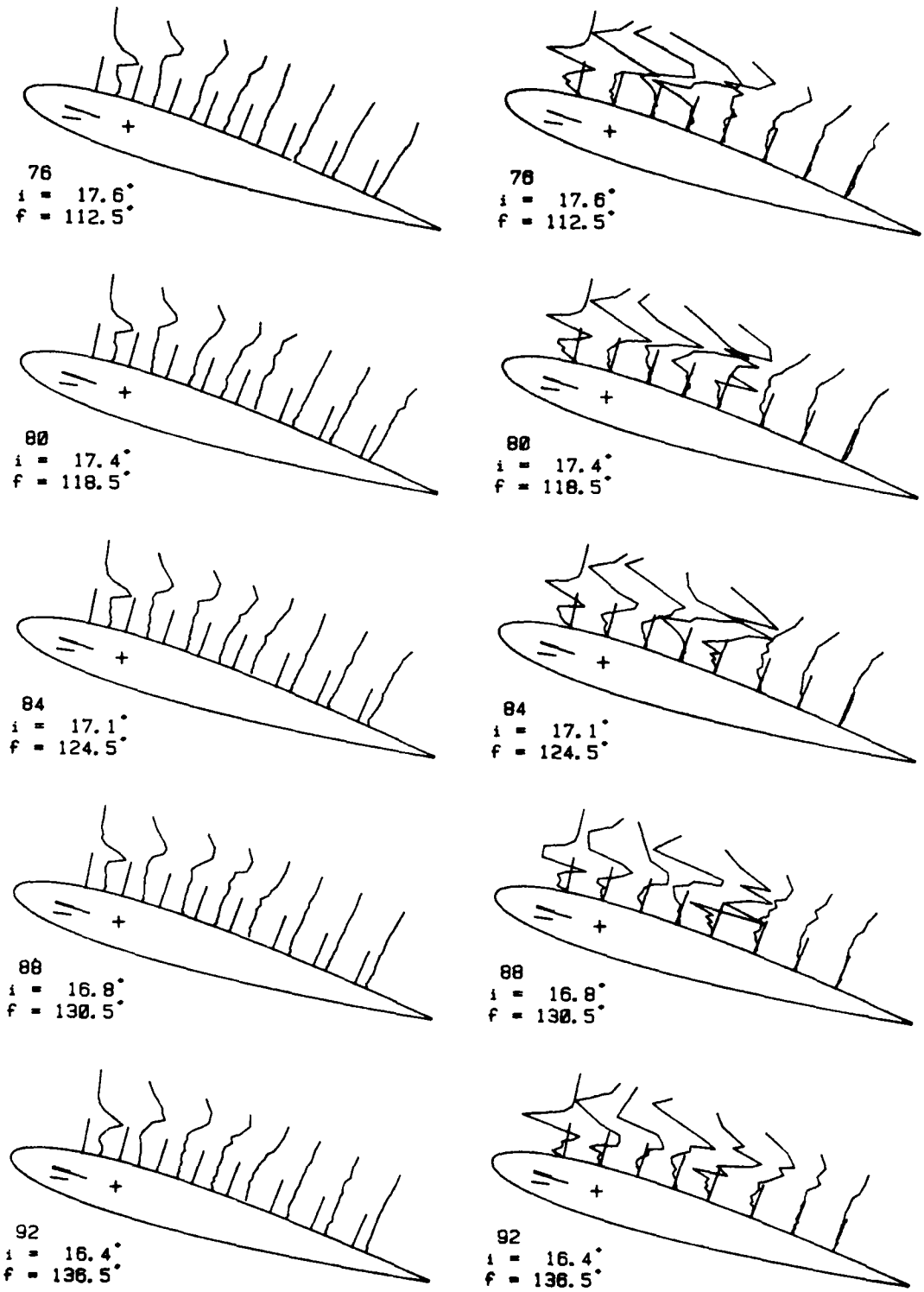

Figure 12 (end) :

Test case BL18 : 8° to 18° incidence, k = 0.3, stall

Velocity vectors scale : — Q

i : incidence f : phase angle

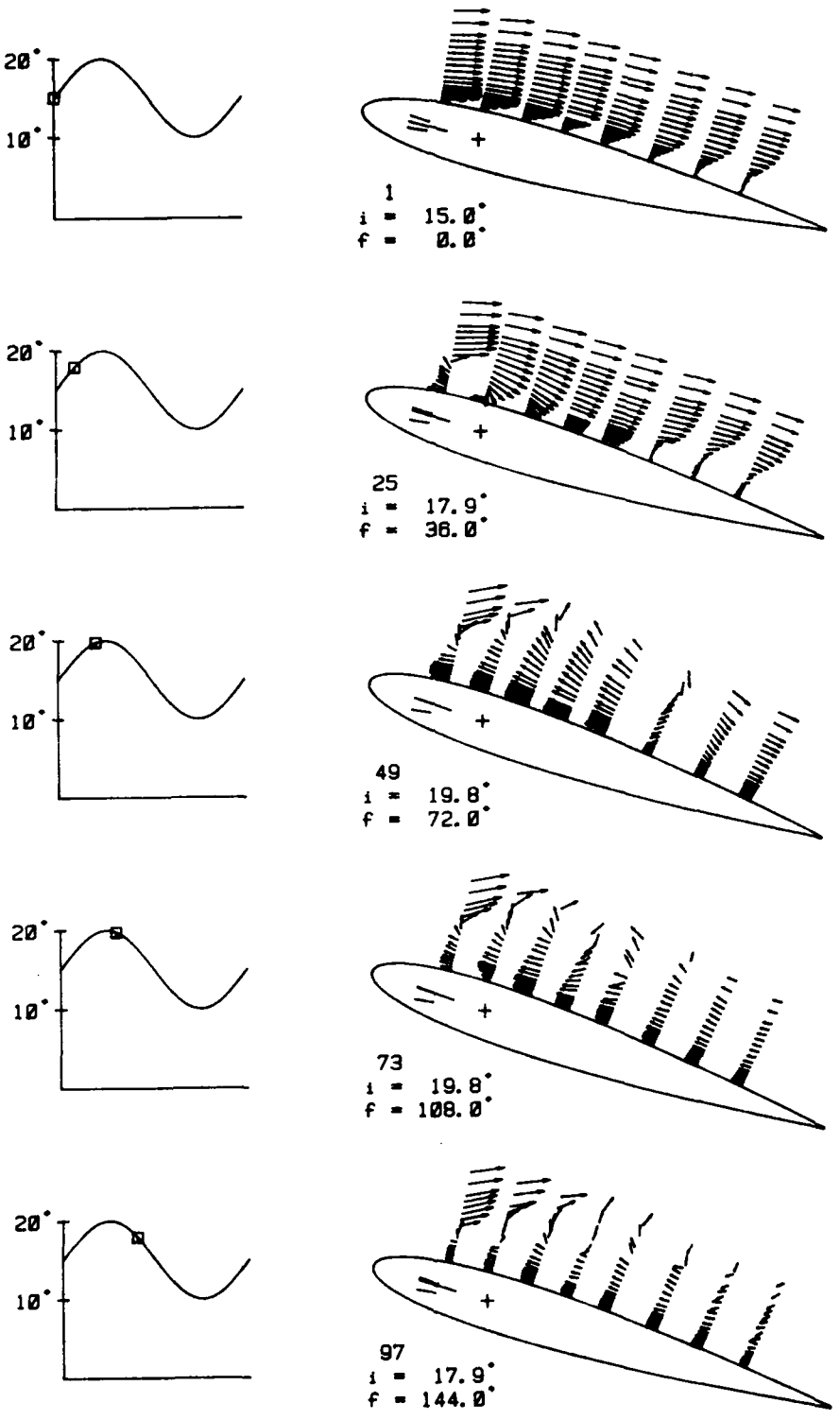

Figure 13.a :

Test case BL20 : 10° to 20° incidence, k = 0.3, stall

Velocity vectors scale : — Q

i : incidence f : phase angle

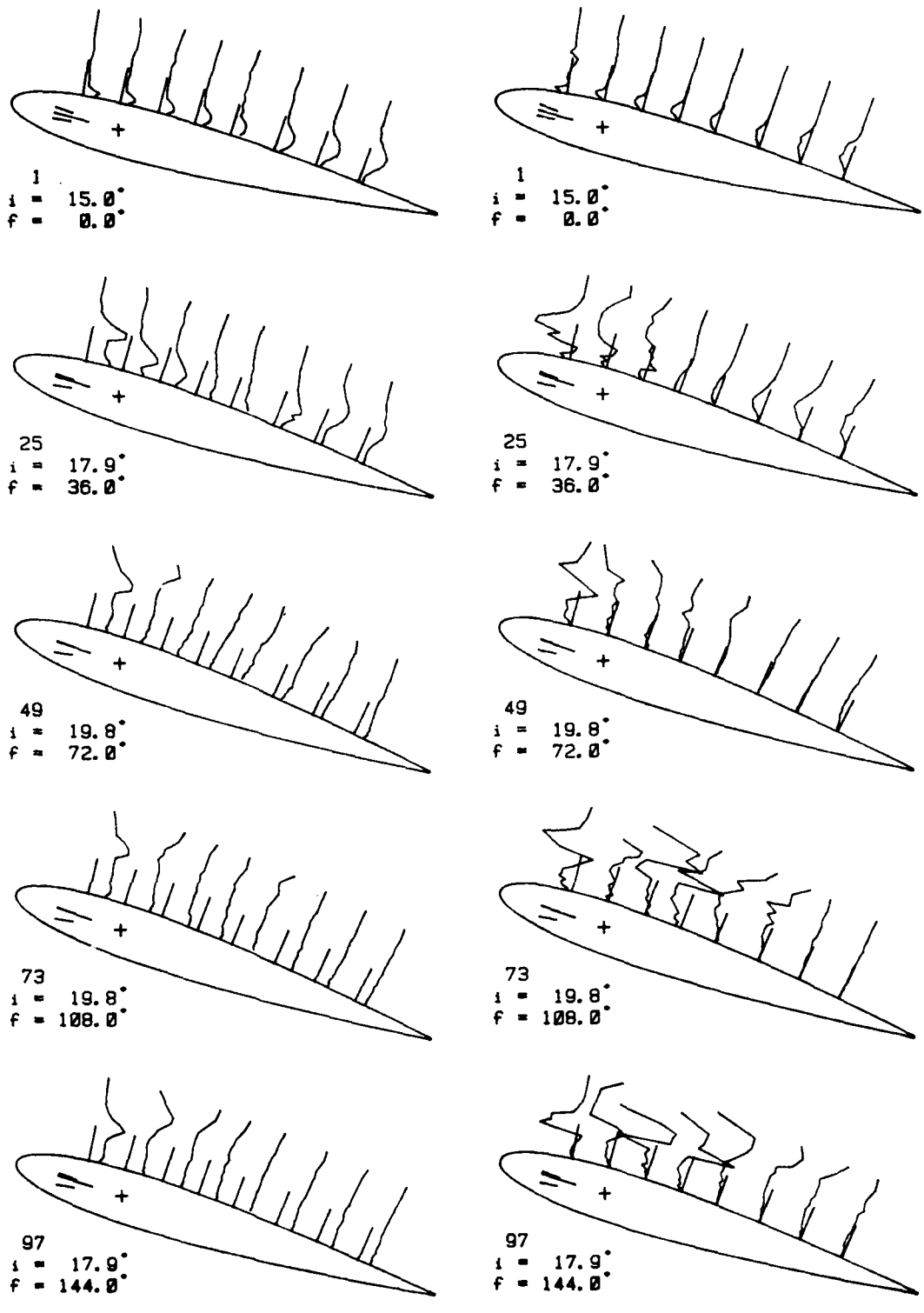

Figure 13.a (continued) :

Test case BL20 : 10° to 20° incidence, k = 0.3, stall

Left : Chordwise fluctuations $\sqrt{u'^2}/Q$ scale : — 30% Q

Right : Reynolds stress $-\overline{u'v'}/Q^2$ scale : — 3% Q^2

i : incidence f : phase angle

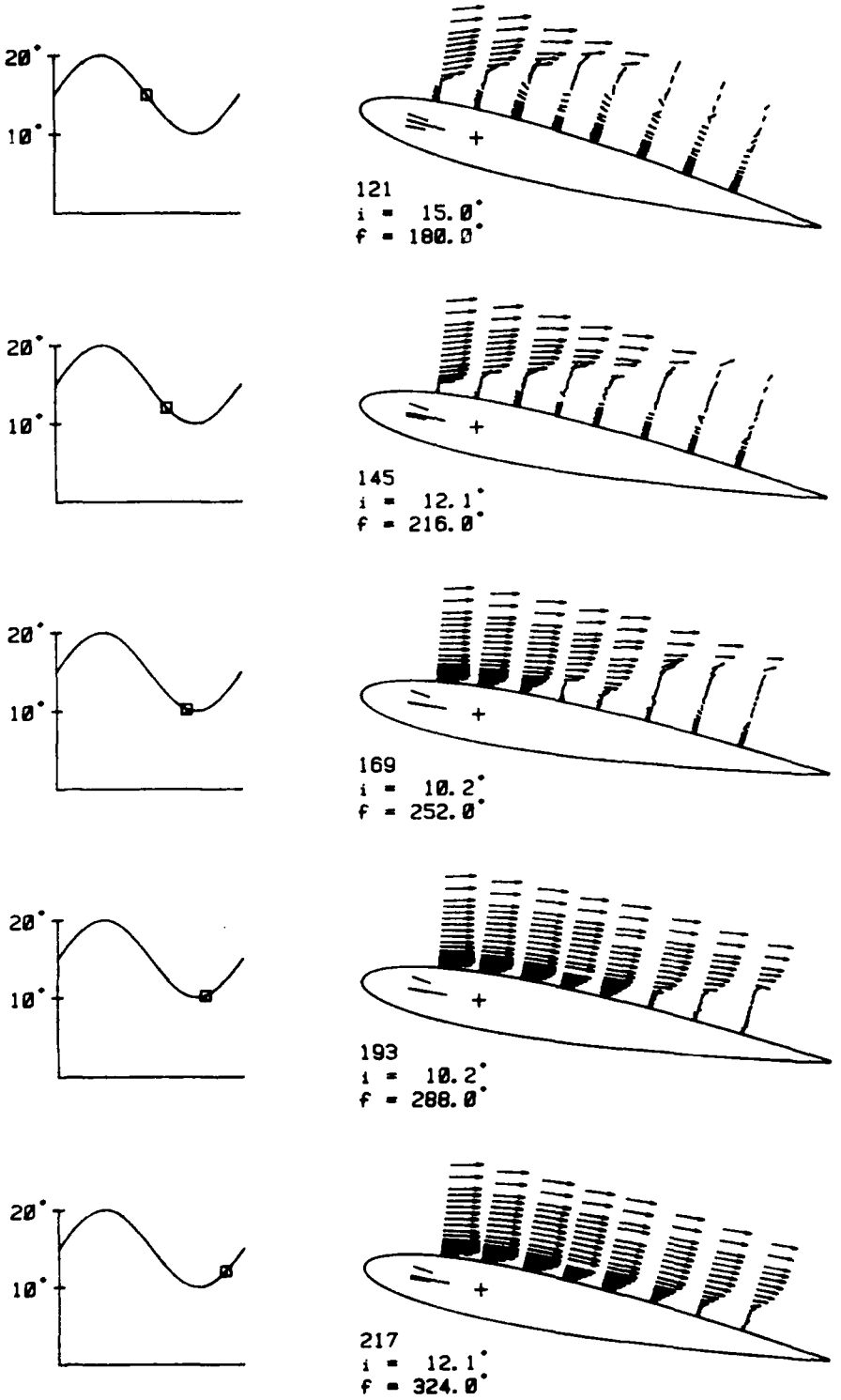

Figure 13.b :

Test case BL20 : 10° to 20° incidence, k = 0.3, stall

Velocity vectors scale : — Q

i : incidence f : phase angle

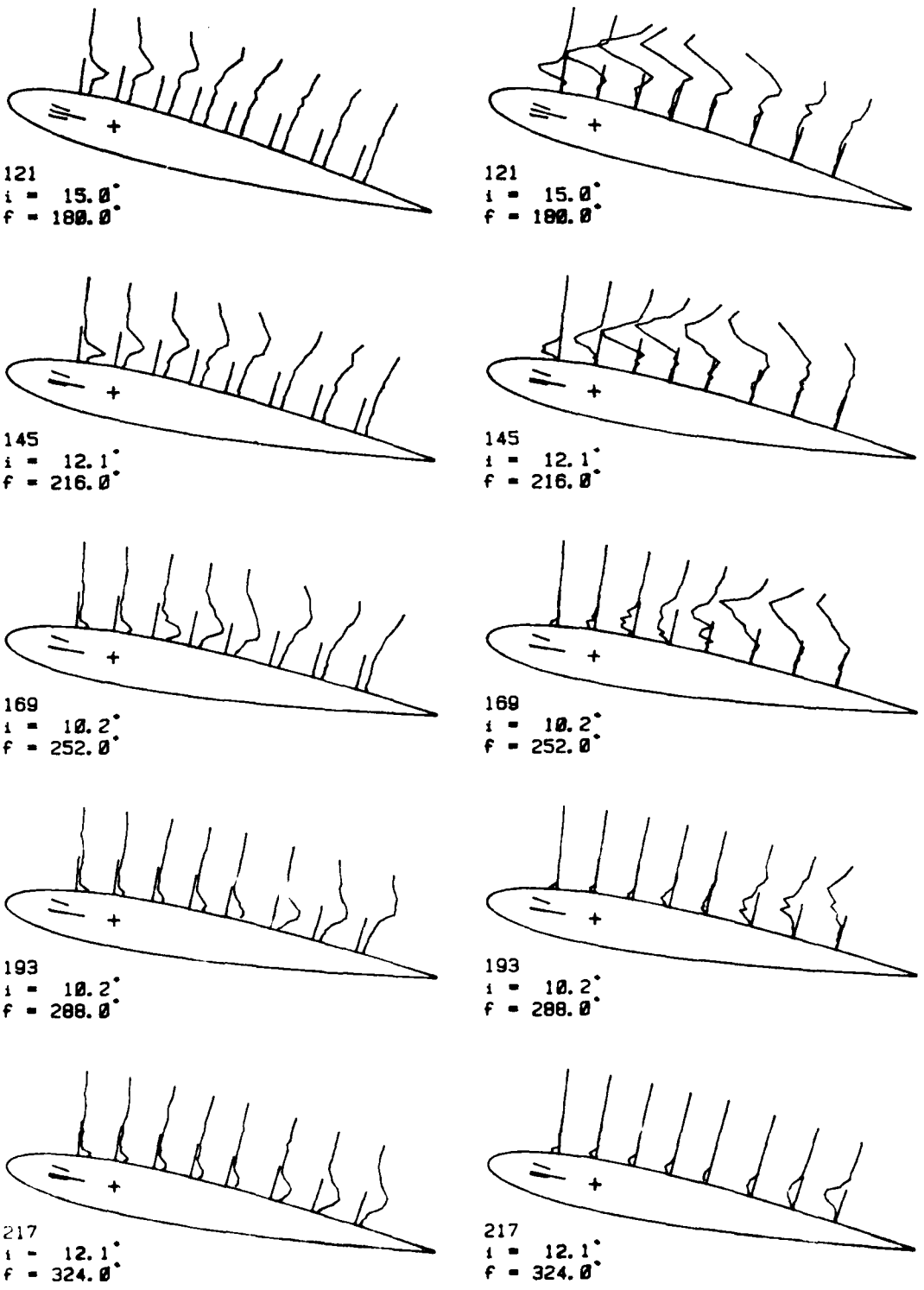

Figure 13.b (continued) :

Test case BL20 : 10° to 20° incidence, k = 0.3, stall

Left : Chordwise fluctuations $\sqrt{u'^2}/Q$ scale : — 30% Q

Right : Reynolds stress $-\overline{u'v'}/Q^2$ scale : — 3% Q^2

i : incidence f : phase angle

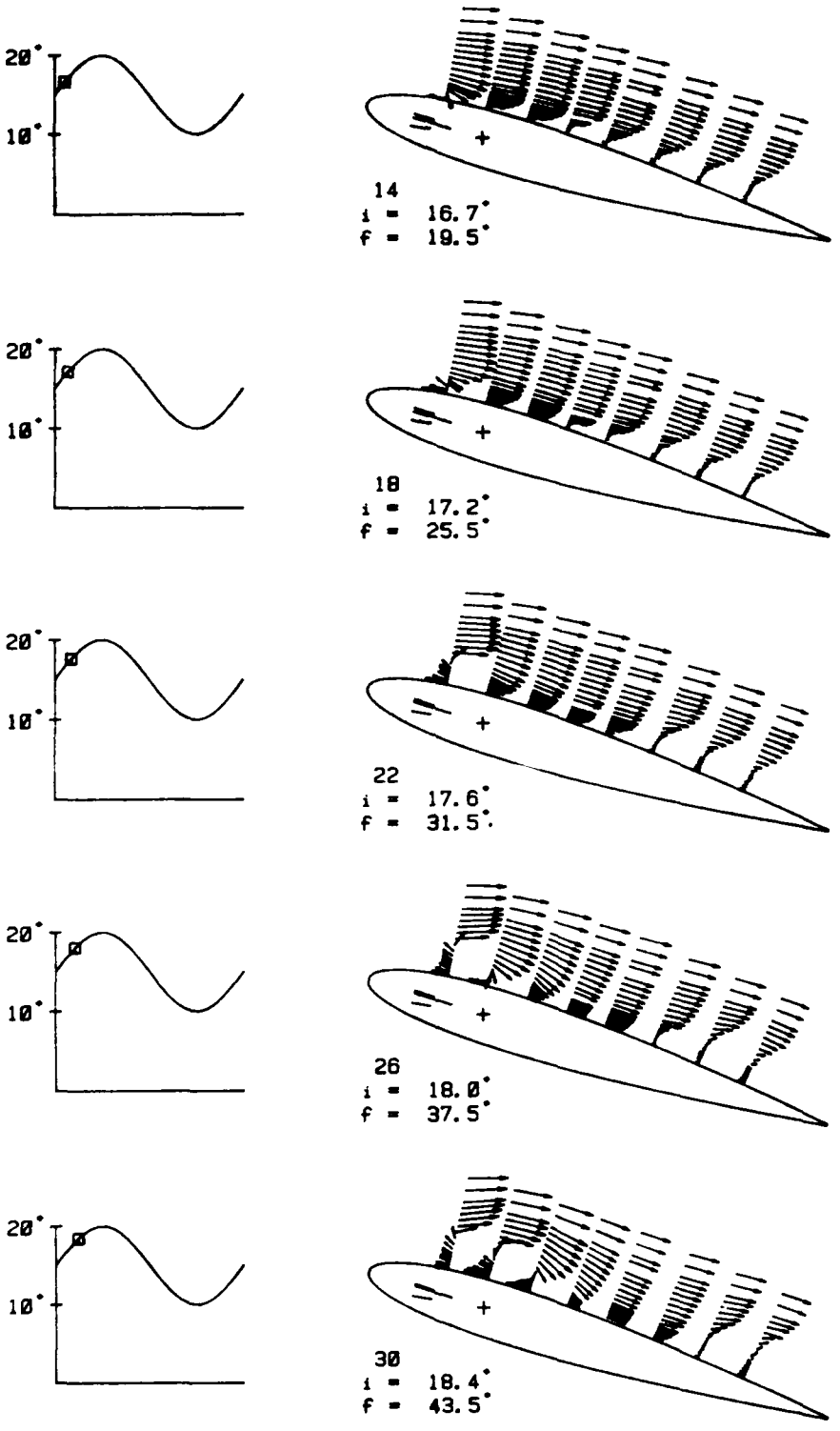

Figure 14 :

Test case BL20 : 10° to 20° incidence, k = 0.3, stall

Velocity vectors scale : — Q

i : incidence f : phase angle

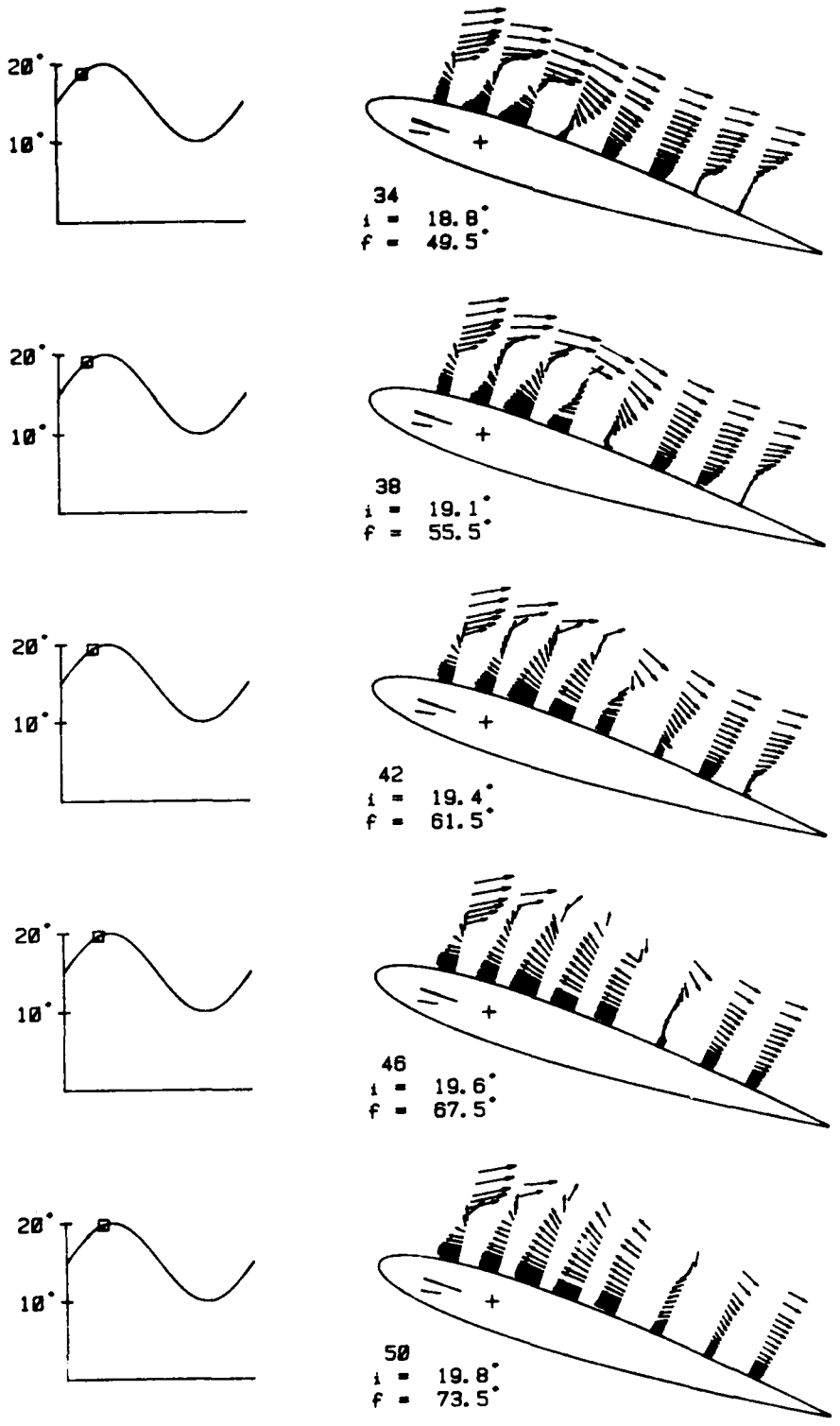

Figure 14 (continued on next page) :

Test case BL20 : 10° to 20° incidence, k = 0.3, stall

Velocity vectors scale : — Q

i : incidence f : phase angle

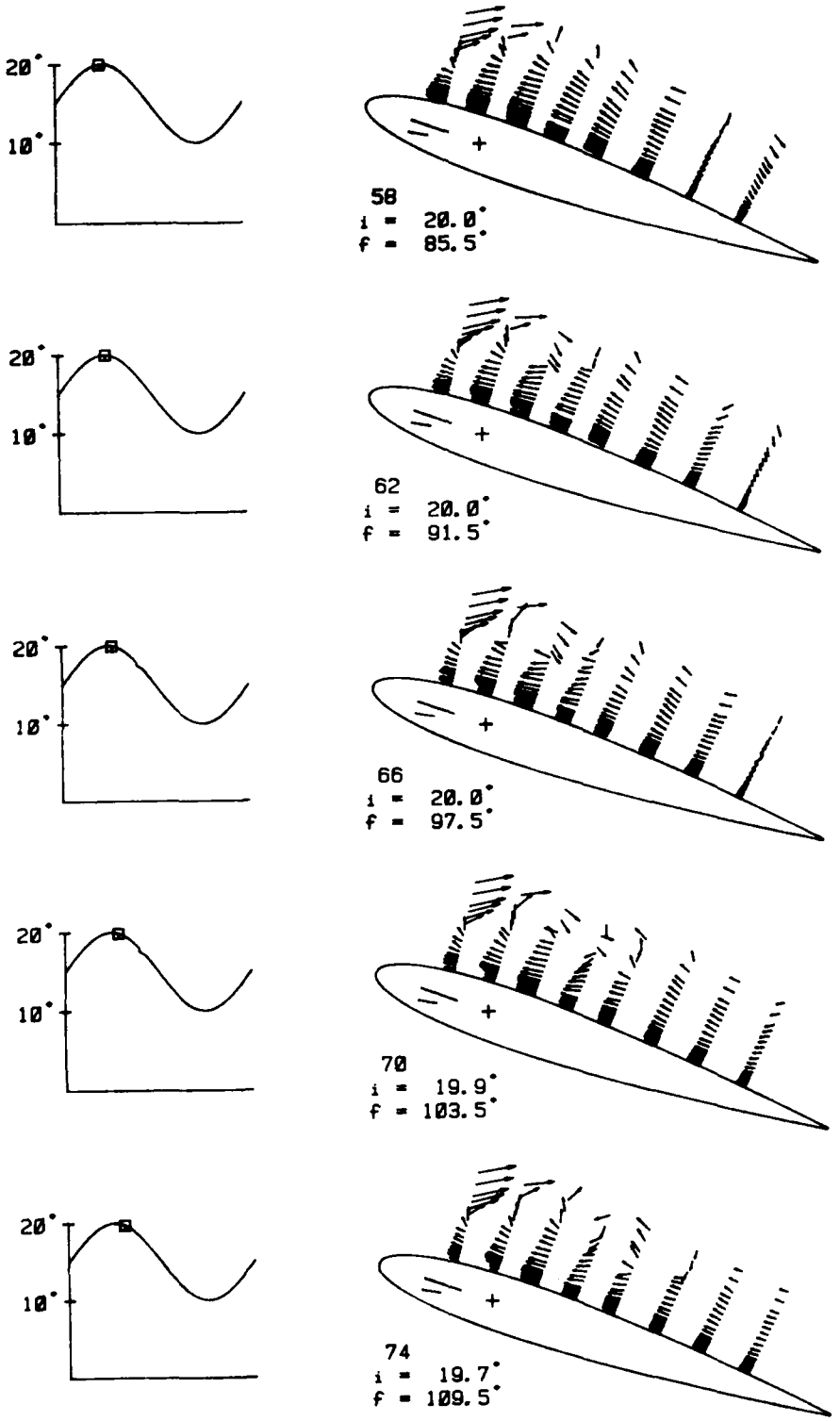

Figure 14 (continued)

Test case BL20 : 10° to 20° incidence, k = 0.3, stall

Velocity vectors scale : — Q

i : incidence f : phase angle

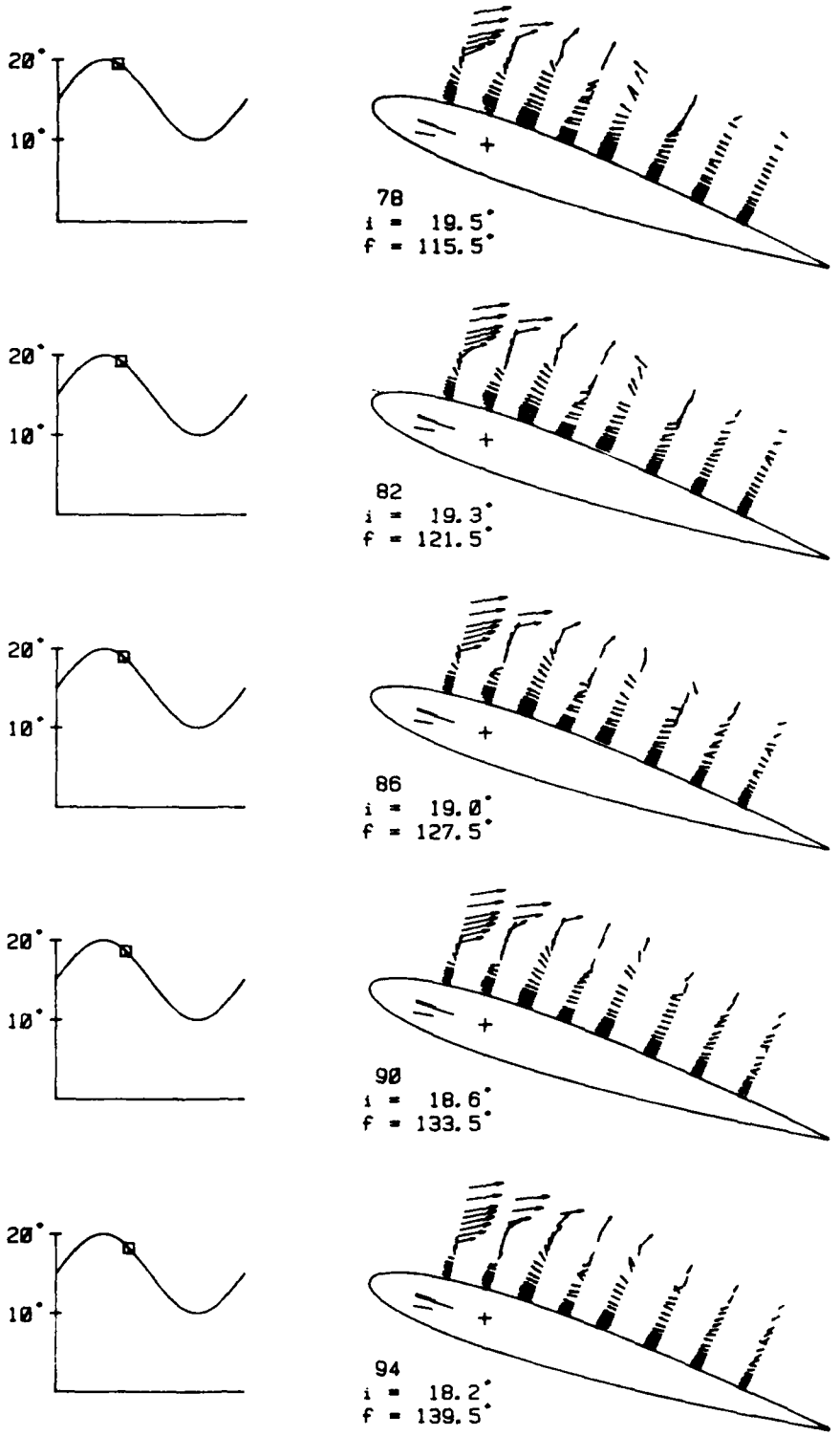

Figure 14 (end)

Test case BL20 : 10° to 20° incidence, k = 0.3, stall

Velocity vectors scale : — Q

i : incidence f : phase angle

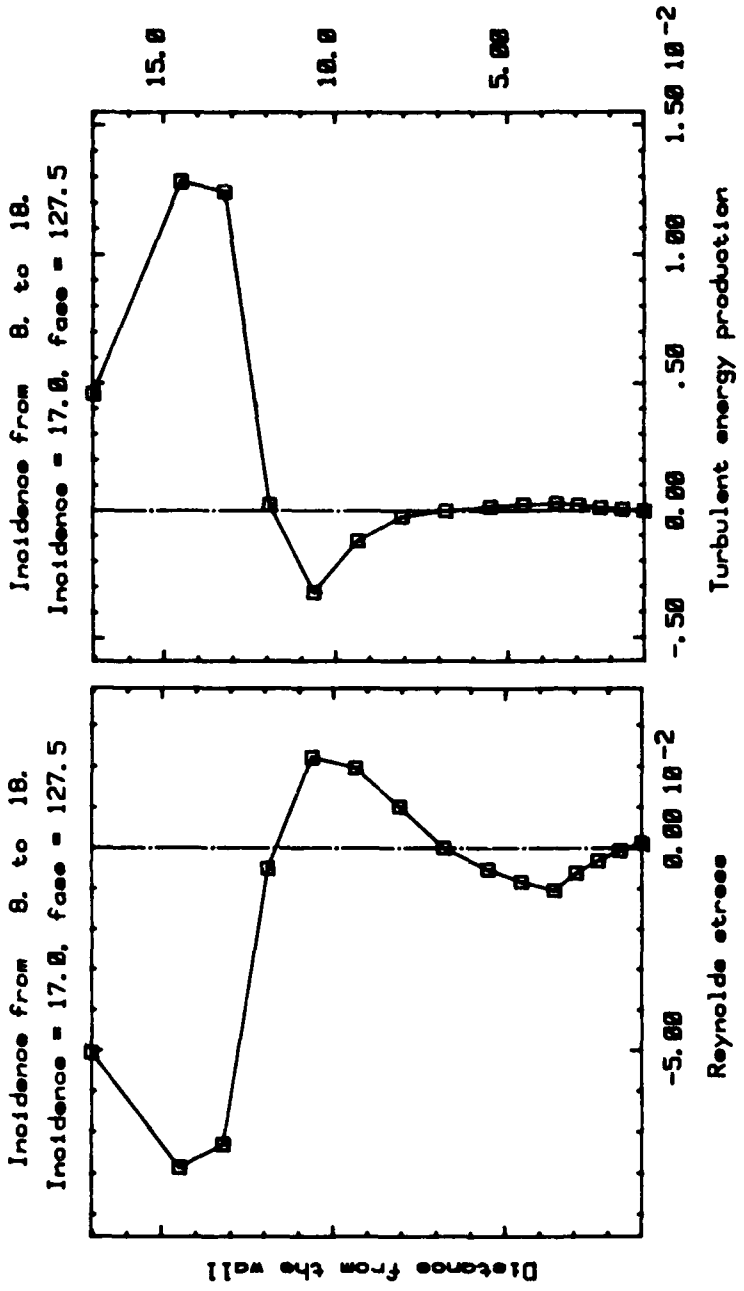

Figure 15 : Turbulent energy production profiles
Test case BL18, 17° incidence, fase = 127.5°
Station 3

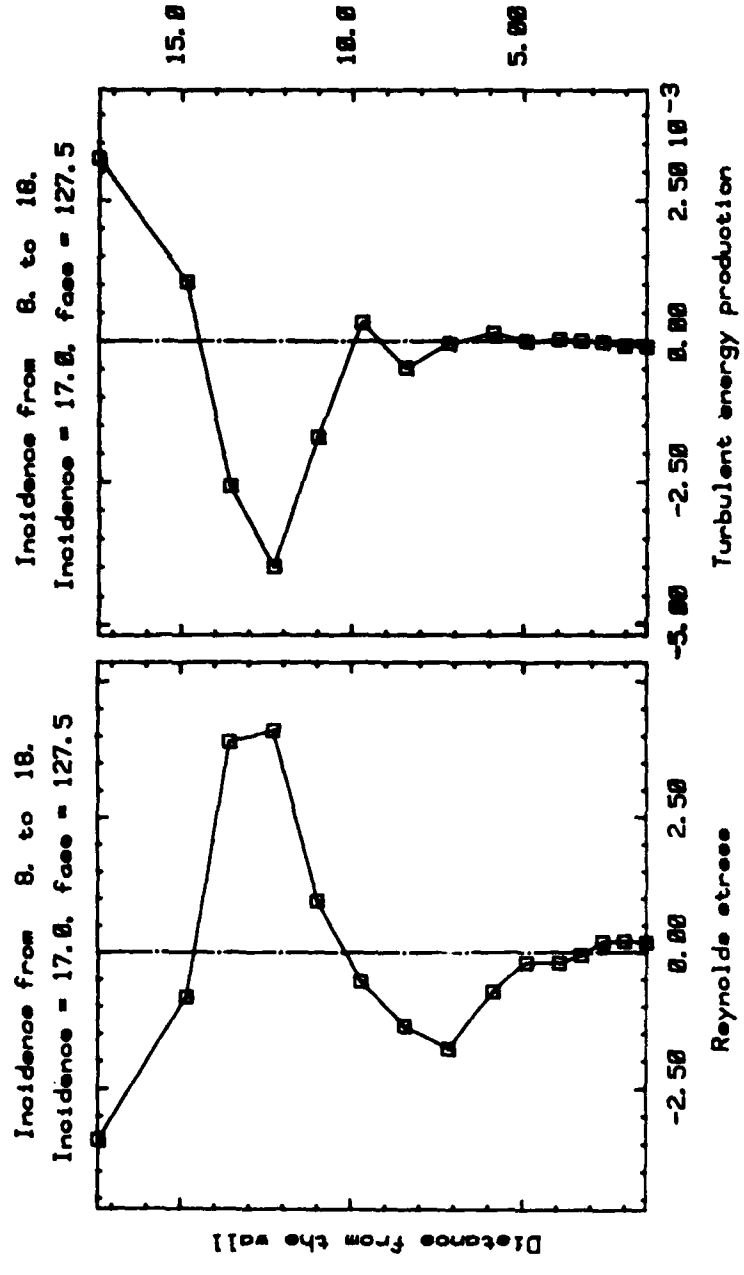

Figure 15 (continued) Velocity and corresponding stress profiles
Test case BL18, 17° incidence, fase = 127.5°
Station 4

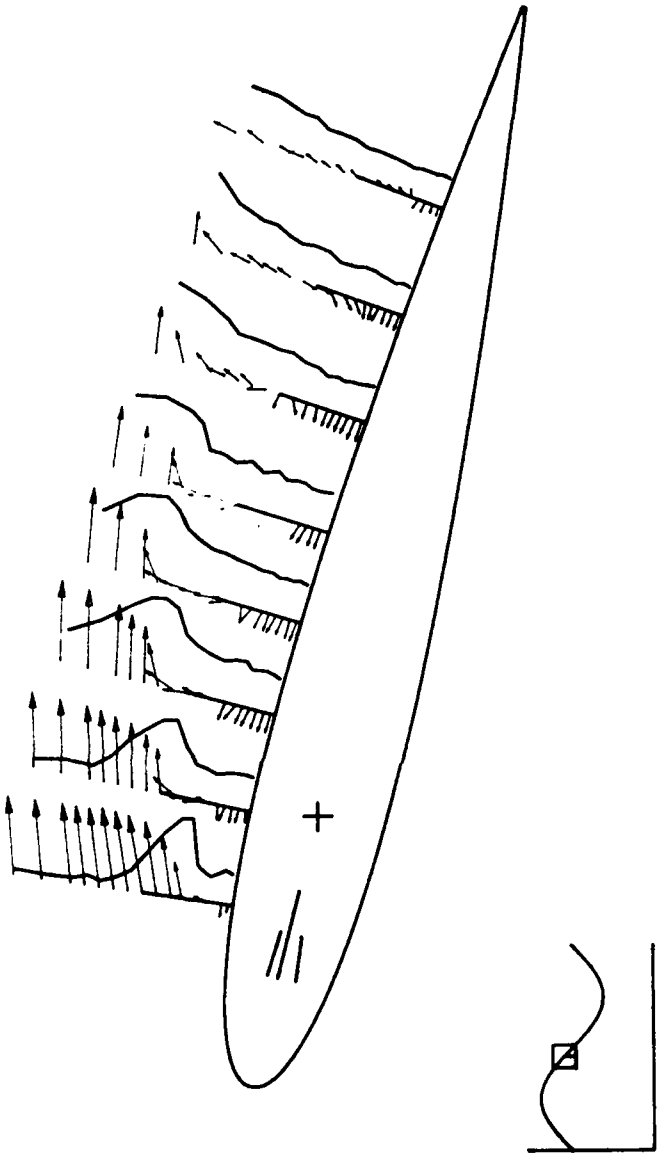

Figure 16 : Velocity and corresponding $\sqrt{u'^2}$ profiles
Test case BL18, time step 104, fase = 142.5°

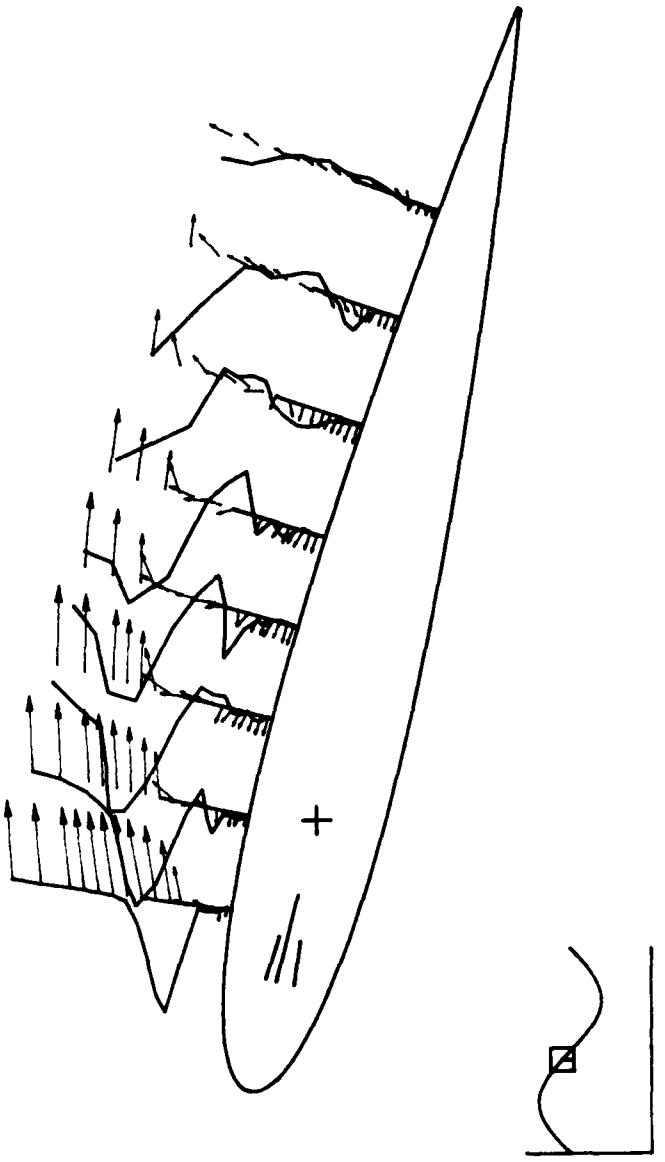

Figure 16 (continued) : Velocity and corresponding Reynolds stress profiles
Test case BL18, time step 104, fase = 142.5°

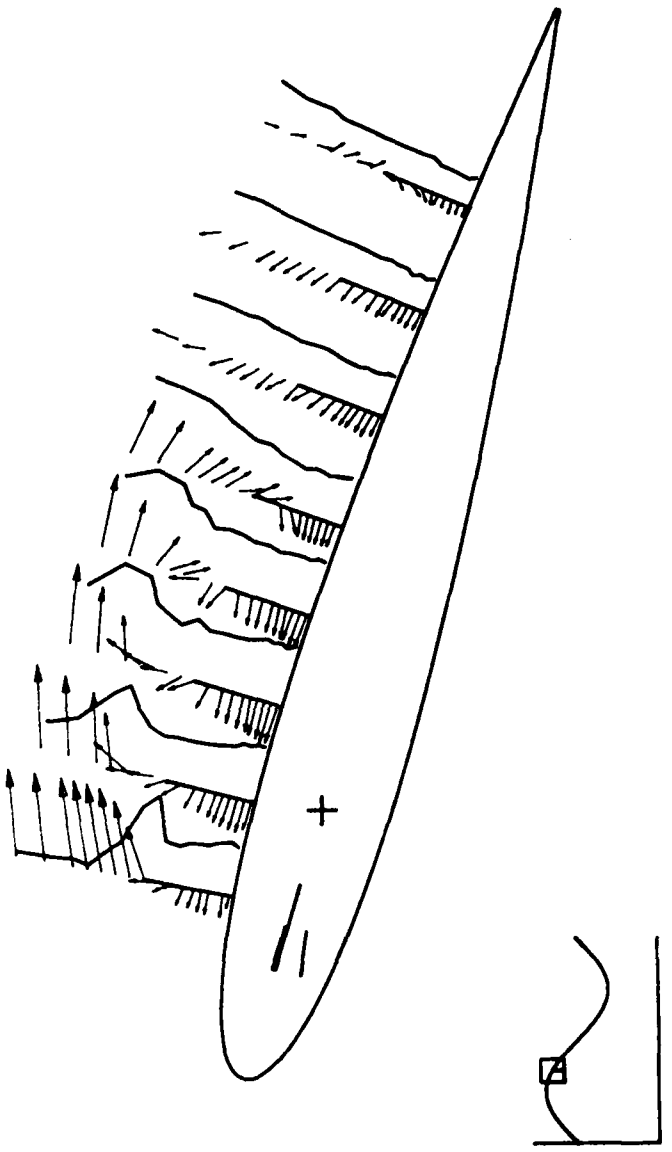

Figure 17 : Velocity and corresponding $\sqrt{u'^2}$ profiles
Test case BL18, time step 95, fase = 127.5°

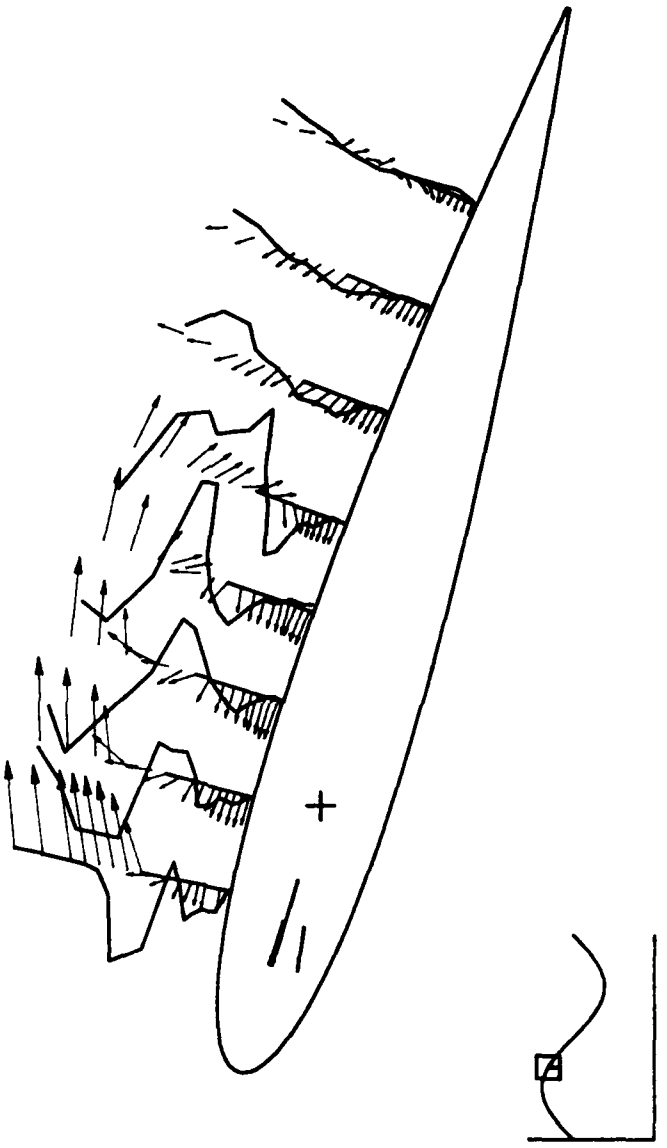

Figure 17 (continued) : Velocity and corresponding Reynolds stress profiles
Test case BL18, time step 94, fase = 127.5°

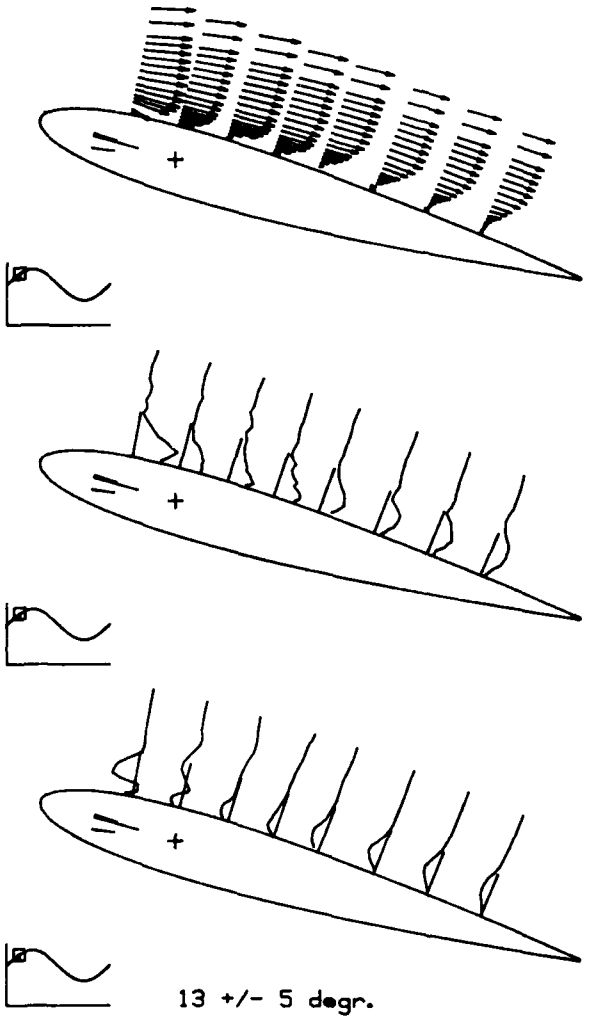

Figure 18 : Velocity and corresponding turbulence profiles
at leading edge separation time
Test case BL18

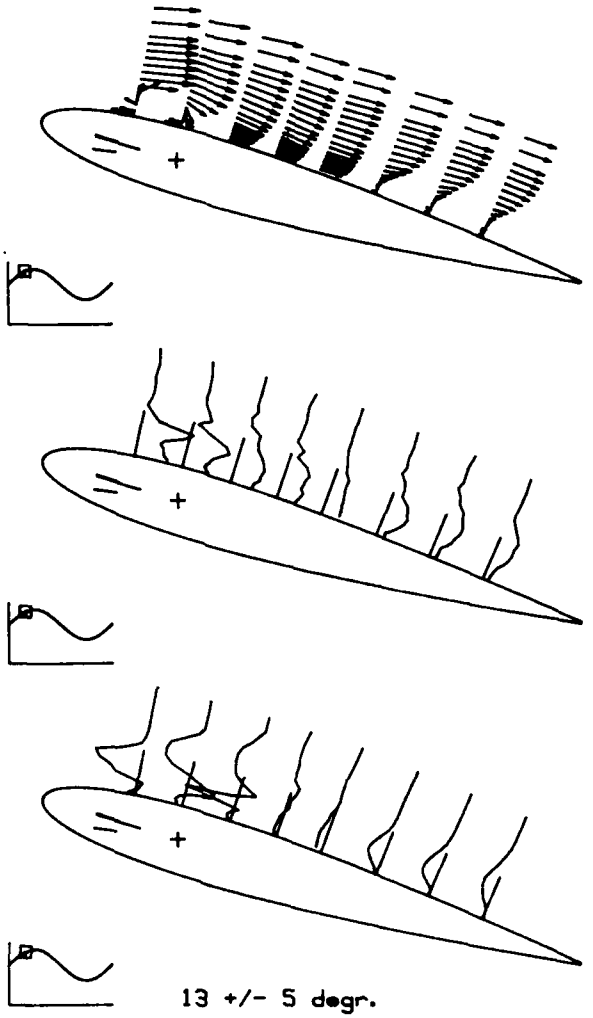

Figure 18 (continued) : Velocity and corresponding turbulence profiles
at leading edge separation time
Test case BL18

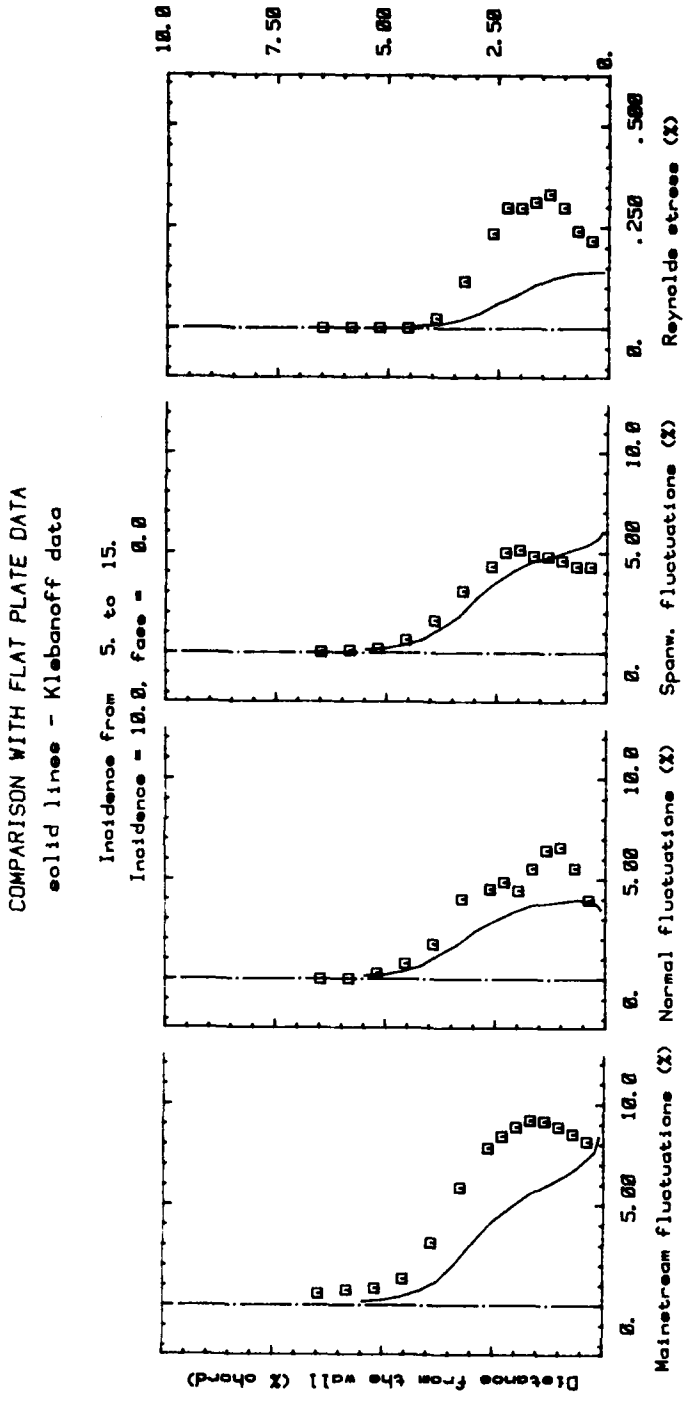

Figure 19.a : Comparison with stant pressure flat plate turbulent boundary layer data
Solid lines : flat plate data [39]
Squares : present data

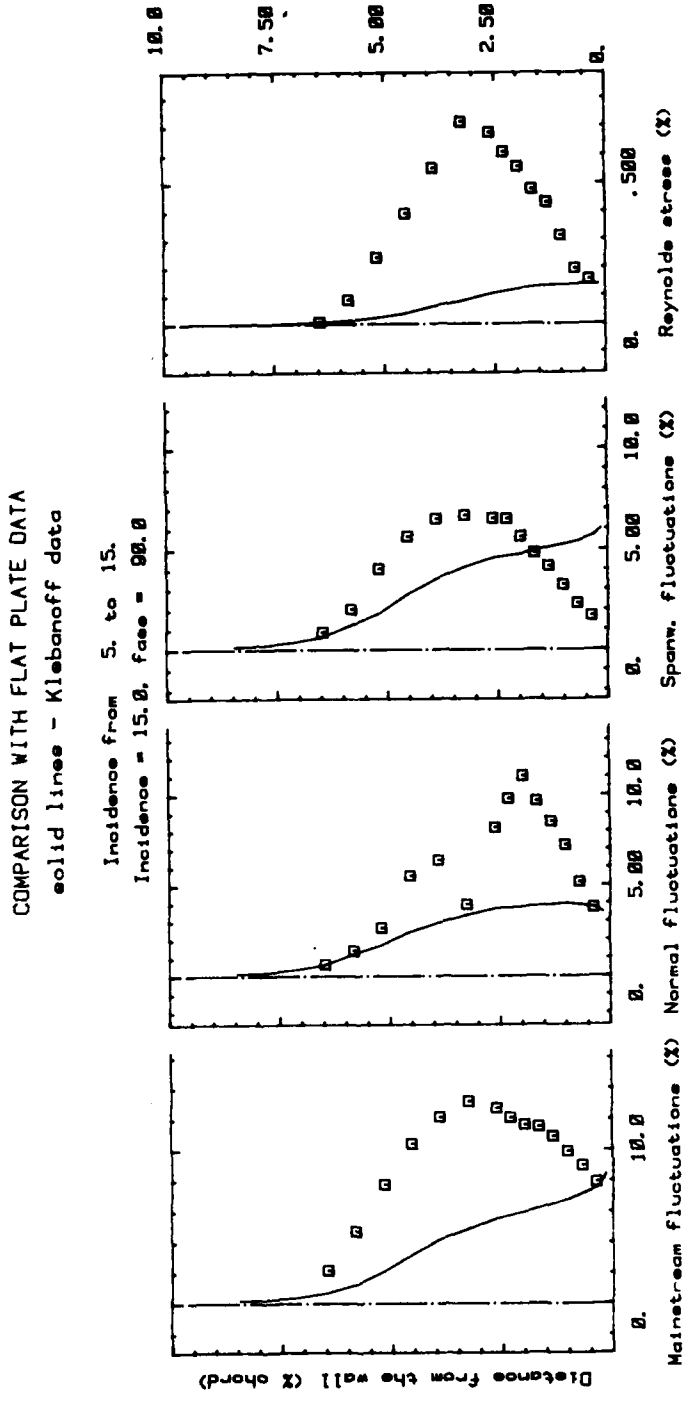

Figure 19.b : Comparison with constant pressure flat plate turbulent boundary layer data
Solid lines : flat plate data [39]
Squares : present data

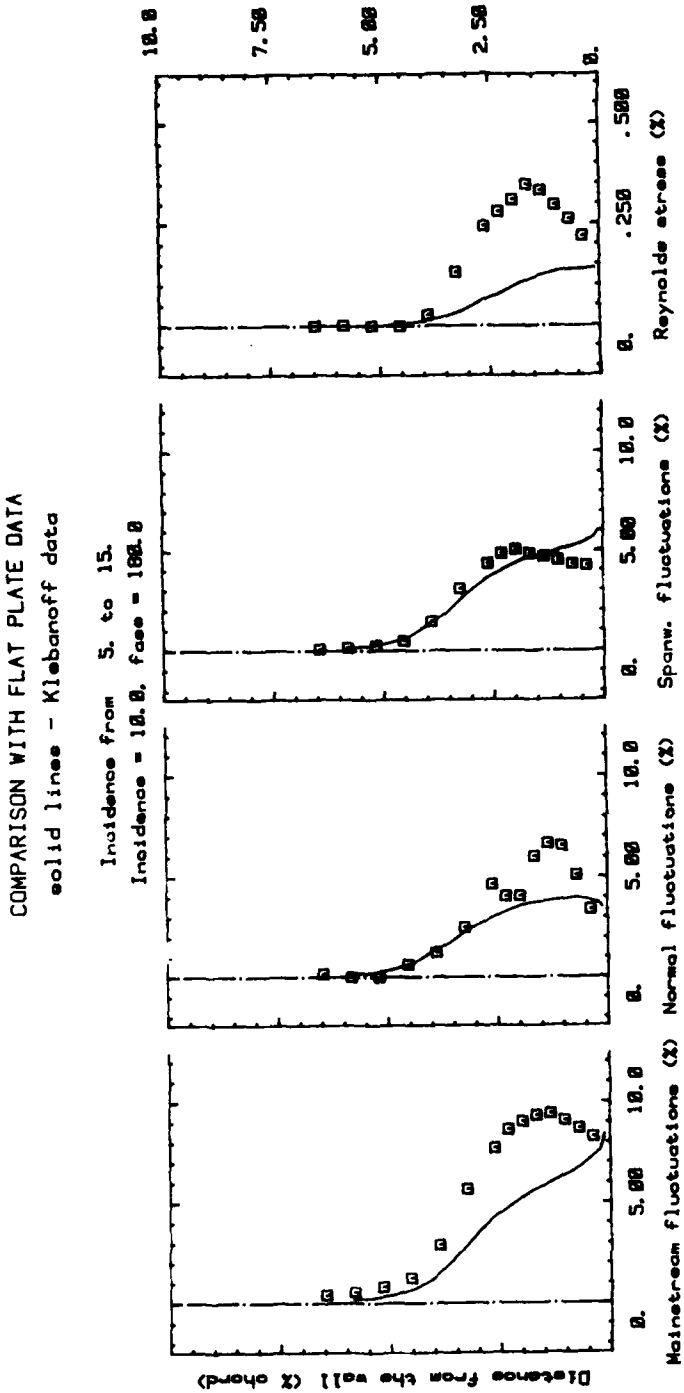

Figure 19.c : Comparison with constant pressure flat plate turbulent boundary layer data
Solid lines : flat plate data [39]
Squares : present data

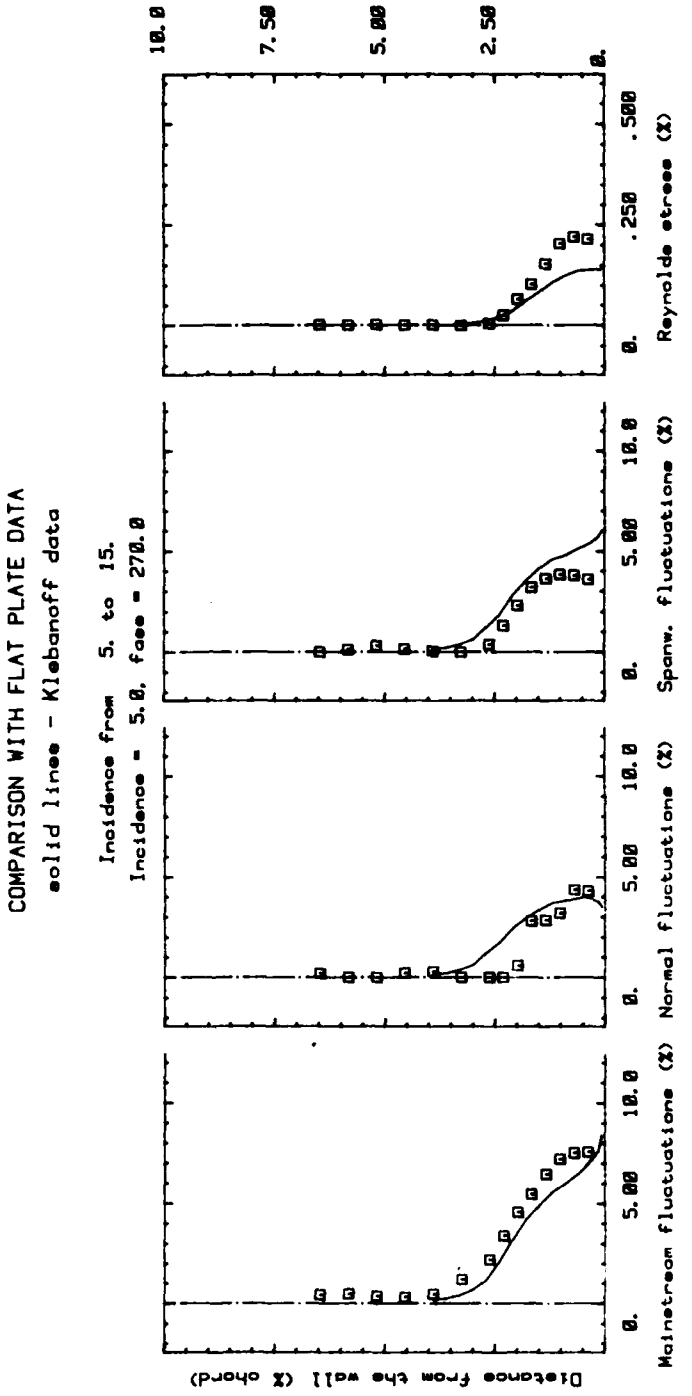

Figure 19.d : Comparison with constant pressure flat plate turbulent boundary layer data
Solid lines : flat plate data [39]
Squares : present data

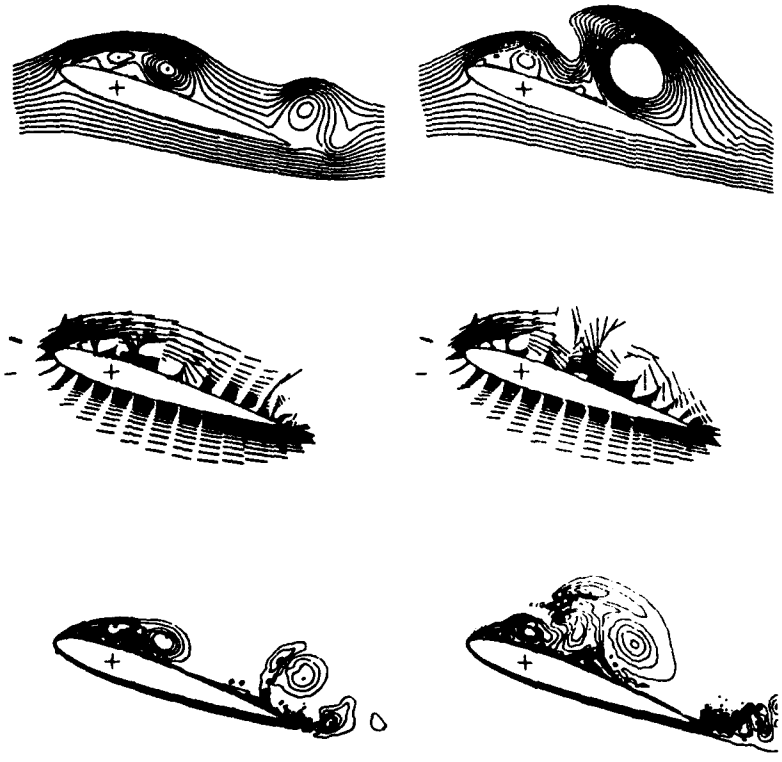

i = 18.97°

i = 19.44°

Figure 20 : Computed results obtained by Mehta (ref 1)

Re = 10,000
k = 0.25

References

[1] MEHTA U.B., 1978, "Dynamic Stall of an Oscillating Airfoil" Agard cp 227, Unsteady Aerodynamics, p 23-1,1978

[2] SUGAVÀNAM A., WU J.C., 1980, "Numerical Study of Separated Turbulent Flow Over Airfoils" AIAA Paper 80-1441, 1980

[3] SANKAR N.L., TASSA Y., 1980, "Reynolds Number and Compressibility Effects on Dynamic Stall of a Naca 0012 Airfoil" AIAA Paper 80-0010,1980

[4] DE RUYCK J., HIRSCH C., "Turbulence Structure in the Wake of an Oscillating Airfoil" Report Vub-Str-12, Vrije Universiteit Brussel, Dept of Fluid Mech., 1981

[5] DE RUYCK J., HIRSCH C., "Instantaneous Turbulence Profiles in the Wake of an Oscillating Airfoil" AIAA Paper 82-0353, 1982

[6] MC CROSKEY W.J., "Some Current Research in Unsteady Fluid Dynamics" Trans. ASME, Journal of Fluid Engineering Vol99, p8-39, 1977

[7] CARR L.W., "A Compilation of Unsteady Turbulent Boundary Layer Data" Agardograph Ag265, 1981

[8] TELIONIS D., 1981, "Unsteady Viscous Flows" Springer Verlag in Computational Physics, 1981

[9] COUSTEIX J., DESOPPER A., HOUDEVILLE R., "Recherches Sur Les Couches Limites Turbulentes Instationaires" Onera/derat tp 1976-147, Toulouse France, 1976

[10] COUSTEIX J., DESOPPER A., HOUDEVILLE R., "Investigation of the Structure and of the Development of a Turbulent Boundary Layer in an Oscillating External Flow" Onera tp N1977-14, Toulouse, France, 1977

[11] COUSTEIX J., HOUDEVILLE R., JAVELLE J., "Experiments on an Oscillating Turbulent Boundary Layer with and Without Pressure Gradient" Unsteady Turbulent Shear Flows Springer Verlag, 1981 (in Press)

[12] COUSTEIX J., HOUDEVILLE R., RAYNAUD M., "Oscillating Turbulent Boundary Layer With Strong Mean Pressure Gradient" Onera tp 1979-89 Toulouse, France, 1979

[13] KENISON R.G., "An Experimental Study of the Effect of Oscillatory Flow on the Separation Region in a Turbulent Boundary Layer" Agard C.p. 227, P20.1-20.12, 1977

[14] PARIKH P.G., REYNOLDS W.C., JAYARAMAN R., CARR L.W., "Dynamic Behavior of an Unsteady Turbulent Boundary Layer" Nasa tm 81304 1981

[15] PATEL M.H., "On Turbulent Boundary Layers in Oscillatary Flows" Proc. Roy. Soc. Vol A353, p 121-144, 1977

[16] PERICLEUS K.A., "An Oscillatory Turbulent Boundary Layer in an Adverse Pressure Gradient" Phd Thesis, Queen Mary College, Univ of London, Enland, 1977

[17] RAKOWSKY E.L., "the Effect of Freestream Oscillations on the Incompressible Turbulent Boundary Layer on a Flat Plate With Pressure Gradient" Phd Thesis, Stevens Inst. of Tech., Hoboken, N.j., 1966

[18] SIMPSON R., "Features of Unsteady Turbulent Boundary Layers as Revealed From Experiments" Agard C.p. 227, P19.1-19.10, 1977

[19] SIMPSON R.L., SHIVAPRASAD B.G., 1983, "The Structure of a Separating Turbulent Boundary Layer, part 5 : Frequency Effects on Periodic Unsteady Free Stream Flows", Journal of Fluid Mech., Vol 131, P319, 1983

[20] SIMPSON L., SHIVAPRASED B.G., CHEW Y.T., 1983, "The Structure of a Separating Boundary Layer, Part 4 Effects of Free Stream Unsteadiness" Journal of Fluid Mech., Vol 127, P219, 1983

[21] YU J.C., "Mean Flow and Reynolds Stresses Measurements in the Vicinity of the Trailing Edge of a Naca 63-012 Airfoil" Nasa Report tm-80224, 1980

[22] HAH C., LAKSHMINARAYANA B., "Measurement and Prediction of Mean Velocity and Turbulemce Structure in the Near Wake of an Airfoil" Journal of Fluid Mech., Vol 115, pp 251-282, 1982

[23] NOVAK C.J., RAMAPRIAN B.R., 1982, "Measurement in the Wake of an Infinite Swept Airfoil" Iowa Institute of Hydraulic Research, Report no 240, 1982

[24] RAMAPRIAN B.R., PATEL V.C., SASTRY M.S., 1981, "Turbulent Wake Development Behind Streamlined Bodies" Iowa Institute of Hydraulic Research, Report no 231, 1981

[25] JANSEN B.J., MUELLER T.J.,1983, "Experimental Studies of the Boundary Layer on an Airfoil at Low Reynolds Numbers" AIAA Paper 83-1671, 1983

[26] SATYANARAYANA, "Some Aspects of Unsteadu Flow Past Airfoils and Cascades" Agard C.p. 177, pr 25, 1975

[27] SAXENA L., FEJER A., MORKOVIN M., " Features of Unsteady Flows Over Airfoils" Agard C.p. 227, P22.1-22.11, 1977

[28] COVERT E.E., LORBER P.F., VACZY C.M., 1983, "Measurement of the Near Wake of an Airfoil in Unsteady Flow" AIAA Paper 83-0127, 1983

[29] MC CROSKEY W.J., PUCCI S.L., "Viscous-Inviscid Interaction on Oscillating Airfoils" AIAA Paper nr 81-0051, 1981

[30] MC ALISTER K.W., CARR L.W., "Water Tunnel Visualisations of Dynamic Stall" ASME Journal of Fluids Eng., Vol 101, 3, P377-380, 1979

[31] ROBINSON L.G., LUTTGES M.W., 1983, "Unsteady Flow Separation and Attachment Induced by Pitching Airfoils" AIAA Paper 83- 0131

[32] HO C.M., CHEN S.H., "Unsteady Wake of a Plunging Airfoil" AIAA Paper nr 80-1446, 1980

[33] WERLE H., 1976, "Visualisation Hydrodynamique de l'Ecoulement Autout d'Une Pale Oscillante" Onera Rapport Technique 56/1369 An, 1976

[34] KOTTAPALLI S.B.R., PIERCE G.A., "Drag on an Oscillating Airfoil in a Fluctuating Free Stream" ASME Journal of Fluids Eng., Vol 101, 3, p 391-399

1979

[35] CEBECI T., "Prediction of Boundary-Layer Characteristics of an Oscillating Airfoil" Unsteady Turbulent Shear Flows Springer Verlag 1981

[36] SHAMROTH S.J., "the Prediction of the Turbulent Flow Field About an Oscillating Airfoil Using a Time-Dependent Navier Stokes Procedure" Unsteady Turbulent Shear Flows, Springer Verlag 1981 (in Press)

[37] SMITH T.F., 1983, "Interacting Flow Theory and Trailing Edge Separation - No Stall", Journal of Fluid Mech., Vol131, 1883

[38] CEBECI T., SCHIMKE S., 1983, "the Calculation of Separation Bubbles in Interactive Turbulent Boundary Layers" Journal of Fluid Mech., Vol 131, P305, 1983

[39] SCHLICHTING H., 1968, "Boundary Layer Theory" mc Grew Hill Series in Mechanical Engineering, mc Grew Hill Book Company p 512, 1968

[40] THOMPSON B.E., WHITELAW J.H., 1984, "Flying Hot Wire Anemometry" Experiments in Fluids 2, 47-55, 1984

[41] KOOL P., "Determination of the Reynolds Stress Tensor With a Single Slanted Hot Wire in Periodically Unsteady Turbomachinery Flow" ASME Paper nr 79-gt-130, 1979

[42] DE GRANDE G., KOOL P., "An Improved Experimental Method to Determine the Complete Reynolds Stress Tensor With a Single Rotating Hot Wire" Journal Phys. e. Sci. Instrum., Vol 14, P196-201, 1981

[43] CASTRO I.P., 1975, "Statistics of the Instantaneous Velocity Vector and the Consequent Errors in Anemometer Measurements" Euromech 63, 2-2, Techn, Univ. of Denmark, 1975

[44] BAKER A.J., YU J.C., GATSKI T.B., "Prediction and Measure- ment of Turbulent Aerodynamic Trailing Edge Flows" AIAA Paper nr 80-1395, 1980

[45] GRADSHTEYN I.S., RYZHIK I.M., "Tables of Integrations Series and Products" Academic press, 1965

Appendix 1 : Zero mean velocity determination

When a mean flow velocity $\bar{q}$ becomes very small whereas the fluctuations q' are high ($\bar{q} < q'$) some difficulties arise when applying equations (1) and (2). These difficulties can best be described with the aid of figure 6.

On figure 6 the probability density of the velocity is shown for a one dimensional case. When $\bar{q}$ is large compared with q', all the values of the measured velocities are positive and no problems arise when averaging the velocity in order to obtain its mean value $\bar{q}$. When the fluctuations are of the same order as $\bar{q}$, negative velocities can be expected and the dashed probability curve extends towards negative values in figure 6. Since a hot wire detects only the velocity modulus, the solid line probability curve is measured. The mean value $\langle q \rangle$ of the measured solid probability curve is different from the mean velocity $\bar{q}$ and a correction is to be made on $\langle q \rangle$ in order to obtain the exact mean velocity $\bar{q}$.

This problem has been investigated (e.g. Castro [43]) but no practical correction rules have been found in the literature. The following procedure has therefore been developed in the present work.

In the following the velocities are to be considered as normalised with respect to the variance $\sqrt{q'^2}$. The dashed probality curve in figure 6 is assumed to be Gaussian and it can be expressed in function of the mean velocity $\bar{q}$ as follows

$$P(q) = \frac{1}{\sqrt{2\pi}} e^{-\frac{1}{2}(q-\bar{q})^2} \tag{A.1}$$

The solid probability curve $P'(q)$ can be derived by adaption of equation (A.1) and the mean value $\langle q \rangle$ of the solid curve is obtained from

$$\langle q \rangle = \int_{-\infty}^{\infty} q\, P'(q)\, dq \tag{A.2}$$

The contributions from positive and negative values of q are considered separately. The positive values of q give the following contribution to $\langle q \rangle$

$$\sqrt{2\pi}\, \langle q \rangle^{+} = \int_{0}^{\infty} q\, e^{-\frac{1}{2}(q-\bar{q})^2} dq$$

$$= \int_{-\bar{q}}^{\infty} (q-\bar{q})\, e^{-\frac{1}{2}(q-\bar{q})^2} d(q-\bar{q}) + \bar{q} \int_{-\bar{q}}^{\infty} e^{-\frac{1}{2}(q-\bar{q})^2} d(q-\bar{q}) \tag{A.3}$$

$$= e^{-\frac{1}{2}\bar{q}^2} + \bar{q}\sqrt{\pi/2}\, \left[1 + \mathrm{erf}(\bar{q}/\sqrt{2}) \right]$$

The negative contribution is obtained by considering a normal distribution

around $-\bar{q}$ as mean value. Negative values of q yield

$$\sqrt{2\pi}\ \langle q\rangle^{-} = \int_{o}^{\infty} q\ e^{-\frac{1}{2}(q+\bar{q})^2}\ dq$$

$$= \int_{o}^{\infty} (q+\bar{q})\ e^{-\frac{1}{2}(q+\bar{q})^2}\ d(q+\bar{q}) \ - \ \bar{q}\int_{o}^{\infty} e^{-\frac{1}{2}(q+\bar{q})^2}\ d(q+\bar{q}) \qquad (A.4)$$

$$= e^{-\frac{1}{2}\bar{q}^2} - \bar{q}\sqrt{\pi/2}\ [\ 1 - \mathrm{erf}(\bar{q}/\sqrt{2})\ ]$$

The sum of both contributions yields

$$\langle q\rangle = \langle q\rangle^{+} + \langle q\rangle^{-} = \sqrt{2/\pi}\ e^{-\frac{1}{2}\bar{q}^2} + \bar{q}\ \mathrm{erf}(\bar{q}/\sqrt{2}) \qquad (A.5)$$

From equation (A.5) it appears that

$$\langle q\rangle = \bar{q} \qquad \text{when} \qquad \bar{q} \to \infty$$
$$\qquad (A.6)$$
$$\langle q\rangle = \sqrt{2/\pi} \qquad \text{when} \qquad \bar{q} \to 0$$

In a two dimensional flow with velocity components u and v, equations (A.1) and (A.2) can be rewritten as (with u and v normalised)

$$P(u,v) = \frac{1}{2\pi}\ e^{-\frac{1}{2}(u-\bar{u})^2 + v^2} \qquad (A.7)$$

$$\langle q\rangle = \iint_{-\infty}^{\infty} \sqrt{u^2+v^2}\ P(u,v)\ du\ dv \qquad (A.8)$$

It has been assumed that u is defined in the mainstream direction such that $\bar{v} = 0$. The variances of u and v are assumed to be equal and the effect of non-zero $\overline{u'v'}$ is not taken into account in the present approach. Equation A.7 is not subject to sign problems as discussed for the one dimensional approach. Equation A.8 can be rewritten as, with $u = q\cos\theta$

$$\langle q\rangle = \frac{1}{2\pi} \int_{o}^{\infty}\int_{o}^{2\pi} q^2\ e^{-(q^2 - 2\bar{u}q\cos\theta + \bar{u}^2)/2}\ d\theta\ dq \qquad (A.10)$$

where, according to Gradshtein 3.937 [45]

$$\int_{o}^{2\pi} e^{q\bar{u}\cos\theta} d\theta = 2\pi\ I_o(\bar{u}q) \qquad (A.11)$$

Hence,

$$\langle q \rangle = \int_0^\infty q^2 e^{-(q^2+\bar{u}^2)/2} I_0(\bar{u}q)\, dq \qquad (q = \sqrt{2x})$$

$$= e^{-\bar{u}^2/2} \int_0^\infty \sqrt{2}\,\sqrt{x}\, e^{-x} I_0(\bar{u}\sqrt{2}\,\sqrt{x})\, dx \qquad (A.12)$$

According to Gradshtein 6.643.2 [45]

$$\langle q \rangle = e^{-\bar{u}^2/2}\,\sqrt{2}\,\frac{\Gamma(3/2)}{\Gamma(1)}\,\frac{\sqrt{2}}{\bar{u}}\, e^{\bar{u}^2/4} M_{-1,0}(\bar{u}^2/2)$$

$$= e^{-\bar{u}^2/2}\,\sqrt{2}\,\Gamma(3/2)\,\Phi(3/2,1;\bar{u}^2/2) \qquad (A.13)$$

M and Φ are degenerate hypergeometric functions ([45], pp 1058,1059). According to [45]

$$\langle q \rangle = \sqrt{\pi/2}\,\Phi(-1/2,1;-\bar{u}^2/2) \qquad (A.14)$$

$$\Phi(\alpha,\gamma;z) = 1 + \frac{\alpha z}{\gamma 1!} + \frac{\alpha(\alpha+1)z^2}{\gamma(\gamma+1)2!} + \ldots$$

From equations (A.5) or (A.14) it is in principle possible to determine the real mean velocity $\bar{q}$ from the measured mean values $\langle q \rangle$. When the turbulence is small, equation (A.14) again reduces to equation (A.6).

An analytical expression for a full three dimensional flow has not been found. It however appeared that both equations (A.5) and (A.14) yield quite similar and satisfactory results. To avoid unacceptable computing times, an approximation for equations (9) and (12) has been searched, as follows

$$\langle q \rangle = \bar{q} + K\, e^{-\bar{q}^2/2} \qquad K = 1.2 \qquad (14)$$

K is a constant parameter which has been calibrated in such a way that a good zero-definition for the mean velocity is found for all the experiments. A good zero definition means that velocity profiles which are partially reversed should have a net and continuous shape when the velocity changes of sign. Equations (A.5), (A.14) ans (A.16) are illustrated on figure 7, where the difference between the measured $\langle q \rangle$ and the real $\bar{q}$ is drawn against $\bar{q}$. At large values of $\bar{q}$, the difference is zero, whereas at zero mean velocity the correction becomes maximum.

Appendix 2 : Data tape user guide

The data are made available on magtape. Following formats are used

- 2400 foot reel
- 9 track
- 1600 bits/inch
- odd parity
- ASCII coded
- unlabeled
- 80 characters / record
- 20 records or 1600 bytes / block

Other tape formats can be delivered on request.

The different test cases are separated by tape end-of-file marks. Each file contains a certain number of time step data sets. Each time step covers eight blocks of 20 card images which each contain the data for one of the eight chordwise positions.

The first card image for each block contains following information :

column	1 to 5 :	free
	6 to 10 :	identification (see page)
	11 to 20 :	time step number (1 to 240)
	21 to 25 :	chord sequence number (1 to 8)
	26 to 30 :	number of data cards (max 19)
	31 to 40 :	chordwise position in % chord
	41 to 50 :	local airfoil thickness in % chord
	51 to 60 :	phase angle in degrees (0 to 360)
	61 to 70 :	instantaneous incidence angle in degrees
	71 to 80 :	blade surface slope in degrees

The data can be read using the format (5X,A5,I10,2I5,5F10.0).
This card is followed by the speficied number of data cards, which are formatted as follows

column 1 to 10 : free
11 to 20 : coordinate normal to the wall in % chord
21 to 30 : u/Q velocity component parallel to the local wall
31 to 40 : v/Q velocity component normal to the wall
41 to 50 : $\sqrt{u'^2}/Q$ r.m.s. velocity fluctuations
51 to 60 : $\sqrt{v'^2}/Q$ r.m.s. velocity fluctuations
61 to 70 : $\sqrt{w'^2}/Q$ r.m.s. velocity fluctuations
71 to 80 : $\overline{u'v'}/Q^2$ minus Reynolds stress

These cards can be read with the format specification 10X,7F10.0.

Since not all the available time steps (240) are relevant, a selection has been made in order to reduce the amount of data. The following selection has been made.

file	ident	number of time steps
1	BL15	40, every 9.0° phase shift
2	BLA5	140, every 1.5° for i>5°, every 9° for i<5°
3	BL16	140, every 1.5° for i>6°, every 9° for i<6°
4	BL18	140, every 1.5 °for i>8°, every 9° for i<9°
5	BLA5	140, every 1.5° for i>10°, every 9° for i<10°

Some of the turbulence data in these files have been smoothed for more clarity in the turbulence structure.

The first 5 files are followed by another 5 files which contain the rough unsmoothed data and where all the available time steps have been included.

Appendix 3 : Smoothing procedure

The smoothing of the data occurs in the time domain. 240 data points are available which are periodic. The smoothing is based on a least squares fit of parabolas through a certain amount M of data points.

The characteristic of the smoothing routine is shown on figure 21. From this figure it appears that the smoothing routine behaves as a current low-pass filter. On the same figure is shown how scatter which is superponed on a sine can quite well be discarted from the basic signal. In this example 240 data points were used, which corresponds to the amount of time data in the present experiments.

```
      SUBROUTINE SMOOTC(Y,N,M,DY,Z)
C-------------------------------------------------
C   SMOOTHING OF PERIODIC Y USING PARABOLIC FITTING
C   Y = ARRAY WITH PERIODIC DATA
C   N = NUMBER OF DATA POINTS
C   M = FRACTION OF N OVER WHICH SMOOTHING APPLIES
C   DY = REPRESENTATIVE TIME BETWEEN Y(I) AND Y(I+1)
C   Z = SCRATCH VEKTOR WITH SAME DIMENSIONS AS Y
C
C   DEPT OF FLUID MECHANICS
C   VRIJE UNIVERSITEIT BRUSSEL
C   PLEINLAAN 2
C   1050 BRUSSELS BELGIUM
C-------------------------------------------------
      DIMENSION Y(1),Z(1),X(240),DUM(240)
      X(1)=0.
      DUM(1)=0.
      DO 60 I=2,M
      X(I)=X(I-1)+DY
   60 DUM(I)=X(I)*X(I)
      IF(M.EQ.0)RETURN
      IF(M.GT.240)M=240
      IF(M.LT.4)M=4
      A=FLOAT(M)
      DO 50 I=1,N
   50 Z(I)=0.
C-------------------------------
C   VSUM = STANDARD V.I.S. ROUTINE
C          VSUM(SUM,X,M) MAKES THE SUM OF X(I),I=1..M
C   VDOT = STANDARD V.I.S. ROUTINE
C          VDOT(SUM,X,Y,M) MAKES THE SCALAR PRODUCT OF X AND Y
C-------------------------------
      CALL VSUM(B,X,M)
      CALL VSUM(C,DUM,M)
      CALL VDOT(D,X,DUM,M)
      CALL VDOT(E,DUM,DUM,M)
      A1=C*E-D*D
      B1=D*C-E*B
      C1=B*D-C*C
      D1=B*C-A*D
      E1=A*C-B*B
      F1=A*E-C*C
      DE=A*A1+B*B1+C*C1
      DO 10 I=1,N
```

```
      P=Q=R=0.
      DO 30 J=1,M
      L=J+I-1
      IF(L.GT.N)L=L-N
      P=P+Y(L)
      Q=Q+Y(L)*X(J)
   30 R=R+Y(L)*DUM(J)
      G0=P*A1+Q*B1+R*C1
      G1=P*B1+Q*F1+R*D1
      G2=P*C1+Q*D1+R*E1
      IF(ABS(DE).LT.1.E-20*(ABS(G0)+ABS(G1)+ABS(G2)))STOP
      G0=G0/DE
      G1=G1/DE
      G2=G2/DE
      DO 10 J=1,M
      L=J+I-1
      IF(L.GT.N)L=L-N
   10 Z(L)=Z(L)+G0+G1*X(J)+G2*X(J)*X(J)
      DE=FLOAT(M)
      DO 20 I=1,N
   20 Y(I)=Z(I)/DE
      RETURN
      END
```

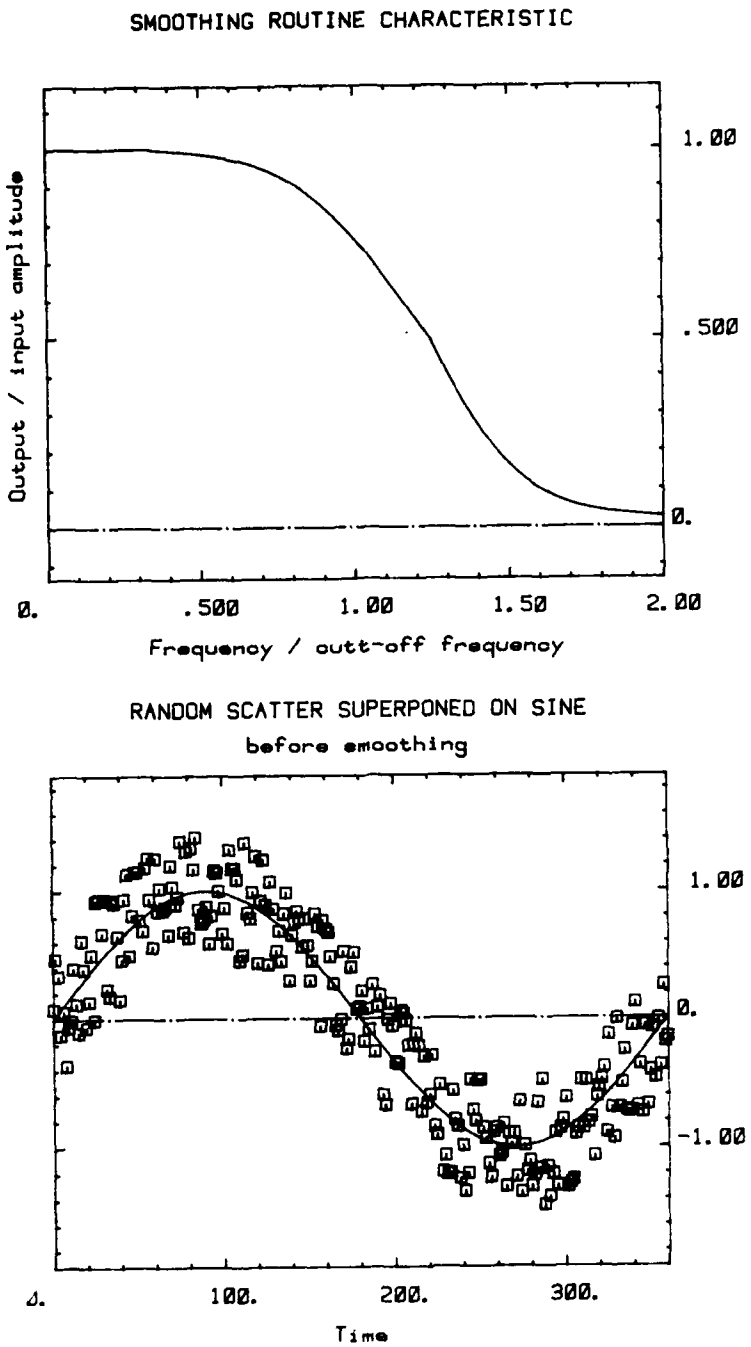

Figure 21 : Smoothing routine characteristics

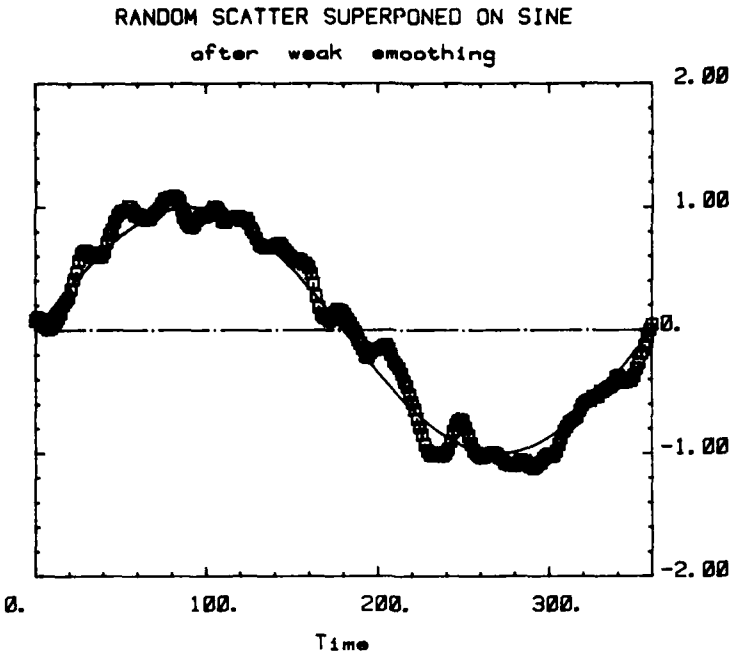

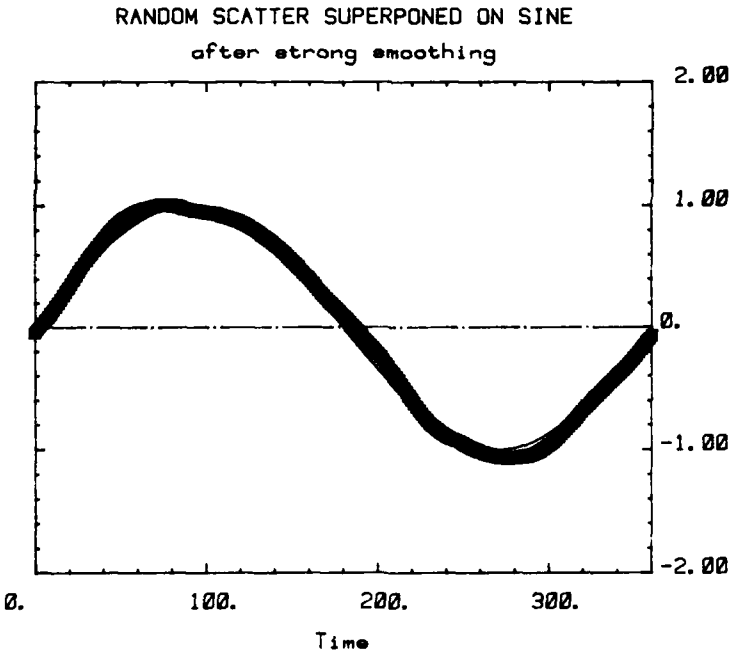

Figure 21 (continued)

END

FILMED

6-85

DTIC